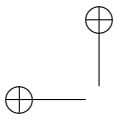
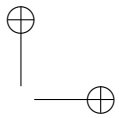

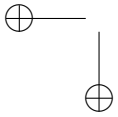
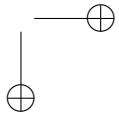

Università Politecnica delle Marche
Scuola di Dottorato di Ricerca in Scienze dell'Ingegneria
Curriculum in Ingegneria Meccanica

Numerical study of cold rolling process with variable thickness

Ph.D. Dissertation of:
Ing. Luca Maria Mattucci

Advisor:
Prof. Marco Sasso

Coadvisor:
Prof. Dario Amodio

Curriculum Supervisor:
Prof. Ferruccio Mandorli

XVI edition - new series

Università Politecnica delle Marche
Scuola di Dottorato di Ricerca in Scienze dell'Ingegneria
Curriculum in Ingegneria Meccanica

Numerical study of cold rolling process with variable thickness

Ph.D. Dissertation of:
Ing. Luca Maria Mattucci

Advisor:
Prof. Marco Sasso

Coadvisor:
Prof. Dario Amodio

Curriculum Supervisor:
Prof. Ferruccio Mandorli

XVI edition - new series

Università Politecnica delle Marche
Scuola di Dottorato di Ricerca in Scienze dell'Ingegneria
Facoltà di Ingegneria
Via Brecce Bianche – 60131 Ancona (AN), Italy

To my sons,
Elia and Sole

Acknowledgments

The author would like to express sincere gratitude to his supervisor, Prof. Eng. Marco Sasso, machine design professor at Università Politecnica delle Marche, for his guidance, support and encouragement throughout the course of this research.

The author is also deeply grateful to all the staff of machine design research group, an ING/IND-14 family rather than a working group. They really deserve to be mentioned one by one, starting from Professor Dario Amodio, Marco Rossi, Edoardo Mancini, Gianluca Chiappini, Attilio Lattanzi, Massimo Natalini and last but not least Emanuele Farotti. He wishes to thank them all for the support, help and all the formidable shared moments throughout academic circumstances and not only.

Acknowledgement is also given to his parents for the enthusiastic support and continuous encouragement throughout these years.

The author would like to express sincere thanks to his darling wife Caterina, for her love, continuous encouragement and her patience during the Ph.D study. He hopes that she will be proud of this dissertation and finish line and that this will provide some sort of satisfaction after her many sacrifices such as living in Ancona... joke! Thanks to his children Elia and Maria Sole, thanks for being there, thanks for giving him such pleasure with their presence or funny pictures, videos and audio messages when being away from home!

Thank you all indeed!

Ancona, November 2017

Ing. Luca Maria Mattucci

Abstract

The buzz word is metal replacement. Replacing those heavier older components with a plastic or composite is surely a logical exercise for anyone wanting to shed a few kg. Cars today, for example, are reportedly 50% by volume one type of plastic or another, but that represents only 10% of the overall weight.

So, with all this talk about metal replacement where does the aluminium industry fit in? While many associate exotic materials with weight reduction, the aluminium industry is keen to remind engineers it is also part of the solution.

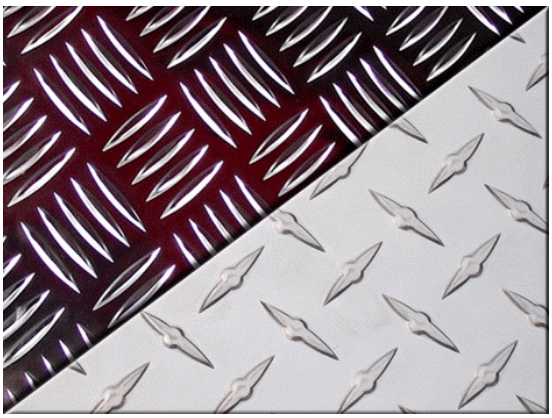

Figure 1 – Aluminium diamond plate examples

The present research activity starts from the idea of an alluminium producer who intends to develop an innovative cold rolling technology able to incentivize the use of alluminium alloy in the automotive world, through the distribution of different thickness areas on the finished product. A very common aluminium diamond plate (shown in Figure 1) can be used to explain the concept of this kind of cold rolling process. However, the over-height related to the diamond is contained in a small area of $1 \div 2$ cm^2 .

The research activity set out hereinafter aims to validate the opportunity to vary shape and dimensions of those diamonds until remarkable size zones with increased thickness are obtained.

So after sharing all the cold rolling process information, i.e. cold rolling parameters, rolling mill data and part of the study materials (Cold Rolling Handbooks, [1, 2]) the aluminium producer requested scientific support to validate the feasibility of this kind of technology and to identify limits or criticalities.

Contents

List of Figures

List of Figures

List of Tables

Chapter 1

Introduction

The low cost of the product coupled with the long-proven technologies for mass production make steel the most used material in the automotive industry. However, green economy policies such as weight and consumption containment are pushing for steel components to be replaced with aluminium alloy ones, especially parts formed by sheet metal.

Use of rolling products is constantly increasing in the automotive field: in addition to the coating and/or finishing role, the current trend is to use aluminium alloy for structural components as well. However, technological systems can not provide an adequate product when a high structural strength is required related to specific areas only (e.g. junctions with other components where localized stiffness is required). Consequently it translates into the use of more material than is necessary or with a global geometric over-dimensioning of any finished product or with additional processes, such as the addition of material through welded reinforcements. From a structural point of view, such over-dimensioning results in an increase of weight of the overall finished product and hence a rise in the operating costs of the vehicle, since consumption is strictly related to mass. From an energetic point of view it should be noted that any surplus of material is intrinsically related to a "waste" of the energy used in production processes, and subsequently an increase in the cost of the component.

As illustrated by the diagram in Figure 1.1, aluminium alloys (purple) show a good compromise between elongation at break (necessary for a good forma-

bility of component) and specific strength (i.e. the ratio of tensile strenght to density). However the fact that it has the same specific stiffness (i.e. the ratio of elastic modulus to density) as its main competitor, steel, meant the aluminium alloys were employed for a few coating applications only and barely used for structural components when stiffness is the primary target. In this case, increasing the component thickness would compensate the lower elastic modulus value causing the weight reduction to decrease, or even disappear, while the cost remains unchanged or even higher.

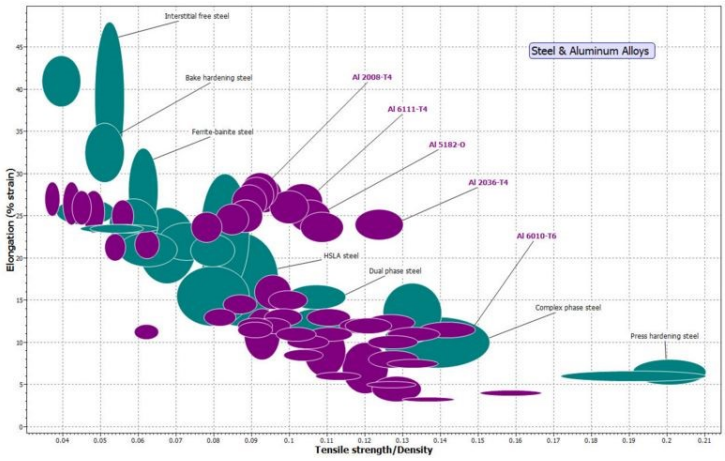

Figure 1.1 – Ashby diagram, elongation VS specific strenght

However if the distribution of material in a rolled product could be optimised by using a lower value thickness in the zones which are less stressed and a higher value thickness in the zones which are most stressed, the gain in terms of weight reduction would be considerable.

The main technological aim of this research project is the development of highly specialised processes to achieve optimised products, where the material can be best distributed where it is needed, to satisfy strength and/or stiffness requirements. Regarding the cold rolling process, the aim is to achieve a better optimisation of the 1D solution, also known as profile-rolling (Figure 1.2), already seen in many industrial areas: the multi-thickness rolling process named patch-rolling.

It represents an absolute innovation by allowing the higher thickness zones

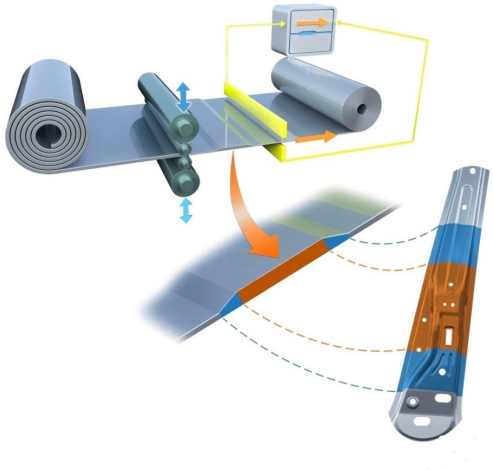

Figure 1.2 – Technological scheme of *profile rolling*

already used in the process of cold rolling to be obtained, with respect to the requested sizes and positioning resulting from the stress map. To this purpose the goal is to develop a support tool able not only to indicate the feasibility of the patches, as requested by the project, but also which suggests any amendments needed such as dimension of the patches, thickness variation, fillet radius etc.

The first stage of the project was the choice of the material with best performances in both rolling and stamping processes. To this purpose, several possible challengers were deeply investigated through uni-axial and formability tests. First ones were led to identify the flow plastic curves and principal mechanical characteristics of the material while the formability ones allowed the anisotropy influence and the Forming Limit Diagrams to be evaluated thanks to advanced optical methods.

In light of the characterizations shown above, one material was selected for all the future analytical activities. The following one, indeed, was the development of a finite element method model of the patch-rolling process in which only mechanical properties of the material were requested. After the model was successfully set-up and validated, several patch-configurations were investigated with the FEM model already described. Due to the unbalanced length-wise

direction deformation of the work-piece a more simple and fast analytical model was also developed in MatLAB®to provide a pre-view of the shape of the laminated work-piece only to evaluate the quality of the patch distribution.

Then the study of how the principal factors (main variables) involved in the rolling process may affect the feasibility of the process itself, was performed through a FEM experimentation organized according to the Design of Experiments (DoE) techniques. The analysis of the results of the DoE allowed a real case application to be developed and analysed, starting from the patch distribution until the prototype realisation.

Chapter 2

The cold rolling process

2.1 Introduction

The rolling process is a plastic deformation process in which a workpiece is pulled through a pair of rolls thus determining a rolling contact guaranteeing both deformation and supply of the material into the roll bite. The workpiece slips forward drawn by friction forces acting on the surface between it and the the rolls.

In Figure 2.1 F_{tx}, proportional to the coefficient of friction, is the force drawing the workpiece in the rolling gap (also known as "roll bite") whereas F_{nx}, independent of the coefficient of friction, acts to oppose the entry of the workpiece into the arc of contact.

The workpiece in bite between the rolls is subject to compression and undergoes a lengthening, in the rolling direction, and a spreading, in the transversal direction. In the entry section, the workpiece slips in a direction opposite to the spin of the rolls *(pressure zone)*, whereas in the exit zone it tends to slip forward *(extrusion zone)*.

Friction forces balance these two movements and are directed towards a "neutral" point (N) in the roll zone where the speed of the worked material equals that of the rolls.

The displacement of the neutral point has been widely investigated in the present study and, as it will be highlighted, it depends on several variables,

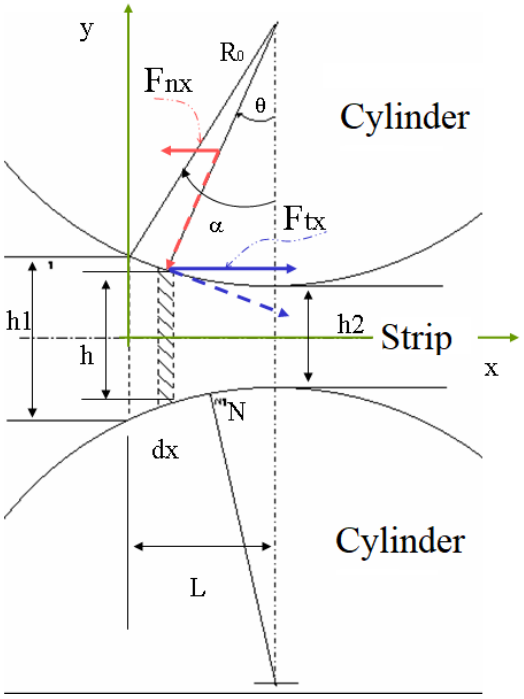

Figure 2.1 – Friction forces

such as pull, reduction, coefficient of friction (μ) etc.

As far as the latter is concerned and, more precisely, with regard to its effect on the position of N, we can anticipate the result which will be easily understandable when looking at Figure 2.1: N tends to shift towards the entry zone of the roll bite with an increase in μ, since F_{tx} tends to take the strip to the speed of the roll definitely faster than in the case of an inferior friction. And this is because F_{tx} increases with increase in the coefficient of friction, F_{nx} remaining, instead, constant. The effect of the other variables is not so readily understandable, the study of their effect will therefore follow in the next chapters.

The distribution of stresses and strains is rather complex; we can make an accurate calculation by using the finite element analysis, or through a traditional study which, although based on several assumptions, will bring results to be considered the more reliable, the thinner and the wider the workpiece.

2.2 Calculation of stresses distribution

2.2.1 Simplifying assumptions

For the purpose of calculating the stresses distribution in the arc of contact, a series of fundamental assumptions are necessary to simplify the problem:

1. state of plane strain with no lateral spread of the strip; when the thickness of the strip is little if compared to its width, this condition is satisfied thanks to the friction between cylinders and rolls and to the resistance opposed to the process of deformation by the non-deformed workpiece just outside the entry of the rolling mill;
2. homogeneous deformation of the strip; in other words, the strip is assumed to be made up of several thin elements vertical and normal to the rolling direction which shorten and lengthen, but never bend;
3. volume constancy;
4. elastic deformation is negligible; this assumption can be accepted bearing in mind that the elastic part is inferior to 0.2% whereas cold rolling deformations range between 20 and 50%;
5. the rolls are considered rigid; in the latest adjustments to the theory, the radius of curvature of the arc of contact equals the diameter of the deformed, roll due to rolls elastic deformation. All the same, the peripheral velocity of the rolls is assumed to be constant.
6. no strain hardening of the workpiece or strain hardening taking place with a constant coefficient of work hardening;
7. friction between the workpiece and the rolls is Coulombian (sliding Coulombic friction); the coefficient of friction is constant in the arc of contact and it is independent of temperature and speed;
8. the normal component of friction forces is negligible;
9. acceleration of the strip in the arc of contact is negligible; absence of inertia phenomena; on the whole, the amount of energy used for this purpose is negligible if compared to that used for strip deformation;
10. constant cross-section strains;

11. during the rolling process, the main stresses are in the rolling direction, normal to the direction of the rolling, with respect to the width of the workpiece, and normal to the the direction of the rolling in plane deformation of the strip;
12. thermal effects are negligible; this is particularly important since the effects that temperature may have both on the material and on the lubricant are known;

2.2.2 Distribution of roll stresses along the arc of contact - "Slab Analysis"

With reference to Figure 2.2, let's consider an infinitesimal vertical element in the arc of contact height h, thickness dx in the rolling direction and displaced between the point of entry to the rolling gap and the neutral point. p_r is the pressure acting between the surface of the roll and the strip on the ends of the worked element, p_{dx} is the vertical force acting as y on the end of the element and θ is the angle formed by the line joining the centre of the roll with the element and the vertical line.

If we assume that the width of the strip is uniform and that the rolls are rigid, the normal force acting on the end of the element is $p_r \frac{dx}{\cos\theta}$ and its component onto the horizontal direction (opposing to the strip getting into the roll bite) is:

$$p_r \ \frac{dx}{\cos\theta} \ \sin\theta = p_r \ \tan\theta \cdot dx \tag{2.1}$$

Whereas the tangential friction force is $\mu \ p_r \frac{dx}{\cos\theta}$, where μ is the coefficient of friction; the horizontal component of this force (dragging the strip in the roll bite) is:

$$\mu \cdot p_r \ \frac{dx}{\cos\theta} \ \cos\theta = \mu \cdot p_r \cdot dx \tag{2.2}$$

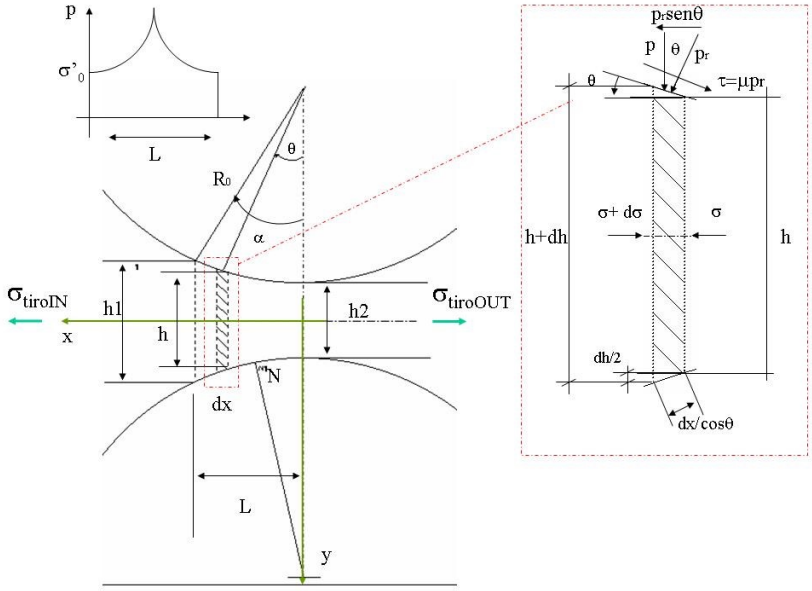

Figure 2.2 – Unitary forces acting on the infinitesymal element object of study

The equilibrium ratio of the specified element leads to:

$$\begin{aligned} &2\ p_r\ dx \tan\theta - 2\ \mu\ p_r\ dx = (h + dh) \cdot (\sigma + d\sigma) - h\sigma \Rightarrow \\ &2\ p_r\ dx \cdot (\tan\theta - \mu) + h d\sigma + \sigma dh = 0 \end{aligned} \tag{2.3}$$

which, rewritten, becomes:

$$p_r(\tan\theta - \mu) = \frac{d(h\sigma)}{2\ dx} \tag{2.4}$$

If the element is displaced between the neutral point and the exit of the arc of contact, the equation 2.4 becomes:

$$p_r(\tan\theta + \mu) = \frac{d(h\sigma)}{2\ dx} \tag{2.5}$$

combining 2.4 and 2.5 it becomes:

$$p_r(\tan\theta \mp \mu) = \frac{d(h\sigma)}{2\ dx} \tag{2.6}$$

If the vertical component of the forces on the end of the element is $p\ dx$,

hence

$$p\,dx = p_r\,\frac{dx}{\cos\theta}\,\cos\theta = p_r\,dx \tag{2.7}$$

and 2.6 becomes:

$$p(\tan\theta \mp \mu) = \frac{d(h\sigma)}{2\,dx} \tag{2.8}$$

From geometrical considerations:

$$\frac{1}{2}\cdot\frac{dx}{dx} = \tan\theta \Leftrightarrow dx = \frac{dh}{2\,\tan\theta} \tag{2.9}$$

so 2.8 can be rewritten in the form:

$$p\left(\frac{1}{2}\cdot\frac{dh}{dx} \mp \mu\right) = \frac{d(h\sigma)}{2\,dx} \tag{2.10}$$

This differential equation, that can also be expressed in other equivalent forms, is known as Von Kármán equation, named after the researcher who first derived it in 1925. It represents the starting point for the analysis known as *"theory of homogeneous deformation"*

2.2.3 Solution of the Von Kármán differential equation

Several solutions to Von Kármán equation have been developed by researchers and can easily be found in mechanical engineering books or in rolling process specialized books (references to the study material are present in the bibliography); it must be said, anyway, that their main difference is in the friction forces assumption. To give an example, Von Kármán solution is based on the assumption of presence of dry slipping along the arc of contact and of a friction force proportional to the value of normal local pressure (Coulomb friction assumption: $\tau = \mu\,p_r$).

A solution of Von Kármán equation is shown below.

Let us start by considering a condition of plasticity according to Von Mises

yeld criterion [1] , which is :

$$\sigma_1 - \sigma_3 = \frac{2}{\sqrt{3}}\sigma_0 = \sigma_0^{'} \tag{2.11}$$

where:

$$\sigma_1 = \sigma \qquad\qquad \sigma_3 = -p \tag{2.12}$$

assuming that $\sigma_3 = -p$, constant in the material, has value p on the axis and is equivalent to the contact pressure. Therefore:

$$\sigma + p = \sigma_0^{'} \tag{2.13}$$

from which:

$$\sigma + p = \sigma_0^{'} \Rightarrow d\sigma = -dp \tag{2.14}$$

Substituting this in 2.8 and recalling that $dx = \frac{dh}{2\ \tan\theta}$, we get to the form:

$$h \cdot dp - \left(\frac{\mu p}{\tan\theta} + \sigma_0^{'}\right) \cdot dh = 0 \tag{2.15}$$

For the integral calculation, several relationships among h, θ and the abscissa x, need to be introduced.

This can be done by approximating the arc of contact by a parabola having the same curvature and the same tangent to the circumference of the roll,when $x = 0$.

$$h = h_2 + 2\ R_0(1 - \cos\theta) \cong h_2 + \frac{x^2}{R_0} \tag{2.16}$$

The approximation, written in terms of θ, can be expressed as:

$$h = h_2 + 2\ R_0 \tan^2\theta = h_2\left(1 + \frac{R}{h_2}\tan^2\theta\right) \tag{2.17}$$

[1] Von Mises equivalent stress is $\sigma_0 = \sqrt{\frac{1}{2}\left[(\sigma_1 - \sigma_2)^2 + (\sigma_1 - \sigma_3)^2 + (\sigma_2 - \sigma_3)^2\right]}$ recalling that in plane strain $\sigma_2 = \frac{\sigma_1 + \sigma_3}{2}$ (direct as the axis of the cylinders) and substituting it in the previous one we get to the ratio

For convenience, we define:

$$\begin{aligned} &\tan\omega = \sqrt{\frac{R}{h_2}}\tan\theta \Rightarrow h = h_2\left(1+\tan^2\omega\right) \\ &A = 2\sqrt{\frac{R_0}{h_2}} \end{aligned} \tag{2.18}$$

By substituting 2.15 we have

$$\begin{aligned} &dp - (p\ \mu\ A + 2\ \sigma_0^{'}\ \tan\omega)d\omega = 0 \Rightarrow \\ &dp - p\ \mu\ A = 2\ \sigma_0^{'}\ \tan\omega\ d\omega \end{aligned} \tag{2.19}$$

Whose general integral, accepting the small-angle approximation, with $\tan\omega \cong \omega$, is

$$\frac{p}{\sigma_0^{'}} = C\ e^{\ \mu\ A\ \omega} - \frac{2}{A^2}\ (1+\mu\ A\ \omega) \tag{2.20}$$

which gives the stress distribution along the arc of contact, between the neutral point and the exit section.

In the zone between the entry and the neutral point the equilibrium 2.15 is modified since the friction force changes its sign:

$$h\cdot dp - \left(\sigma_0^{'} - \frac{\mu p}{\tan\theta}\right)\cdot dh = 0 \tag{2.21}$$

After approximation, the general integral results in:

$$\frac{p}{\sigma_0^{'}} = C\ e^{\ \mu\ A\ \omega} - \frac{2}{A^2}\ (1-\mu\ A\ \omega) \tag{2.22}$$

To calculate the constants we set boundary conditions, respectively

$$\sigma = \sigma_{tiroOUT}\ \ per\ \ \theta = 0 \Rightarrow \omega = 0 \tag{2.23}$$

for the exit section, and:

$$\sigma = \sigma_{tiroIN}\ \ per\ \ \theta = \alpha \Rightarrow \omega = \omega_\alpha \tag{2.24}$$

for the entry section

Resolving it we get the distribution of stresses between the neutral point and the exit and entry sections. These are respectively:

$$\frac{p}{\sigma_0'} = e^{\,\mu\, A\, \omega}\left(1 + \frac{2}{A^2} - \frac{\sigma_{tiroOUT}}{\sigma_0'}\right) - \frac{2}{A^2}\,(1 + \mu\, A\, \omega) \tag{2.25}$$

$$\frac{p}{\sigma_0'} = e^{\,\mu\, A\, (\omega - \omega_\alpha)}\left(1 + \frac{2}{A^2}(1 + \mu\, A\, \omega_\alpha) - \frac{\sigma_{tiroIN}}{\sigma_0'}\right) - \frac{2}{A^2}\,(1 - \mu\, A\, \omega) \tag{2.26}$$

If we draw a diagram of 2.25 and 2.25 we obtain the rolling stress distribution curve, generally known as "friction hill", as shown in Figure 2.3; the pairs of curves meet in a point of no slipping, known as"neutral point" or "no-slip point", which separates the pressure zone from the extrusion zone.

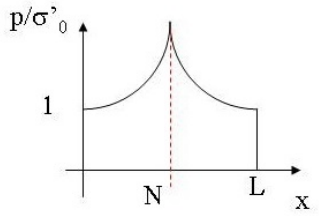

Figure 2.3 – Friction hill

Once the distribution of the stresses along the arc of contact is known, we can calculate the roll force and the torque:

$$F_{Laminazione} = \int_0^{\alpha} pR_0\, d\alpha \tag{2.27}$$

$$M_{Laminazione} = \int_0^{\alpha} \mu\, pR_0\, d\alpha + R_0\,(T_{OUT} - T_{IN}) \tag{2.28}$$

where $T_{IN} = \sigma_{tiroIN} \cdot h_1$ e $T_{OUT} = \sigma_{tiroOUT} \cdot h_2$

Equations 2.25, 2.26 e 2.27, once written in the explicit form, can be used to highlight the influence of various process parameters on the amplitude of the friction hill, hence on the roll force.

A graphical representation of this effect is shown in Figure 2.4 :

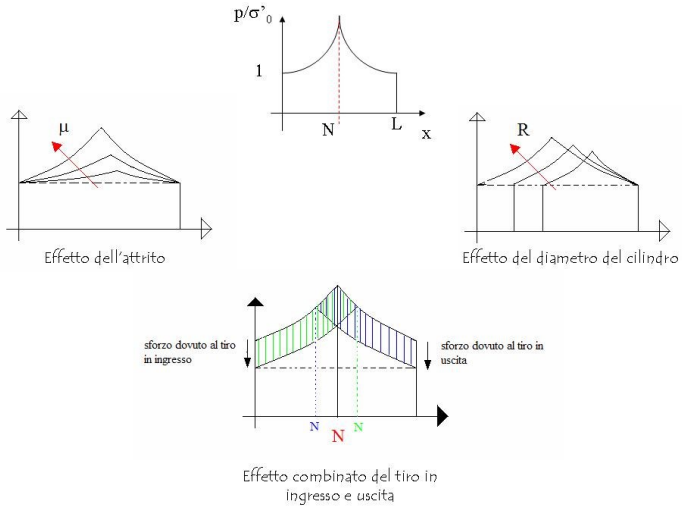

Figure 2.4 – Influence of several parameters on the amplitude of the friction hill

It can be seen that the rolling force increases with an increase in the coefficient of friction μ, in the radius of the cylinders and/or in pass draft $(h_1 - h_2)$ and in the material strain hardening capacity. It, conversely, decreases when back and front tensions are applied to the rolling mill.

2.3 Cold rolling mills - a brief mention

The cold rolling process aims at reducing the workpiece thickness and at maintaining the strip width. There are two cold rolling methods: the first uses a series of several roll stands in sequence (tandem rolling mill), the other uses reversing mills.

In tandem cold rolling the process of strip cross-section reduction to its final thickness actually takes place in one pass through several mills in parallel alignment, as shown in Figure 2.5.

Tandem rolling mills are used in soft material rolling (mild steel, stainless steel, etc.) and they generally have a set of two, three or four mills (each set is called stand) depending on thickness reduction to be reached. There is a pay

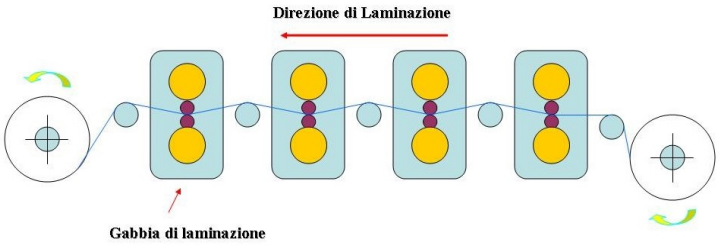

Figure 2.5 – Tandem rolling scheme

off reel at the entry of the mill and a take-up reel at its exit. Neutral rolls are displaced between the stands and the rolling speed is automatically adjusted as the workpiece passes from one stand to another.

Reversing mills are generally preferable to roll rolling different types of materials; in this mills the direction of rolling is alternately reversed, the workpiece is passed forward and backward through the rolls (Figure 2.6).

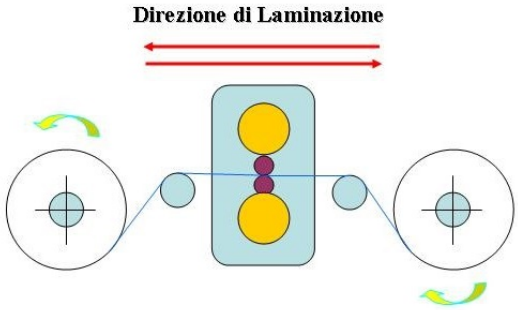

Figure 2.6 – Reversible rolling mill scheme

The "Two High" reversing mill (2Hi) is the most elementary type of reversing mill. It consists of two working rolls put in a direct line (Figure 2.7) enduring the rolling force; the latter being equally distributed on the support rolls which need to have big diameters as well. This arrangement uses high rolling forces and its application is limited to tight strips and controlled cross-section reduction operations (e.g. skin pass operations).

Figure 2.7 – "Two High" cold rolling mill scheme

The most common type of reversing mill is the "Four High" reversing rolling mill (4Hi), consisting of four rolls, as shown in Figure 2.8.

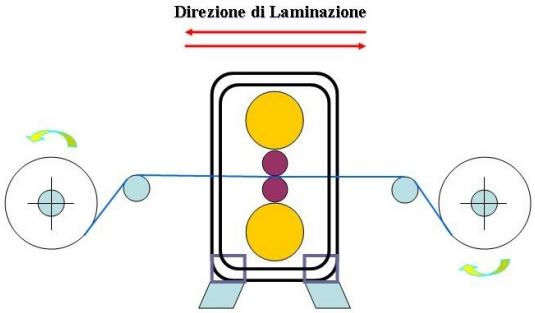

Figure 2.8 – "Four High" cold rolling mill scheme

In this case, the two work rolls in direct contact with the workpiece are smaller than the external rolls (backup rolls), working as support rolls so that the rolling force is reduced; the relationship between the two external rolls and the work rolls may vary, ranging from 2:1 to 3,5:1, depending on hardness of work materials and cross-section reduction.

The advantages of this rolling mill arrangement are to be found in its simple structure and in the fact that no big rolling tensions are needed; conversely, due to the big size of the rolls, this type of rolling mill cannot be used for rolling too wide, too thin or too hard workpieces.

As for "Six High" reversing rolling mills, they can be of two types: the first, consisting of two work rolls and four external rolls (Figure 2.9), is not widely

used due to a non favourable distribution of the rolling force: and this although the horizontal force of the pair of work rolls is absorbed by the external rolls. The second widely used mill arrangement, consists of six high reversing rolls aligned on the same vertical axis, two work rolls, two intermediate rolls and two backup rolls (Figure 2.10).

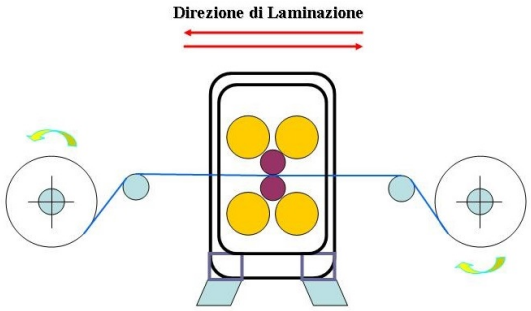

Figure 2.9 – "Six High" cold rolling mill scheme, version 1

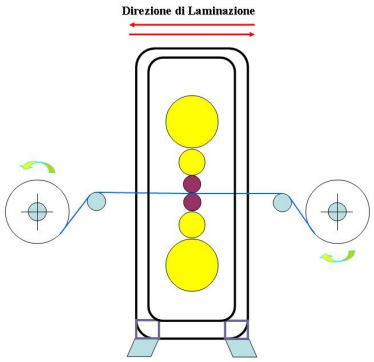

Figure 2.10 – "Six High" cold rolling mill scheme, version 2

2.3.1 Sendzimir reversing rolling mills

Sendzimir reversing rolling mills are of two types: "Z-High Mill", counting a total number of 18 rolls, and the "20-High Mill", where the number of rolls is 20.

Z-High mill

A scheme of a "Z-High Mill" is shown in Figure 2.11.

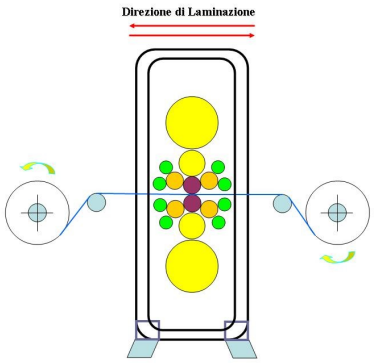

Figure 2.11 – "ZHi" Sendzimir rolling mill scheme

In order to reduce the diameter of the rolls the, "Z-High Mill" has lateral support rolls for the roll forces produced by the torque, in both rolling directions. These rolls are not in direct contact with the work rolls but there an axial adjusting device right before the rolling process.

In order to face eventual problems at the edges of the strips, intermediate rolls, tapered on the end, are placed in direct contact with the work rolls. These rolls can be translated in their axial direction so to adjust planarity defects at the edges.

This type of rolling mill is an intermediate version between the "4Hi" and the "20Hi" rolling mill. It offers several advantages: the work rolls are smaller than those of a "4Hi" mill, hence, major cross-section reductions are possible; the roll force is vertical, unlike the "20Hi" mills, where it is instead distributed among all the rolls and rolls flattening plays an important role on strip forging, leading to the necessary construction of proper tempered rolls and of several adjustments; no need to use heavy tensions as in the "20Hi" mills; it can easily be converted into a "4Hi" mill.

A disadvantage can be traced in the size of the work rolls which are too big to allow further strip thickness reductions.

Multi-High mill

A "20-High Mill" is comprised of 20 rolls (Figure 2.12, Figure 2.13 e Figure 2.14).

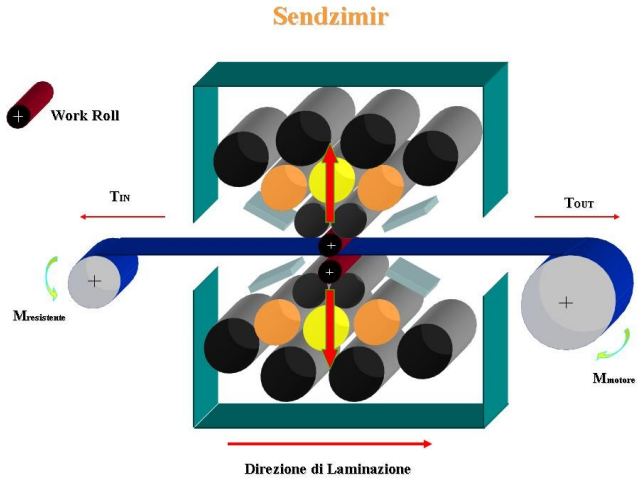

Figure 2.12 – "20 Hi" Sendzimir cold rolling mill scheme - whole mill

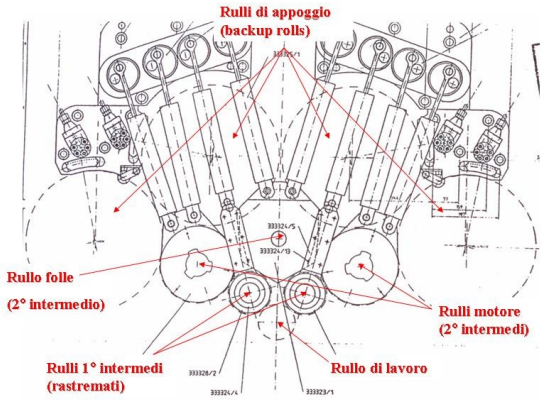

Figure 2.13 – "20 Hi" Sendzimir cold rolling mill scheme - upper half (rolls)

This type of rolling mill is characterized by very small sized work rolls (80-90mm diameter), through which large cross-section reductions, hard strips and

Figure 2.14 – "20 Hi" Sendzimir cold rolling mill scheme - whole mill

very small thickness can be obtained.

The rolls are easy to replace and suitable to produce high surface quality strips. Thanks to the use of smaller work rolls, the flattening of the rolls does not play an important role in a numerical simulation study which allows to consider the rolls as rigid surfaces without making major errors, and the rolling forces are inferior; having many rolls in direct contact among them leads to the problem of shape defects, more precisely at the edges of the strip. The solution to this problem has lays in the use of tapered rolls which can move in the direction of their axis (Figure 2.15).

Another important characteristic of this type of rolling mills, which also represents the main difference between them and the 2Hi,4Hi and 6Hi mills, is the design of backup-rolls. In traditional rolling mills the rolls are backed-up at their edges by the rolling mill pillars, thus behaving like beams bearing

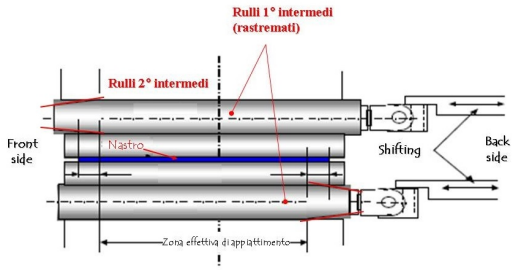

Figure 2.15 – "Shifting" of first intermediate tapered rolls scheme

distributed loads, where the effect of rolls bending is relevant.

In Sendzimir rolling mills, backup rolls are bound not only at the edges but along the shaft. The external mill housing encloses the whole rolls. This is possible since the backup rolls are comprised of a shaft divided into sectors on which rolling elements bearing are placed and which, in turn, discharge the deformation on the whole cylinder block mill frame (Figure 2.16a). This results in the advantage of a mill which can be used both for wide and tight strips since it is the mill frame that is subject to deformation (Figure 2.16b), and still to a lesser extent in comparison to the rolls in traditional rolling mills.

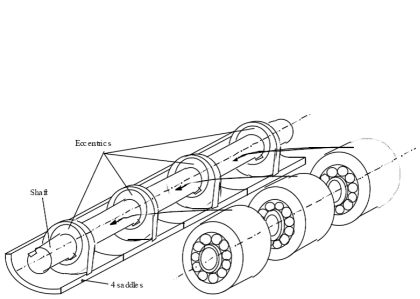

(a) Scheme of a backup-roll

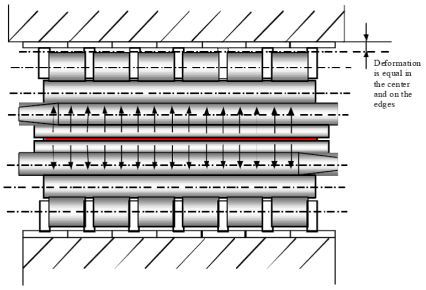

(b) Rolling mill deformation

Figure 2.16

Torque transmission, necessary in the rolling process, takes place thanks to second intermediate motor rolls which, together with tensions applied to the take-up and pay off reels, enable the rolling process.

Chapter 3

Aluminium and its alloys

3.1 Introduction

Aluminium is a ductile metal mainly sourced from bauxite ore, an hydrated aluminium oxide containing from 50 to 60% of Al2O3 (alumina), from 1 to 20% of Fe 203 (haematite), from 1 to 10% of SiO2 (silica) and minor quantities of other minerals with an amount of water ranging from 20 to 30 %.

Raw aluminium is processed through industrial production processes, such as fusion, forging or stamping. Many industries use it for manufacturing a huge variety of products and it has a key role in the world's economy. Structural components made of aluminium are essential for the aerospace industry and extremely important both in transport and construction fields where lightness of material, durability and resistance are key elements.

Figure 3.1 – Pure aluminium

Aluminium is a light metal with a silverly-white colouring (Figure 3.1) due to the light layer of oxidation which it develops when exposed to air and which

prevents corrosion, since it is insoluble. Aluminium has a specific weight of about a third of steel, or that of copper; it is malleable, ductile and easy to work. It has an excellent corrosion resistance and durability. Moreover, aluminium is non-magnetic and non-sparking , and it is the second most malleable metal and the sixth most ductile.

Aluminium is a chemical element included in the p- block metal group. It comes with the following general properties:

- Element with atomic number 13 and a face-centred cubic structure at room temperature;
- Electron Configuration: Ne3s23p1;
- Density: 2,70 g/cm3;
- Melting point: 660° C;
- Ultimate tensile strength: 55 – 91 Mpa;
- Modulus of elasticity: 66,6 GPa;
- Elongation at break: 55;
- Low specific weigh;
- High corrosion resistance;
- High thermal and electric conductivity;
- Non- toxicity;
- High plasticity;
- Excellent ductility and malleability;
- Low radiant power;
- Excellent weldability;

Aluminium alloys can be divided into two broad groups: casting alloys, used fot the production of casts, and wrought alloys, used for the production of rolled plates, forged components or extrudates. The latter, in particular, can conventionally be identified using their aluminium wrought alloys designation consisting of a four-digit number and a control acronym. The form of the designation is the following:

$$AAXXXXY$$

Where:

- AA stands for Aluminium Association;
- The first digit (X—) may range between 1 and 8 and indicates the principal alloying element;
- The second single digit (-X–),indicates a modification of the specific alloy, which is expressed by a 0;
- The last two digits (–XX) in the 1xxx series provide the degree of purity of aluminium, or minimum aluminium content. (For example, the aluminium content of 1050 is 99.50%); in all the other series, the third and fourth digits are arbitrary numbers given to identify a specific alloy in the series.

Moreover, to designate the aluminium alloy, a final letter (Y) is added to the code, separated by a hyphen. This letter indicates the thermal and mechanical treatments the alloy may undergo to achieve its final properties, before usage. The temper designation letters have the following meaning:

- F - As Fabricated: no special control over the strain-hardening conditions
- H - Strain hardened
- O - Annealed (tempering and recrystallization): The lowest strength, highest ductility temper
- W - Solution heat treated : applicable only to alloys which spontaneously age after solution heat-treatment
- T- Heat treated to produce stable tempers (other than F, O and H)

Most aluminium alloys are normally supplied as semi-finished products, thus manufactured for plastic deformation processes.

Mechanical strength of the alloy can be increased through refinement and homogenization of grain and through material hardening resulting from machining of the wrought alloy.

These alloys can be classified into two broad categories: non - heat treatable alloys, which can only be strengthened through cold working, and heat – treatable alloys, which can be made stronger by precipitation hardening through

coherent and semi-coherent phases.

3.2 Heat treatments

The main aluminium and aluminium alloys heat treatments are the following:

- annealing
- relaxation
- solution treatment
- precipitation hardening.

The term heat-treatment comprises all the cooling and heating operations executed on metal products, aiming at changing their mechanical properties, their specific metallurgical structure or their residual stress state.

When talking about aluminium, the application of the term is restricted since we refer to the specific operations employed in order to increase strength and resistance of alloys which can be hardened through precipitation hardening, thus generally referred to as "heat- treatable" alloys. Such mechanism consists in restricting dislocation movements the result of a proper distribution of particles in the grains. The formation of grain-boundary precipitates needs to be avoided since a grain-boundary already represents a barrier to the movement of a dislocation.

A phase diagram containing a solubility curve which increases with an increase in temperature is an essential attribute for an alloy to be precipitation-hardened.

The typical heat treatment involves two stages known as solution treatment and aging.

Solution treatment is the heating of an alloy to a suitable temperature, holding it at that temperature long enough to cause one or more constituents to enter into a solid solution and then cooling it rapidly enough to hold these constituents in solution. Subsequent precipitation heat treatments allow controlled release of these constituents either naturally (at room temperature) or artificially (at higher temperatures).

Solution treatment: the alloy is heated above the solvus temperature in order to obtain an homogeneous solution, because the second phase which uses to be less, dissolves into the first one. The alloy is kept at this temperature until an homogeneous solution is obtained. The homogeneous solid solution it is then quenched at a cooler temperature where the conditions for supersaturation of the solution are reached.

Aging: a treatment used on alloys to develop their properties consists in controlled precipitation hardening treatment of very fine particles and is conducted both at room and high temperatures. In general, precipitation does not start immediately but it needs an "incubation time" to allow the formation of stable proper-sized nuclei; the growing process takes place right after.

The speed of precipitation varies depending on the temperature. With low temperatures, the speed of reaction is controlled by the velocity of migration of atoms. When performed at temperatures just below the solvus temperature, the speed of precipitation is very low since the nucleation rate is slow. In this case, the solution is only lightly supersaturated and the precipitation is controlled by the atoms formation rate. When performed at intermediate temperatures, the speed of precipitation increases until it reaches the maximum speed, hence the time necessary for precipitation to take place is very short.

3.3 Main aluminium alloys

With respect to the first figure in the code, we distinguish:

- 1xxx Series alloys: the pure aluminium series comprised of 99% minimum aluminium. Alloys characterized by excellent corrosion resistance, high thermal and electrical conductivity, good workability and relatively poor mechanical properties.
- 2xxx Series alloys: principle alloying element is copper. These are heat-treatable alloys.
- 3xxx Series alloys: the major alloying element used is manganese which allows both to increase the mechanical strength of wrought alloys and to

reduce their sensitivity to intergranular corrosion and stress corrosion.

- 4xxx Series alloys:silicon is the used as principle alloying element which, when added to aluminium, improves its fluidity and and reduces its melting pot.
- 5xxx Series alloys: magnesium is the major alloying element which gives the alloy special properties of resistance to corrosion in addition to good levels of resistance to heat, excellent ductility and workability. It generally does not require age hardening and possesses good weldability.
- 6xxx Series alloys: Silicon and magnesium are the two major alloying elements. These are heat-treatable alloys which, after heat-treatment, develop intermediate mechanical properties, although generally inferior to the 2000 series alloys. They have good formability, good workability, as well as good machinability and weldability. This series alloys are the most widely used for heat-treated workpieces and for those obtained by fusion. They combine some favourable properties: good mechanical strength, relatively low sensitivity to hardening and good resistance to corrosion.
- 7xxx Series alloys: the principle alloying element is zinc, which has a higher solubility than aluminium. Binary Al- Zn alloys are generally not used, Al-Zn-Mg alloys are preferred. These are heat-treatable alloys which develop the highest mechanical properties among all aluminium alloys. Zinc addition increases resistance and hardness besides fostering self-hardenability of the alloy.
- 8xxx Series alloys (miscellaneous compositions): among these, Al -Li alloys are very important (i.e. 8090) characterized by low density (2,5-2,6g/cm3 depending on the percent of lithium contained in the alloy) and good resistance to stress, they maintain good static resistance, also after impact damage, and excellent toughness, even at low temperature. They are distinguished by good workability to machine tools and, in most cases, poor fusion weldability. These alloys are widely used for building aeronautic structures and for the construction of means of transport and of all parts subjected to great stresses, in general.

The alloys involved into the study merit a more in-depth analysis: 5182, 5754 and 6016 alloy.

3.3.1 AA 5182 alloy

The AA 5182 aluminium alloy belongs to the 5000 series alloys containing a high magnesium content, it is annealed and crystallized. The following table will provide its chemical composition [3, 4]:

Table 3.1 – AA5182 alloy chemical composition

Material	Percentage [%]
Aluminium, Al	$93.2 \div 95.8$
Chromium,Cr	0.10
Copper, Cu	0.15
Irone, Fe	≤ 0.35
Magnesium, Mg	$4.0 \div 5.0$
Manganese, Mn	$0.2 \div 0.5$
Silicon, Si	≤ 0.20
Titanium, Ti	≤ 0.10
Zinc, Zn	≤ 0.25
Other, each	≤ 0.05
Other, total	≤ 0.15

Traditionally used in aeronautics, for the construction of welded structures, the aluminium-magnesium 5182 alloy is characterized by excellent resistance properties to oxidation and corrosion in general; its mechanical properties are extremely high, its formability is also very high and it can be readily fusion welded. This alloy exhibits excellent toughness both at room and low temperatures.

It is widely used in trim panels, pressure vessels, lorries, road tankers, fuel tanks, as well as in ship structures, plates, wheels, cryogenic applications and, in general, in all applications not requiring very high static mechanical properties but good fatigue resistance.

Table 3.2 – Main physical properties of AA5182 alloy at room temperature

$\rho\ [g/cm^3]$	2.650
$k\ [W/mK]$	126
$C_p\ [J/gK]$	0.904
$E\ [MPa]$	69.600

Table 3.3 – Main processing properties of AA5182 alloy

Formability	Very good at O/H111 temper
Machinability on tool machines	Not good
Weldability	Good (TIG - MIG)
Corrosion resistance	Good

3.3.2 AA 5754 aluminium alloy

The AA 5754 aluminium alloy belongs to the 5000 series alloys containing a high magnesium content, it is annealed and crystallized. Its chemical composition is the following [3, 4]:

Table 3.4 – AA5754 alloy chemical composition

Material	Percentage [%]
Aluminium, Al	$93.6 \div 97.3$
Chromium,Cr	0.30
Copper, Cu	0.10
Cr + Mn	$0.10 \div 0.60$
Iron, Fe	≤ 0.40
Magnesium, Mg	$2.6 \div 3.6$
Manganese, Mn	≤ 0.50
Silicon, Si	≤ 0.40
Titanium, Ti	≤ 0.15
Zinc, Zn	≤ 0.20
Other, each	≤ 0.05
Other, total	≤ 0.15

The aluminium – magnesium 5754 alloy is characterized by excellent resistance properties to oxidation and corrosion in general; its mechanical properties are poor, its formability is instead very high and it can be fusion welded. The alloy is generally used in the form of thin plates. It is moreover widely used for the construction of trim panels, pressure containers, lorries, road tankers, chemical plants and ship structures, as well as of plates, wheels and applica-

tions not requiring very high mechanical properties. It is often used for the insertion of single elements to welded structures.

Table 3.5 – Main physical properties of AA5754 alloy at room temperature

$\rho\ [g/cm^3]$	2.650
$k\ [W/mK]$	138
$C_p\ [J/gK]$	0.213
$E\ [MPa]$	70.000

Table 3.6 – Main processing properties of AA5754 alloy

Formability	Very good at O/H111 temper
Machinability on tool machines	Not good (better at H32 temper)
Weldability	Good (TIG - MIG)
Corrosion resistance	Good

3.3.3 AA6016 aluminium alloy

The AA6016 aluminium alloy belongs to the 6000 series alloys containing a high silicon and magnesium content, it is annealed and crystallized. Its chemical composition is the following [3, 4]:

Table 3.7 – AA6016 alloy chemical composition

Material	Percentage [%]
Aluminium, Al	$96.4 \div 98.8$
Chromium,Cr	0.10
Copper, Cu	0.20
Iron, Fe	≤ 0.50
Magnesium, Mg	$0.25 \div 0.60$
Manganese, Mn	0.20
Silicon, Si	$1.00 \div 1.50$
Titanium, Ti	≤ 0.15
Zinc, Zn	≤ 0.25
Other, each	≤ 0.05
Other, total	≤ 0.15

Traditionally used in the fields of aerospace, railways and shipbuilding for welded structures, the 6016 aluminium-magnesium-silicon alloy exhibits excellent resistance to oxidation and corrosion in general. It has good mechanical

properties although inferior to the 2000 and 7000 series alloys; good machinability on machine tools and high formability: it is moreover fusion weldable.

The alloy is used in architectural applications, motorcycle and bicycle looms, welded structures in general. This system constitutes the main series of alloys used for hot-processed and merged components.

The 6016 alloy has recently been introduced into the automotive sector with regard to the application of stamped sheet metal components (car body and external panels).

Table 3.8 – Main physical properties of AA6016 alloy at room temperature

$\rho\ [g/cm^3]$	2.700
$k\ [W/mK]$	$190 \div 210$
$C_p\ [J/gK]$	0.869
$E\ [MPa]$	68.900

Table 3.9 – Main processing properties of AA6016 alloy

Formability	Very good at T4 temper
Machinability on tool machines	Good
Weldability	Good (TIG - MIG)
Corrosion resistance	Good

3.4 Hybrid aluminium composites

A hybrid matrix composite combines more than two kinds of matrix, such as a metal and a polymer.

In a polymer metal sandwich construction the matrix is formed by metal sheets and a polymer honeycomb structure which is fibre-reinforced as shown in Figure 3.2.

Polymer metal sandwich sheet composites are made from a polymer honeycomb structure enclosed by two thin metallic sheets. A resin or adhesive is used as a matrix, which holds it all together. The honeycomb structure makes the composite relatively light, but stiff.

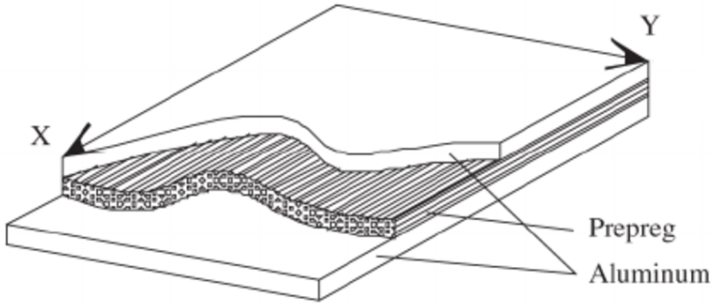

Figure 3.2 – Aluminium hybrid composite

Examples of polymer metal sandwich sheets are Hylite, which is made of two thin aluminium layers with a plastic (polypropylene/PP) core in between, and Dibond, which is similar to Hylite, but in which the polypropylene is substituted with polyethylene.

3.4.1 DIBOND®

DIBOND®combines 0.3mm Aluminium layers on either side with a Polyethylene core. The light weight sheet material can be transformed three dimensionally by using the routing and folding technique but it is stiff and stable at the same time, ideal for indoor as well as outdoor applications.

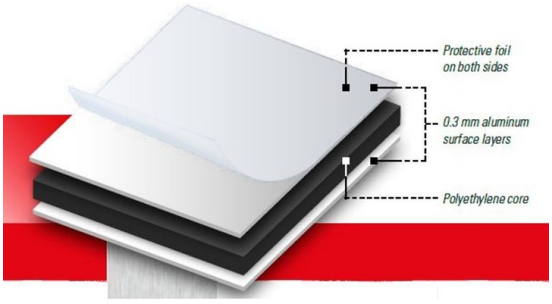

Figure 3.3 – DIBOND®layers detail

DIBOND®has a very low thermal expansion and is weather resistant: it is applicable with temperatures between -50°C and +80°C.

Common applications:

- Indoor and outdoor signage
- Shop fronts
- Exhibition design
- Shop fitting - Shop design - Furniture design
- Displays - POS/POP

The main process techniques are:

Table 3.10 – DIBOND®processing

Cutting	Sawing
Contour cutting	Contour milling
Drilling	Punching
Shearing	Fettling
Routing	Folding
Glueing	Bending
Screwing	Riveting
Clamp connections	Hot air welding

3.4.2 HYLITE ®

HYLITE®is an aluminium composite panel with a polypropylene core and aluminium outer skins. Two different core systems were tested.

Compact CORE - Panel thicknesses 1.2 mm and 2 mm

HYLITE®Compact CORE is the world's thinnest composite panel with thicknesses of $1.2mm$ and $2mm$, and it offers another special feature: the panel's core material can provide a hinge function, which withstands repeated bending without damage. This function is achieved by milling grooves in the same position into both outer aluminium skins.

Common applications include:

- Office articles - article design e.g. high-end CD sleeves, files and books backs etc.
- Technical manuals for automotive industry
- Notebook stands

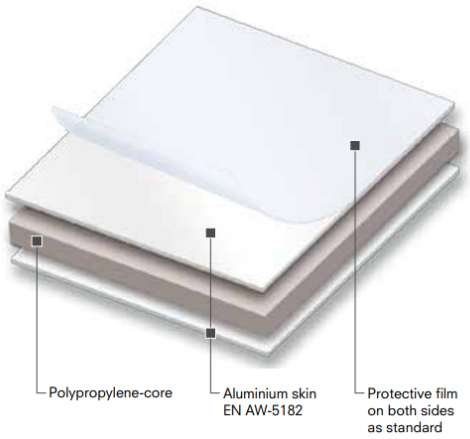

Figure 3.4 – HYLITE®layers detail

- Bicycle mudguards
- High-end packaging
- Suitcases

Foamed CORE - Panel thicknesses 3 mm and 4 mm

The core material for the $3mm$ and $4mm$ - panel thicknesses - is foamed in a thicknesses manufacturing process specially developed for this purpose. The result is an ultra-light aluminium composite panel, and the only cutback is in weight: HYLITE®in $3mm$ and $4mm$ thicknesses is up to 80% lighter than conventional steel sheets or up to 60% lighter than aluminium sheets yet provides the same flexural rigidity.

The foamed core panel features other superlative technical properties. Major advantages include dimensional stability at high temperatures and excellent digital printing results, due to the high quality aluminium strips used in the production process.

Common applications include:

- Interior / exterior cladding for commercial vehicles, agricultural machinery, mobile homes, caravans, buses, trains
- Machinery casing

- loudspeaker casings
- Furniture design
- Signs / advertising
- Light boxes

Moreover HYLITE®has dimensional stability at temperatures ranging from +120°C to , for a limited period, +150°C (approx. 30 minutes). It can also be processed in plenty of ways:

Table 3.11 – HYLITE®processing

Cutting	Roll bending
Sawing	Folding
Drilling	Punching
Gluing	Profile milling
Riveting	Screen printing
Screwing	Direct digital printing
Bending	Embossing
Contour cutting	Water jet cutting
Powder coating	Hinge joint routing

Chapter 4

Characterisation of materials

4.1 Introduction

The rolling process, also known as sheet-metal forming, using the Anglo-Saxon terminology, has acquired a dominant position in several fields of mechanics, such as the automotive and the aerospace industries. Of course, the tendency is to obtain, also in mass production, excellent quality finished products and to reduce scraps resulting from breaking, surface defectiveness or exceeding the Geometric Dimensioning & Tolerancing (GD&T) limits. In this scenario, the need to manifacture semi-finished products or finished parts characterised by a low index of scraps coming from procedural errors or surface defects, has given the impetus to several experimental, theoretical and numerical analyses of sheet-metal forming.

The capability of a workpiece to survive a bulk deformation process (i.e. forging) can be described as workability, which takes into account both the ductility of the worked material and the stress-rate enforced by the process; in this case fracture is a major concern. Conversely, the capability of a workpiece to survive sheet-metal working processes, is linked to the concept of formability, another complex property which is strictly related to causes of failure during the rolling process; some of them will be mentioned below.

During rolling, the surface of the worked material can appear "grainy" and show an "orange peel" effect. This is a natural consequence of the polycrys-

talline structure of metals. In fact, each grain has a crystallographic direction which distorts in a slight different way from the others. This effect has no backwash on the integrity of the structure but it may be aesthetically unacceptable. This problem can be avoided by using materials characterized by very tiny grains so that the effect would be invisible to the naked eye. In some work materials the yield stress can be highly localized and visible on the surface in the form of slip bands (Lüders bands). As the deformation process advances, the surface of the workpiece will be crossed by families of these slip bands which are harmless, as far as resistance is concerned, but intolerable on exposed surfaces. However, once the whole surface of the workpiece is covered with bands, they are not distinguishable any more.

In the case of localized necking, both aesthetics and functional properties are involved; although there is no fracture, the local material load resistance could be reduced, the other sections will still remain perfectly functional. The choice of materials is intended to optimize those factors capable of delaying the onset of the necking process or of redistributing the incipient necking. Once necking is triggered off, a subsequent plastic deformation will produce a localized thickness reduction up until fracture. In cold metal working, an even low yet positive value of m (strain rate sensitivity exponent) can be useful.

Many alloys are suitable for sheet-metal working treatments.

Of course, these alloys need to have sensibly different properties from those required to metals used in bulk deformation, not only because this type of deformation results from the application of tensile stresses, not compression, but also because the work elements in the rolling mill are mostly exposed parts; hence their finishing needs to be faultless. It is therefore necessary to use sheet-metal characterization criteria which overcome the mere mechanical characterization (determination of flow curves, determination of the strain sensitivity index and of the strain-rate sensitivity index, definition of hardness, etc.) to get to the heart of the forming process; in other words, it is necessary to investigate the "formability" properties of the material [5]. A powerful formability assessment tool is represented by the Forming Limit Curve (FLC) [6] which expresses the limit condition to the main real in-plane strains in sheet-metal forming (ε_1,

ε_2), once the limit condition is passed, undesired fracture or necking phenomena take place. Thanks to this knowledge, the effects of enforced strains can be predicted and the setting of a forming process based only on empirical considerations or on "trial and error" methods, can be avoided. For this reason, the FLC is a very useful element in the planning phase and control phase of the forming process. There are several standard and non-standard tests which aim at defining and evaluating the formability of sheet-metals (the Erichsen test, the Nakazima test, the Marchiniak test, etc.). Among these tests, the Nakazima test, simulating the behaviour of a planar strain deformation of a sheet-metal under real process conditions, is the most targeted at determining the FLC.

Formability testing inevitably necessitates a considerable strain on resources, as well as the application of sophisticated strain analysis and strain measurement techniques. It is mainly for these reasons that research for the definition of the FLC is mostly conducted under controlled laboratory conditions. Experiment-based research has recently been supported by sophisticated numerical techniques grounded on analytical approaches to the problem of sheet-metal plasticity. These numerical techniques can be used as a modern analysis tool to obtain formability parameters of sheet-metals in a less time-consuming and more cost-effective way. To give an example, significant developments made in the calculation codes based on the finite element method (FEM), suggested the possibility of simulating formability tests on the computer with a consequent drastic reduction in the time and equipment necessary to obtain an operational assessment of formability. This makes the FLC analysis process much more direct and immediate, and therefore applicable also to contexts where not all the necessary equipment for experimental testing is available. Of course, a similar approach needs to undergo a preliminary testing phase before being for its assessment.

4.1.1 Formability

The term refers to the different types of sheet-metal forming processes a workpiece can be subject to. These processes, in case of complex shapes, may vary depending on the parts of the workpiece taken into consideration.

Bending is one of the basic types of sheet-metal forming; in this case, the deformation takes place only in the area of the workpiece where forces are applied modifying its bending radius. In bending, the typical strain state, corresponds to the existence, on the plane of the sheet, of an in-plane strain direction coincident with the bending axis.

In stretching (or stretch-bending), only a specific region of the metal-sheet undergoes deformation, the remaining part is, instead, totally clenched by a blankholder acting in the region surrounding the strained area. The forming process may be carried out through direct action of a pressurised fluid (hydroforming process), in this case no friction phenomena are present on the stretched area; it can, otherwise, be performed by a punch pressed into the workpiece with force (punch stretching), in this case, friction phenomena between the surfaces of the elements in contact produce effects of major importance on the process. The typical strain state in this type of forming process is distinguished by the fact that the two main in-plane strains are both positive.

The deep drawing process produces a deformation state characterized by the existence of a main drawing direction, on the plane of the sheet, along which the deformation is positive, and of a second drawing direction, along which the deformation is negative. The reduction in the blank planar perimeter (circumferential compression), visible in a drawing operation, is a most evident example of this. In this case, the compressive strength has an impact on the workpiece formability, especially when the blank undergoing the process is clenched only on one side or not clenched at all by blankholder and die. The circumferential compression resulting from blank perimeter reduction, causes the formation of wrinkles, ending in the discarding of the piece. In industrial sheet-metal forming processes, these basic types of deformation are used, separately or simultaneously, with a general predominance of tensile stress states.

The development of modern technologies and of increasingly complex processing systems, has led to the necessity of a highly sectoral knowledge of the properties of worked materials. For those involved in bulk and sheet-metal processing, not only the the mechanical properties of the specific metal used, but also, and very often, the behaviour of that metal under certain strain conditions need to be present in specialised scientific literature. For this reason, a new field of research was developed dealing with the investigation of these metal properties. To do so, a series of tests have been developed drawing on many of the most common processes the materials may undergo. Some of the most widespread are reported below.

4.1.2 The forming limit diagram

The Forming Limit Diagrams (FLD) represent a convenient and widely used tool for classifying formability and evaluating sheet metal forming processes. Sheet-metals formability is often referred to as the ability of metal to undergo plastic deformation within desired limits, without necking or cracking.

Each type of sheet metal can be deformed up to a certain limit, which is generally marked by the onset of the necking zone, a zone where the tensile deformation has reached the point in which a localized thinning of the metal takes place, eventually leading to a possible fracture. A well known method for describing this limit is by using the forming limit diagram, a diagram showing the deformation trends on the main surface of the sheet-metal. FLDs are a key guidance instrument in sheet-metal forming. Once a certain mode of forming has been chosen, the FLD associated to this mode shows the limits of the main strain the sheet-metal is exposed to.

The diagram represents the major strain on the ordinate and the minor strain on the abscissa, both characteristic of how a certain section of the sheet metal has been strained after forming. In forming limit diagrams, zones indicating the different probabilities to obtain an undamaged workpiece, can be identified. The so called "safe zone" is the zone where failure in forming is extremely improbable. The "highly improbable failure" zone still represents

a zone characterized by very low fracture probability; whereas in the "highly probable failure" zone the probability of fracture is very high. The two probability zones enclose the "marginal zone" where the probability of failure is high enough for the process to be considered not safe.

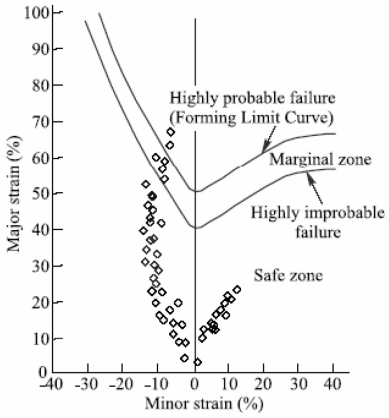

Figure 4.1 – Safe zone, failure zone and marginal zone in FLD

The FLD concept was introduced by Keeler and Backofen who, with their tensile tests, developed the right side of the graph, where only positive minor stains are plotted, later Goodwin extended the diagram introducing also negative minor strains. On the right side of the FLD, circles will acquire the shape of ellipses wider in all directions compared to their original dimensions. This the region of biaxial stretching (traction-traction) and of balanced biaxial tension , along the 45° quadrant bisector, where circles expand with no shape alteration. Conversely, on the left side of the diagram, little circles will acquire the shape of ellipses wider only in one direction; this is the region of tension-compression strains which are characteristic of deep drawing and uniaxial tension. On the vertical axis we have an plane strain state: circles extend only in one direction with no other size alteration.

As shown in the previous figure, FLD was developed through the contribution of several types of formability tests. Among them, one of the most widely used is the Nakazima test. In this test, metal-sheets of different size are used, with a view to plotting a limit curve covering the whole forming limit diagram. The

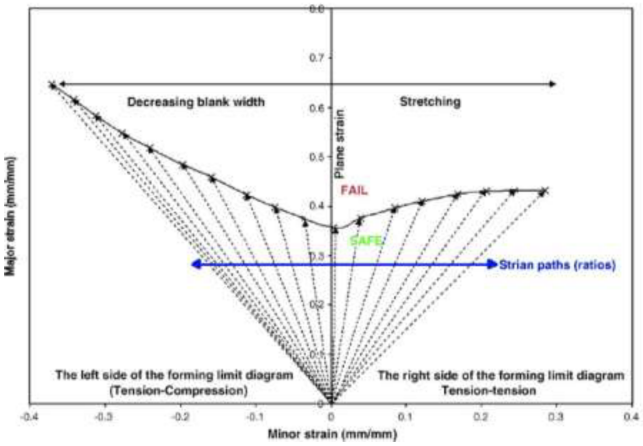

Figure 4.2 – Test conditions in FLD

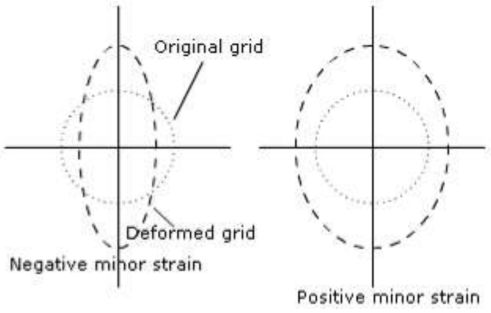

Figure 4.3 – Strain effects. Respectively: negative strain effects and positive strain effects

aim is to obtain both uniaxial tensions, marked as dots in the left side quadrant, where minor strain is negative, and in-plane or biaxial tensions, marked as dots in the right quadrant, where both minor strain and major strain are positive. The region below the curve is considered the safe zone for each type of strain applied, whereas the region above the curve represents the zone where fracture or necking are likely to take place. With a view to guaranteeing a safety margin, another curve , named "safe" curve, is generally plotted in the graph shifted of 10% below the forming limit curve (FLC); the higher is the curve in the graph, the better its formability. Data for the definition of forming limit conditions have been collected for several different work materials, not only

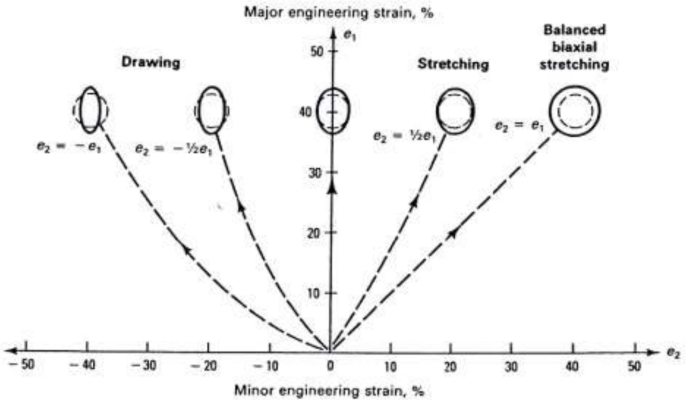

Figure 4.4 – Some major and minor strain configurations

through experimental tests but also through the analyses conducted on the products of industrial processes. The results revealed an excellent correlation among them, thus demonstrating that the forming limit curves plotted after experimental tests are valid tools to evaluate sheet-metal processing in real industrial application.

4.1.3 Influence of material properties on formability

Very often, when selecting the material for a certain application, a compromise between the functional properties required for the final product and the formability properties of the material to use, needs to be found.

Among the properties of the alloy, apart from those of the base metal, the type and quantity of alloying elements have an important influence. Moreover, full account should be taken of the starting conditions of the sheet-metal, since these are dependent of the production process, of heat-treatments and of possible cold rolling processes previously endured. Specifically, the rolling process can produce a certain level of anisotropy, which is non-negligible in plastic deformation processing of sheet-metal. Anisotropy entails a different reaction of the material to the application of tensile stresses; its effects may therefore vary depending on the direction taken into consideration, not only with respect to the planar direction of the sheet (planar anisotropy) , but also normal to it,

with respect to its thickness (normal anisotropy).

4.1.4 Anisotropy of sheet-metals

Sheet-metal properties, such as formability, are generally dependent of many factors; and, among them, the properties of the standard alloy have crucial importance.

Sometimes, however, some of their properties, although homogeneous in the material, show anisotropy. This may be due to the material crystallographic structure, or to certain production processes such as rolling, where the the grains of the sheet have no random crystallographic orientation but a preferential orientation.

In order to highlight the anisotropic behaviour of a sheet-metal, we usually analyse the variation of a selected property at directions showing a different orientation from the rolling direction (usually at 0°, 45° and 90°). For this purpose, we make use of a tensile test in which the selected specimens have their axis respectively parallel, normal and or at 45° with respect to the direction of rolling.

Normally, to compare tests having different orientation of the axes, the specimen is stretched until a set point is reached, generally corresponding to 15-20% of the initial length.

Anisotropy influences sheet-metal both in-plane strains and out-of-plane strains (thickness reduction). In particular, the variation in the plastic behaviour of the material according to direction, can be determined through the introduction of the Lankford parameter, or plastic anisotropy factor. This parameter, with regard to to the strain section, is defined as:

$$r = \frac{\varepsilon_w}{\varepsilon_t} = \frac{\ln\left(\frac{w}{w_0}\right)}{\ln\left(\frac{t}{t_0}\right)} \tag{4.1}$$

where ε_w is the real strain related to the width of the specimen and ε_t the real strain related to its thickness, as it can be easily understood in Figure 4.5.

If we impose the volume constancy condition for a plastic deformation, the in-plane strain in length can be taken into consideration to replace the in-plane deformation in width. The plastic anisotropy factor will vary depending on the direction considered and it will be indicated by a subscript representing the angle formed by the direction of rolling and the axis of the specimen. The subscript will be respectively: r_0, in case they are parallel, r_{90}, in case of normality, and r_{45} in case the two axes are inclined at 45° from each other.

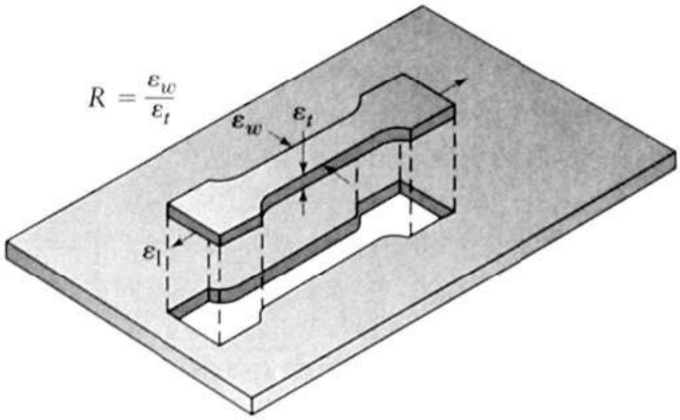

Figure 4.5 – Plastic anisotropy factor

With respect to the definition of r the possible combinations are the following:

- material isotropy: $r_0 = r_{45} = r_{90} = 1$
- planar anisotropy: $r_0 \neq r_{45} \neq r_{90}$
- normal anisotropy: $r_0 = r_{45} = r_{90} \neq 1$
- planar and normal anisotropy: $r_0 \neq r_{45} \neq r_{90} \neq 1$

To split the two contributions we define two coefficients:

- the average normal anisotropy factor:
  $r_m = \dfrac{(r_0 + 2r_{45} + r_{90})}{4}$

- the planar anisotropy factor:
  $\Delta r = \frac{(r_0 - 2r_{45} + r_{90})}{2}$

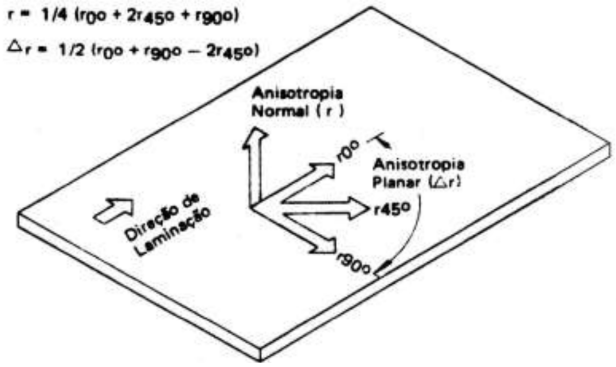

Figure 4.6 – Normal and planar anisotropy

4.1.5 Influence of anisotropy on sheet-metal forming

High values of normal anisotropy factor are signs of good resistance to sheet-metal cross-section reduction and, therefore, of good formability. Specifically, values higher than one denote a tendency to plastic flow on the plane of the sheet, a property to be considered desirable to avoid the insurgence of necking with a consequent increase of uniform strain.

To ensure satisfactory drawability, high values of r_n and ad low values of Δr are required. A high value of the normal anisotropy factor favours a wider strain distribution along the plane of the sheet-metal, thus avoiding excessive cross-sectional reduction which could cause cracking. Planar anisotropic materials are exposed to the problem of earing during deep drawing.

In this case, there is an an increase in material waste and an additional shredding operation, resulting in higher production costs, will be needed. In general, the effect of anisotropy is highly visible at room temperature whereas it tends to diminish as temperature increases.

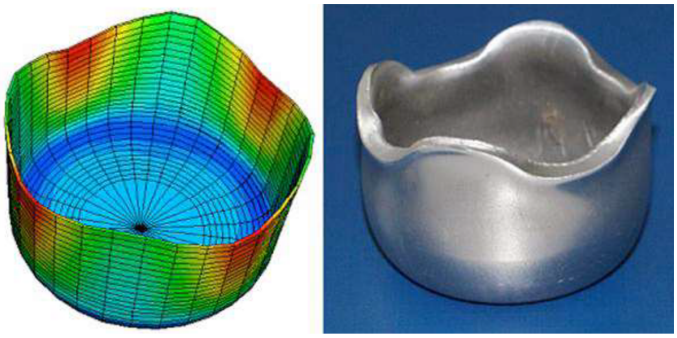

Figure 4.7 – Earing in deep drawing

4.2 Experimental research activity

The simplest test used for the characterization of the strain behaviour of a material, is the tensile test, which, nevertheless, is only valid for uniaxial tension.

When evaluating other more complex deformation processes, a test involving all the directions of the applied tensions, or at least two of them, as in the case of biaxial tension, will be required. Among the latter, the Nakazima test is one of the most commonly used. This test, making the use of tensile specimens of different thickness, permits to analyse the material under several different strain conditions.

In tensile testing, for the purpose of strain deformation measurement (Figure 4.8), an optical measuring technique based on the digital correlation of speckle images, has been used. In Digital Image Correlation (DIC), pigmentation on the surface of the specimen is obtained through random spray printing of black and white speckles: the calculation of the planar displacement of the intersections of the elements of a virtual grid drawn on the specimen, has allowed to retrace the map of the shifts on the two-dimensional (2D) surface of the specimen. Conversely, for the measuring of strain deformations in formability testing, a semi-automatic optical technique has been chosen, based on the measurement of a grill stamped on the specimen surface through ink transfer: the determination of spacial displacement of the intersections of the grid,

resulting from a stereoscopic system of two cameras, calibrated on three dimensions on the basis of the Heikkila algorithm, has permitted to reconstruct the three-dimensional (3D) surface of the specimen.

In both cases, the right Cauchy-Green deformation tensor has been created, and it has then allowed to obtain the logarithmic deformation field. The results of both tensile tests and Nakazima tests, together with the optical technique, enabled to achieve the mechanical properties of the analysed alloys: ultimate tensile strength (R_{max}), yield strength at 0,2% of plastic deformation (R_y), elongation after fracture (A%) and the forming limit diagram (FLD).

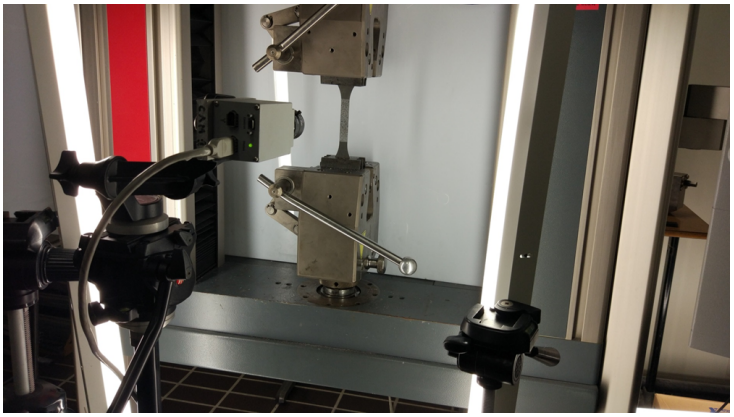

Figure 4.8 – Tensile test set-up

4.2.1 Experimental techniques

Sheet-metal properties, such as formability, generally depend on several factors [7, 8]. Among these factors, the properties of the standard alloy have a fundamental importance. Sometimes, however, some properties are dependent of the loading conditions, as for example the loading speed, and are influenced by temperature [9]. The flow curves result from tensile tests carried out on specimens of a proportional size taken at full thickness from the sheet-metal, with a recumbency of 0°, 45° and 90° with respect to the direction of rolling (UNI EN 10002). The tests have been conducted under shift control, with a crossbeam speed of 30mm/min (5 and 0,5 mm/s). For each orientation, three

trials have been carried out for the purpose of evaluating the repeatability of the mechanical properties. The Nakazima test consists in deep drawing rectangular tensile specimens of different width using an hemisferic punch, a die and a blankholder, until necking or fracture are reached (Figure 4.9). By varying the width of the specimen and the lubrication condition, several different levels of deformation are obtained, from those typical of deep drawing to those resulting from stretch forming. As the ratio between the original dimensions of the sides of the blank varies, different strain states can be observed: if, in fact, for a sides ratio equivalent to 1:1 (original square blank) the blankholder exerts its pressure on the whole flange of the blank and the conditions for a balanced biaxial stretching are reached; as the sides ratio changes, and, therefore, as the blankholder exerts its pressure on an increasingly restricted blank flange, the stretching conditions become progressively unbalanced.

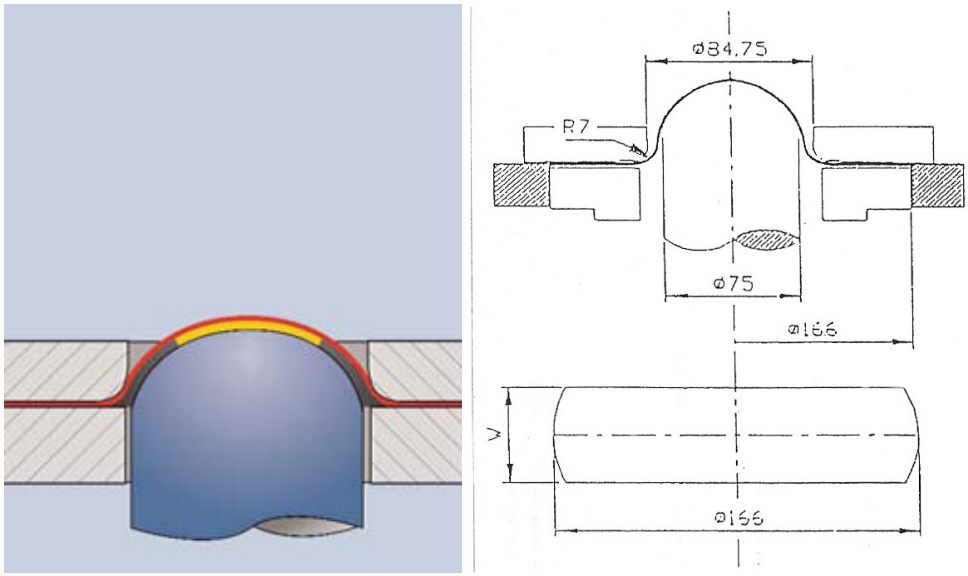

Figure 4.9 – Nakazima test

The advantages of the Nakazima test consist in the simple tools and simple shape of the specimen, as well as in the possibility to mark out the whole forming limit curve domain. Its disadvantages are, instead, represented by the the probability of causing wrinkling and rippling in the material, and in the

possibility of making measurement errors, since wrinkling occurs on a surface which has been curved by the action of the hemispheric punch, hence on a non-planar surface. Thanks to the use of a stereoscopic optical technique, the risk to incur into this type of measurement error has been eliminated.

4.2.2 Optical methods

Strain measurement is based on the principle of the calculation of the displacement of the intersections of a grid [10, 11], initially evenly spaced, inprinted on the non-strained specimen and integral with it during the tensile test or during the Nakazima test. The surface of the specimen is recorded by a stereoscopic two-camera system CMOS with a resolution of 1280×1024 pixels (Pixelink ®B371F) at 25 frames per second (fps). The cameras are calibrated on three-dimensions using the Heikkila algorithm with a mutual reference point. In cameras calibration a 50x50 dot array grid with 1mm pitch is recorded from different positions by the two cameras.

Table 4.1 – Calibration results

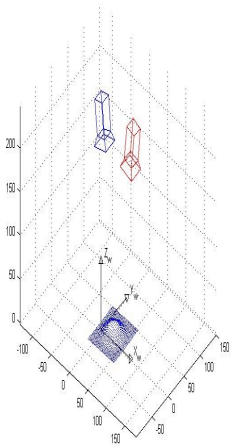

Camera 1		Camera 2	
f_x	4087.54	f_x	4090.60
f_y	4086.68	f_y	4089.25
γ	0	γ	0
c_x	655.79	c_x	640.7
c_y	479.21	c_y	510.36
Extrinsic parameters			
α_1	-0.0107	T_x	-71.36
α_2	0.2637	T_y	-2.91
α_3	0.00784	T_z	0.25

Using a calculation program developed in Matlab®, intrinsic parameters (focal length, optical center coordinates and skew coefficient), extrinsic parameters (rotation matrix and position vector) and the radial distortion coefficients for the two cameras have been derived. These parameters have then been used for the calculation of the triangulation in stereo vision necessary for the reconstruction of the surface of the specimen. Table 4.1 shows a graphic representation of the position of the two cameras with respect to the specimen surface resulting from the stereoscopic estimation made using the parameters enlisted in the chart. In Figure 4.10 displays two specimens used in tensile tests with and without speckle pattern application.

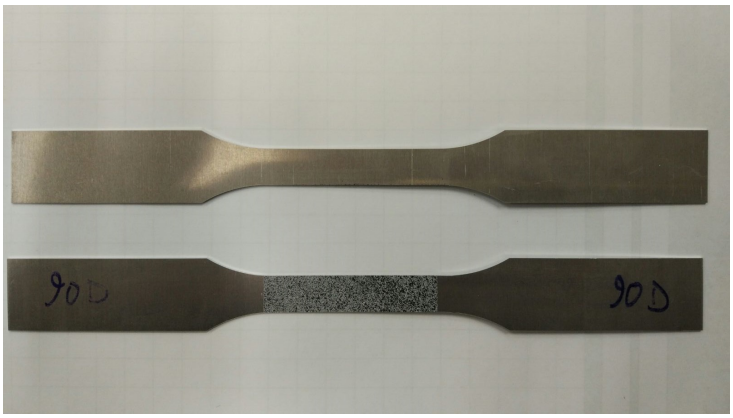

Figure 4.10 – Specimen used in tensile tests with and without speckle pattern application

The images captured for the Nakazima test specimens are displayed in Table 4.2. As shown in Figure 4.11, three types of specimens of different width have been used.

The captured images have been processed using a semi-automatic program in Matlab®for pixel coordinates of the cross centers recognition. The program is based on an algorithm in which three main phases can be distinguished:

- image segmentation,
- localization of the center of the marker,
- sorting of centres according to their referential position

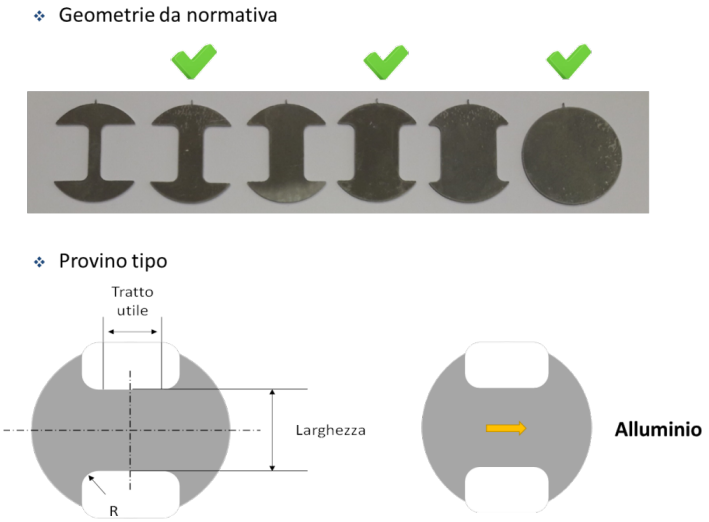

Figure 4.11 – Standard format specimens for aluminium formability test

Table 4.2 – Deformed specimens after Nakazima test

	Mappa di ε_1 proiettata sul provino	Mappa di ε_2 proiettata sul provino
Geometria 1	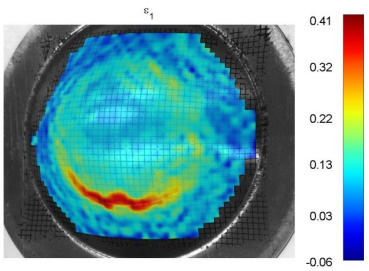	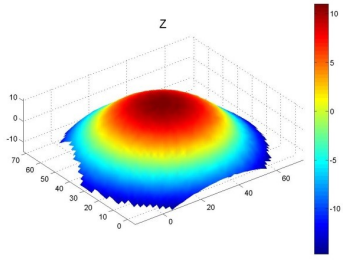
Geometria 2	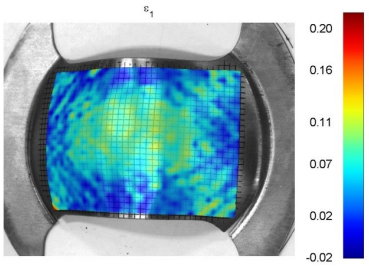	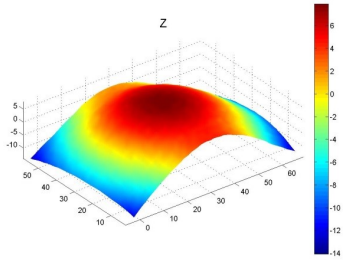
Geometria 3	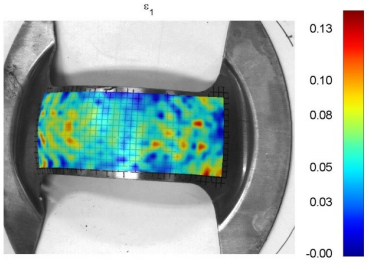	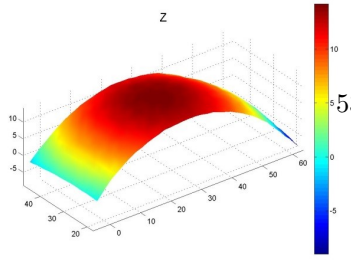

Image segmentation enables to determine which pixels belong to the marking grid and which to the background. To do so, a gray level for discrimination needs to be set. This level represents the threshold above which each pixel is pale enough to belong to the background (the surface of the specimen) and below which each pixel is dark enough to be assigned to the marking grid. We can estimate the threshold level by duly processing the histogram of the picture; this operation is possible and meaningful only when the histogram shows a bimodal trend.

Once the image is converted into a binary image through the use of an algorithm based on the research of polygons Convex Hull, the coordinates of the center of the intersections of the calibration grid, can be determined . The sorting problem refers to the process by which a correlation is established between the markers on the specimen and the respective referential coordinates. In square mesh grids, each marker has a corresponding couple of integer coordinates. This is a crucial passage in order to detect the correspondence between the two cameras intersections.

In Figure 4.12 the sequence of the operations carried out to obtain an image of the Nakazima test, is shown: the binarized image, the map of the convex polygons used to detect the center of the intersections and the original image with the highlighted centers, are all visible. The results of the automatic process need to be filtered and optimized in order to eliminate false intersections and insert any undetected crossing due to non-uniform lightening.

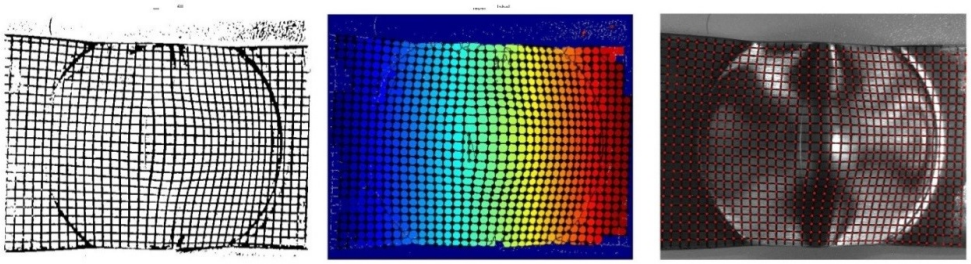

Figure 4.12 – Intersection identification process

Starting from the pixel coordinates, exploiting the referential coordinates

automatically assigned on the two images, pairs of corresponding points are determined and, by means of a stereoscopic calculation based on the pinhole model ans on epipolar geometry, the 3D surface of the specimen is traced and displaced as a cloud of points. As shown in Table 4.3.

Table 4.3 – 3D surface – Nakazima test

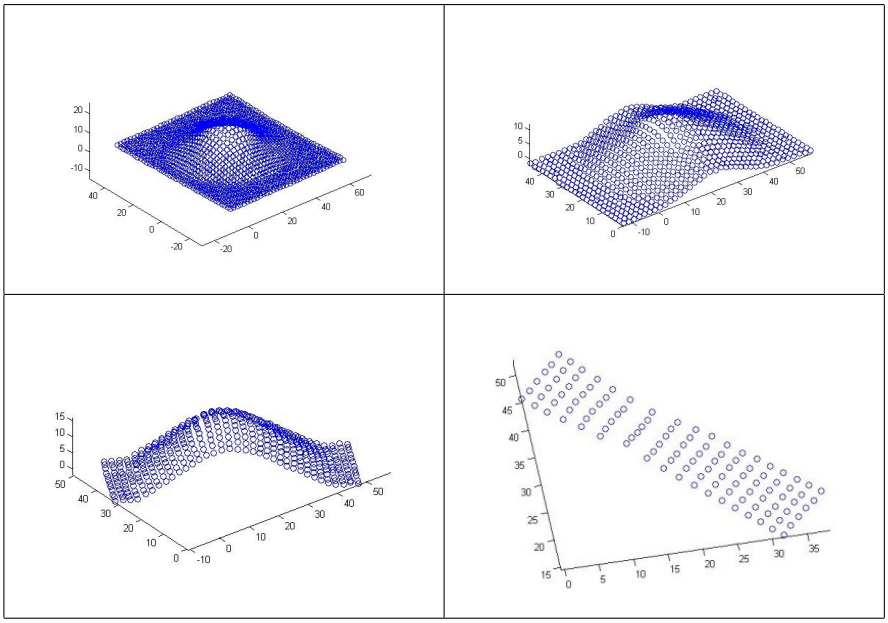

Comparing the marker coordinates in the deformed configuration with those in the non deformed configuration, according to the theory of large deformations, by defining the shape functions, the gradient tensor of deformation has then been calculated. From the gradient tensor, the Cauchy-Green right tensor has been obtained, then allowing to determine the field of logarithmic deformations. In Table 4.4 the map of the principal membrane strains ε_1 and ε_2 calculated for two Nakazima tests, is displayed.

Table 4.4 – Maps of principal strains

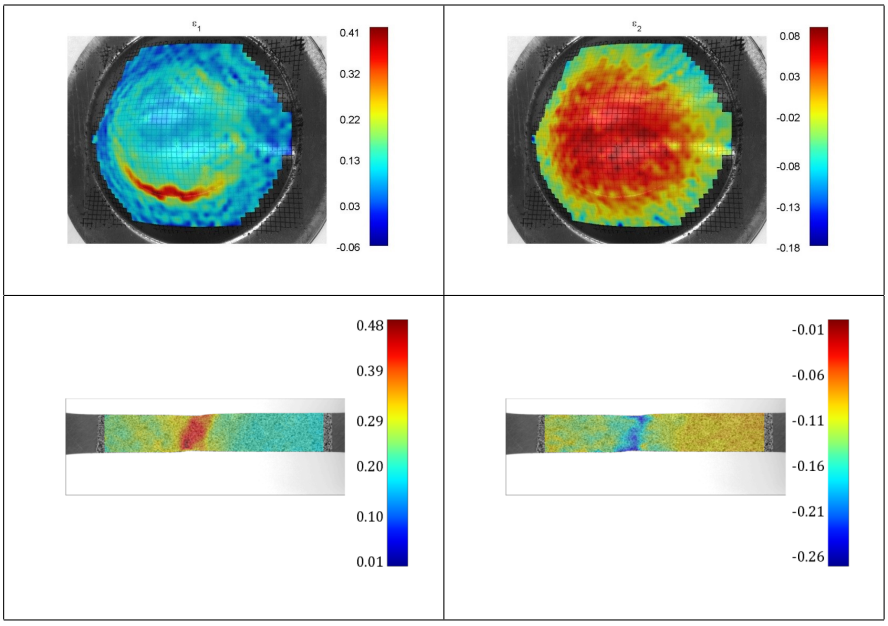

The maps of the principal strains have been plotted directly on the captured images to identify the exact position of the points of interest for further processing. By imposing the volume constancy, is also possible to estimate the exact value of the strains with respect to the thickness.

4.3 Results

4.3.1 AA 5182

Figure 4.13, Figure 4.14, Figure 4.15 show the experimental flow plastic curves obtained from the tensile tests on AA5182. Three tensile specimens were taken from the coil for each investigated direction, i.e. 0°, 45° and 90° with respect to the LD (longitudinal direction i.e. the rolling direction). The main mechanical characteristics such as yielding stress, ultimate stress, elongation at break and Lankford parameter were reported under each flow plastic curve.

Figure 4.16 shows a comparison among the averaged values of the tests results

on all the three directions. The calculated normal and planar anisotropy values are reported at the bottom of the same figure Figure 4.15.

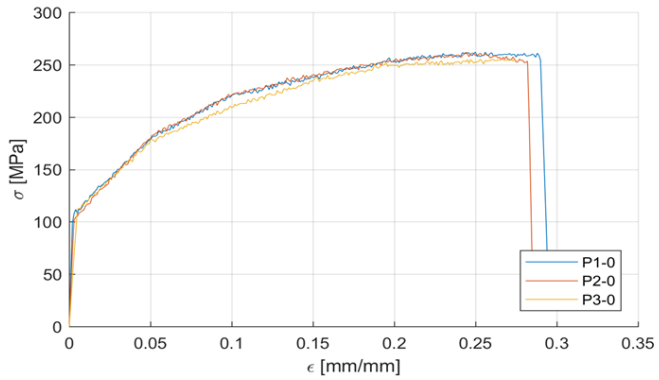

0°	testA	testB	testC	MEDIA	Dev.Std.
σ_S [Mpa]	112,55	117,82	110,61	**113,66**	3,73
σ_R [Mpa]	264,89	265,74	268,42	**266,35**	1,84
A [%]	28,50	28,72	27,63	**28,28**	0,58
r	0,642	0,648	0,663	**0,651**	0,011

Figure 4.13 – AA5182 0° flow plastic curves

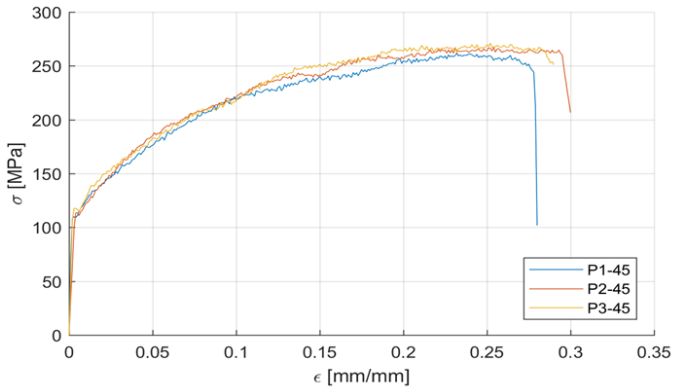

45°	testA	testB	testC	MEDIA	Dev.Std.
σ_S [Mpa]	111,81	119,1	113,77	**114,89**	3,77
σ_R [Mpa]	263,55	264,39	267,06	**265,00**	1,83
A [%]	29,42	29,65	28,52	**29,20**	0,60
r	0,769	0,776	0,794	**0,780**	0,013

Figure 4.14 – AA5182 45° flow plastic curves

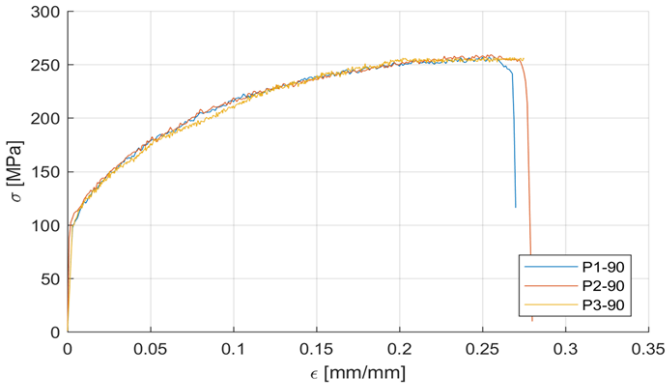

90°	testA	testB	testC	MEDIA	Dev.Std.
σ_S [Mpa]	113,48	111,52	118,79	**114,60**	3,76
σ_R [Mpa]	265,58	265,20	264,80	**265,19**	0,39
A [%]	28,41	28,64	27,55	**28,20**	0,57
r	0,661	0,667	0,682	**0,670**	0,011

Figure 4.15 – AA5182 90° flow plastic curves

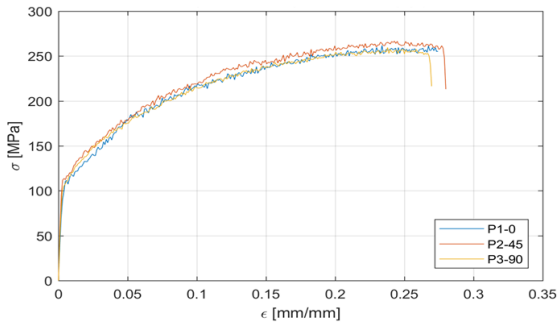

	0°	45°	90°
σ_S [Mpa]	113,66	114,89	114,60
σ_R [Mpa]	266,35	265,00	265,19
A [%]	28,28	29,20	28,20
r	0,651	0,780	0,670

	testA	testB	testC	MEDIA	Dev.Std.
r_0	0,642	0,648	0,663	**0,651**	0,011
r_{45}	0,769	0,776	0,794	**0,780**	0,013
r_{90}	0,661	0,667	0,682	**0,670**	0,011
Rm	FATTORE ANISOTROPIA NORMALE			**0,720**	
ΔR	FATTORE ANISOTROPIA PLANARE			**-0,119**	

Figure 4.16 – AA5182 summary and characteristic parameters

Forming limit curves were obtained by interpolating the maximum major strain value of the safe points of all the different tests which were led.

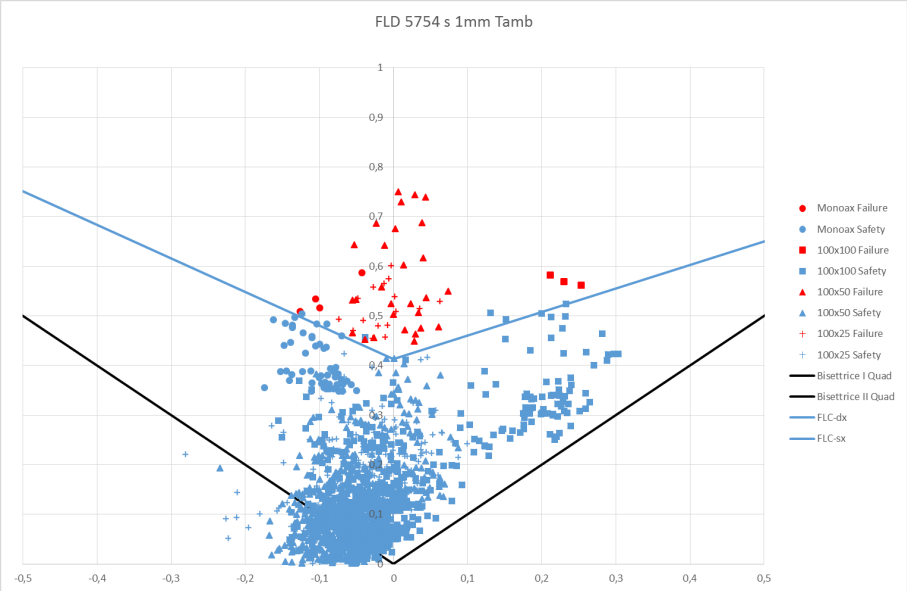

Figure 4.17 – AA5182 Forming Limit Diagram

4.3.2 AA 5754

Figure 4.18, Figure 4.19, Figure 4.20 show the experimental flow plastic curves obtained from the tensile tests on AA5754. Four tensile specimens were taken from the coil for each investigated direction, i.e. 0°, 45° and 90° with respect to the LD (longitudinal direction i.e. the rolling direction). The main mechanical characteristics such as yielding stress, ultimate stress, elongation at break and Lankford parameter were reported under each flow plastic curve.

Figure 4.21 shows a comparison among the averaged values of the tests results on all the three directions. The calculated normal and planar anisotropy values are reported at the bottom of the same figure Figure 4.20.

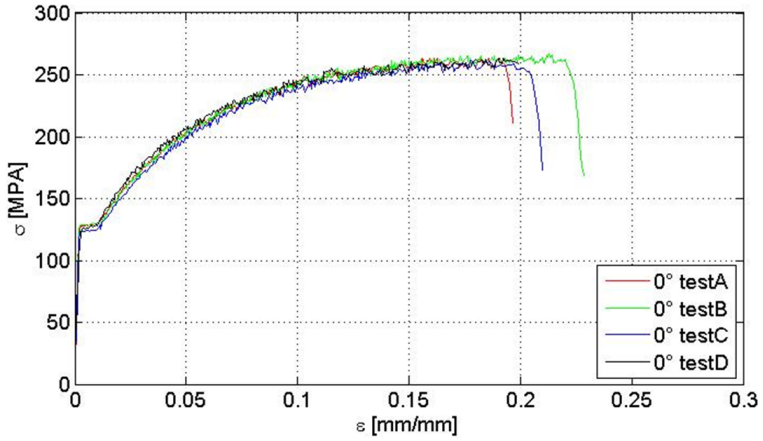

0°	testA	testB	testC	testD	MEDIA	Dev.Std.
σ_S [Mpa]	128.23	129.18	124.45	126.34	**127.05**	2.10
σ_R [Mpa]	263.62	266.80	261.18	263.19	**263.70**	2.33
A [%]	19.98	22.86	20.99	19.89	**20.93**	1.38
r	0.534	0.545	0.552	0.563	**0.549**	0.012

Figure 4.18 – AA5754 0° flow plastic curves

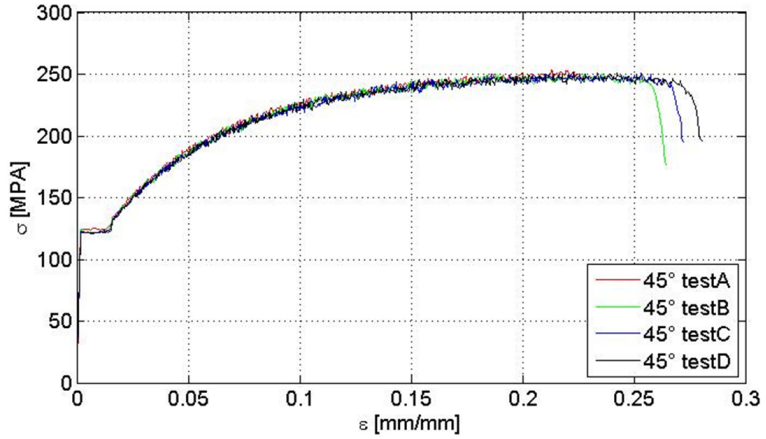

45°	testA	testB	testC	testD	MEDIA	Dev.Std.
σ_S [Mpa]	125.39	122.56	122.08	119.95	**122.50**	2.24
σ_R [Mpa]	253.22	250.10	251.38	256.29	**252.75**	2.69
A [%]	22.76	26.45	27.45	28.26	**26.23**	2.43
r	0.850	1.035	0.965	0.960	**0.953**	0.076

Figure 4.19 – AA5754 45° flow plastic curves

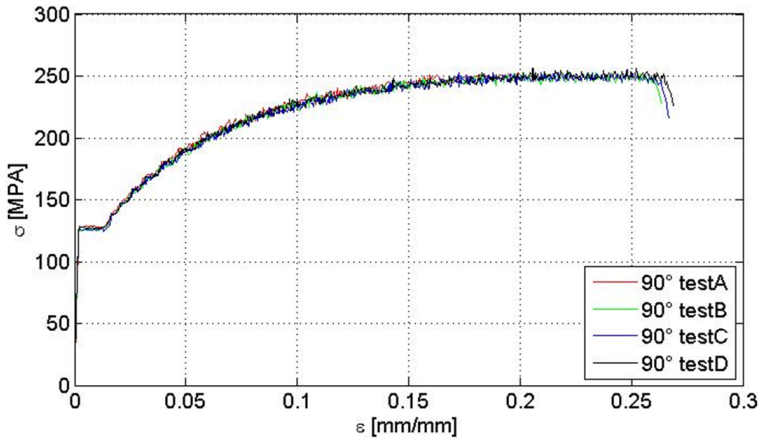

90°	testA	testB	testC	testD	MEDIA	Dev.Std.
σ_S [Mpa]	128.23	126.34	125.39	126.34	**126.58**	1.19
σ_R [Mpa]	252.26	253.77	254.10	256.39	**254.13**	1.71
A [%]	20.46	26.33	26.66	26.89	**25.09**	3.09
r	0.669	0.755	0.754	0.731	**0.727**	0.040

Figure 4.20 – AA5754 90° flow plastic curves

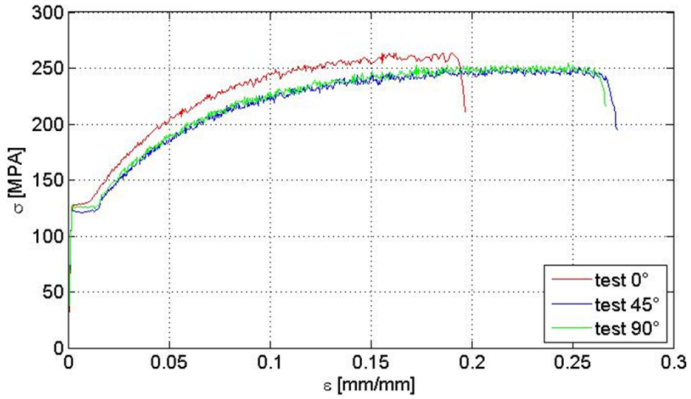

	0°	45°	90°
σ_S [Mpa]	**127.05**	**122.50**	**126.58**
σ_R [Mpa]	**263.70**	**252.75**	**254.13**
A [%]	**20.93**	**26.23**	**25.09**
r	**0.549**	**0.953**	**0.727**

	testA	testB	testC	testD	MEDIA	Dev.Std.
r_0	0.534	0.545	0.552	0.563	**0.549**	0.012
r_{45}	0.850	1.035	0.965	0.960	**0.953**	0.076
r_{90}	0.669	0.755	0.754	0.731	**0.727**	0.040
Rm	FATTORE ANISOTROPIA NORMALE				**0.795**	
ΔR	FATTORE ANISOTROPIA PLANARE				**-0.315**	

Figure 4.21 – AA5754 summary and characteristic parameters

Forming limit curves were obtained by interpolating the maximum major

strain value of the safe points of all the different tests which were led.

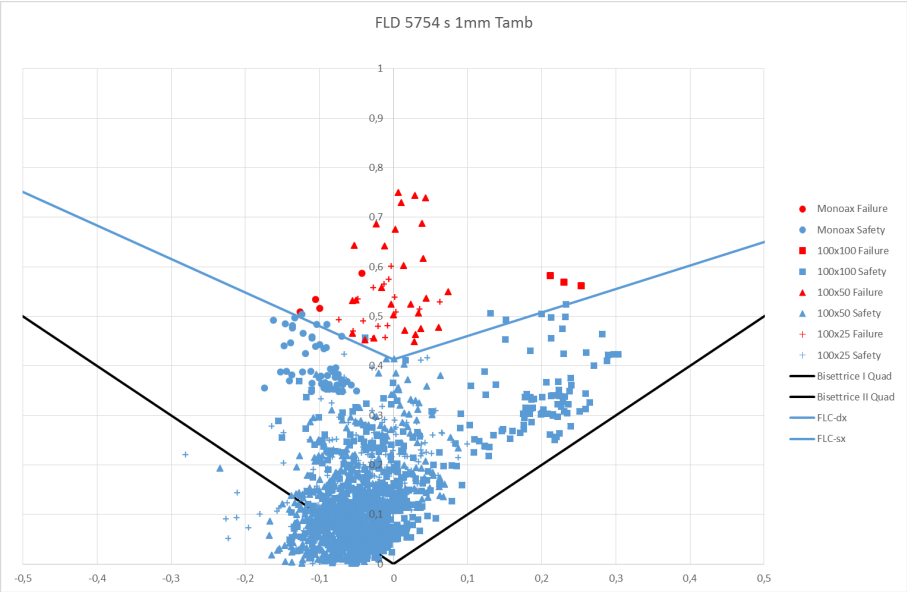

Figure 4.22 – AA5754 Forming Limit Diagram

4.3.3 AA 6016

Figure 4.23, Figure 4.24, Figure 4.25 show the experimental flow plastic curves obtained from the tensile tests on AA6016. Four tensile specimens were taken from the coil for each investigated direction, i.e. 0°, 45° and 90° with respect to the LD (longitudinal direction i.e. the rolling direction). The main mechanical characteristics such as yielding stress, ultimate stress, elongation at break and Lankford parameter were reported under each flow plastic curve.

Figure 4.26 shows a comparison among the averaged values of the tests results on all the three directions. The calculated normal and planar anisotropy values are reported at the bottom of the same figure Figure 4.25.

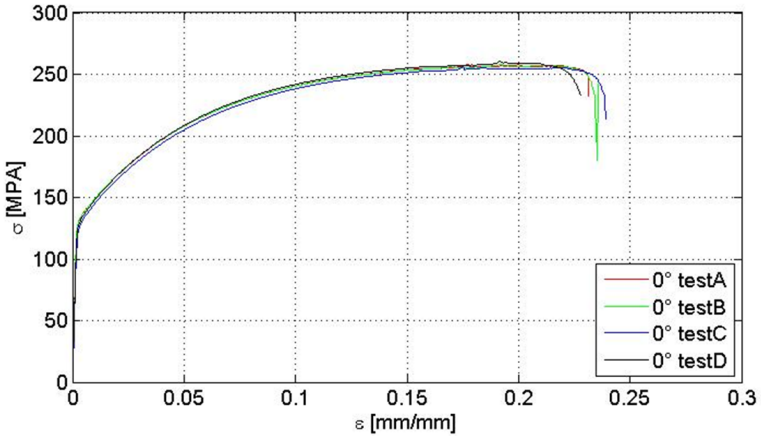

0°	testA	testB	testC	testD	MEDIA	Dev.Std.
$\sigma_{0.2}$ [Mpa]	134.58	134.63	129.58	132.24	**132.76**	2.40
σ_R [Mpa]	258.03	259.98	255.86	261.06	**258.73**	2.29
A [%]	23.49	23.79	23.92	22.78	**23.49**	0.51
r	0.743	0.800	0.727	0.791	**0.765**	0.036

Figure 4.23 – AA6016 0° flow plastic curves

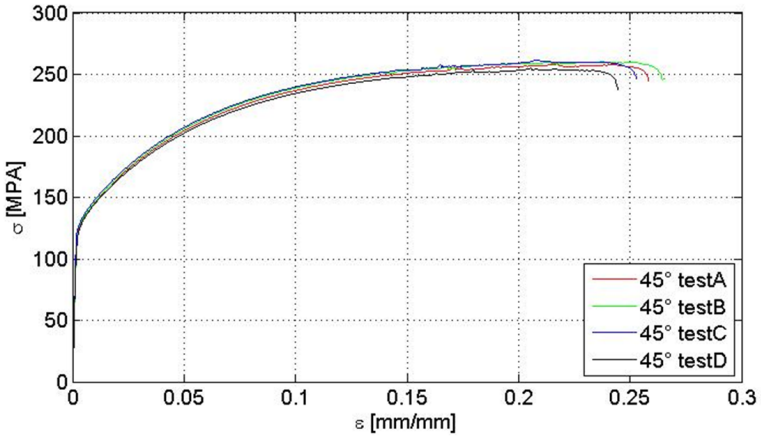

45°	testA	testB	testC	testD	MEDIA	Dev.Std.
$\sigma_{0.2}$ [Mpa]	129.24	130.28	131.36	128.43	**129.83**	1.27
σ_R [Mpa]	258.72	264.39	261.85	255.54	**260.12**	3.84
A [%]	25.84	26.69	25.31	24.44	**25.57**	0.94
r	0.494	0.486	0.499	0.506	**0.496**	0.008

Figure 4.24 – AA6016 45° flow plastic curves

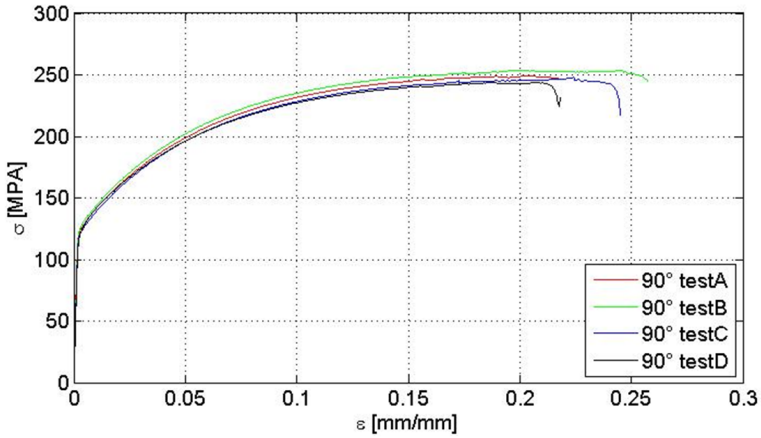

90°	testA	testB	testC	testD	MEDIA	Dev.Std.
$\sigma_{0.2}$ [Mpa]	126.84	128.95	123.92	125.92	**126.41**	2.09
σ_R [Mpa]	249.00	253.93	247.88	246.11	**249.23**	3.35
A [%]	21.72	25.73	24.49	21.89	**23.46**	1.98
r	0.702	0.694	0.696	0.766	**0.715**	0.034

Figure 4.25 – AA6016 90° flow plastic curves

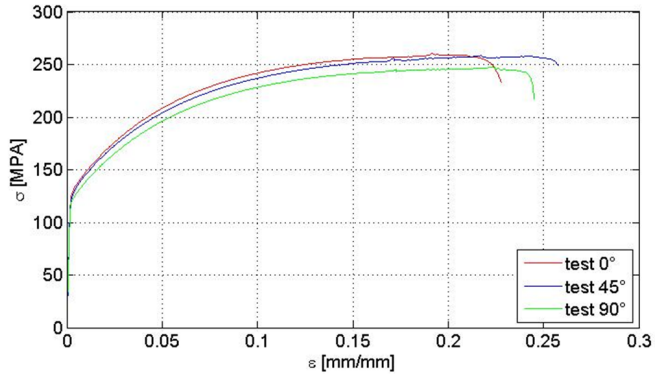

	0°	45°	90°
$\sigma_{0.2}$ [Mpa]	**132.76**	**129.83**	**126.41**
σ_R [Mpa]	**258.73**	**260.12**	**249.23**
A [%]	**23.49**	**25.57**	**23.46**
r	**0.765**	**0.496**	**0.715**

	testA	testB	testC	testD	MEDIA	Dev.Std.
r_0	0.743	0.800	0.727	0.791	**0.765**	0.036
r_{45}	0.494	0.486	0.499	0.506	**0.496**	0.008
r_{90}	0.702	0.694	0.696	0.766	**0.715**	0.034
Rm	FATTORE ANISOTROPIA NORMALE				**0.618**	
ΔR	FATTORE ANISOTROPIA PLANARE				**0.244**	

Figure 4.26 – AA6016 summary and characteristic parameters

Forming limit curves were obtained by interpolating the maximum major

strain value of the safe points of all the different tests which were led.

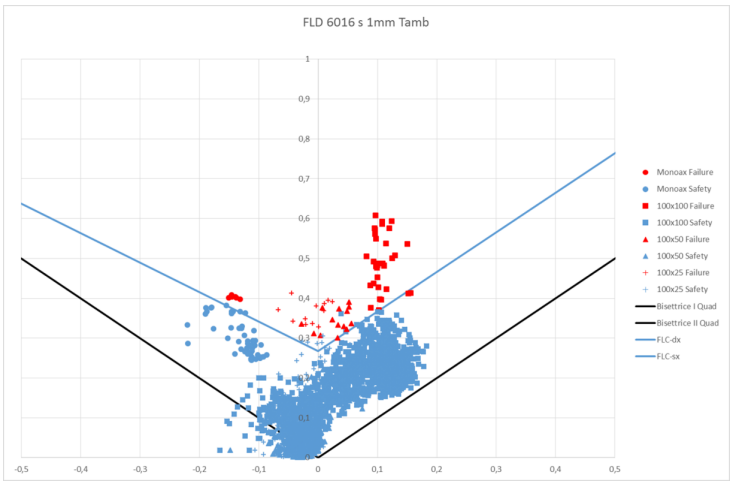

Figure 4.27 – AA6016 Forming Limit Diagram

4.3.4 Hylite

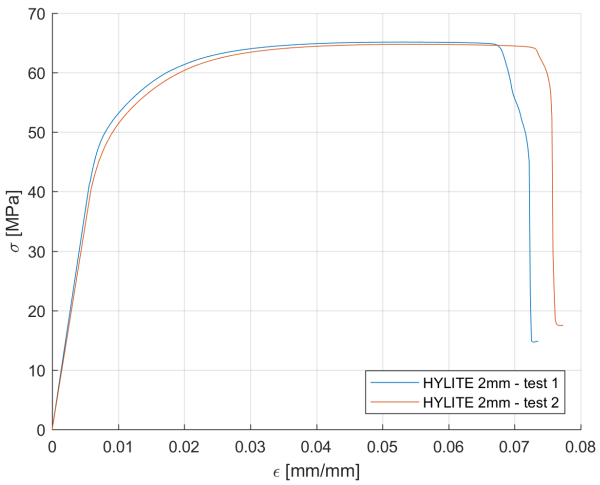

0°	testA	testB	MEDIA	Dev.Std.
σ_S [Mpa]	52,51	50,28	**51,40**	1,58
σ_R [Mpa]	65,68	65,40	**65,54**	0,20
A [%]	5,46	5,58	**5,52**	0,08

Figure 4.28 – HYLITE flow plastic curves

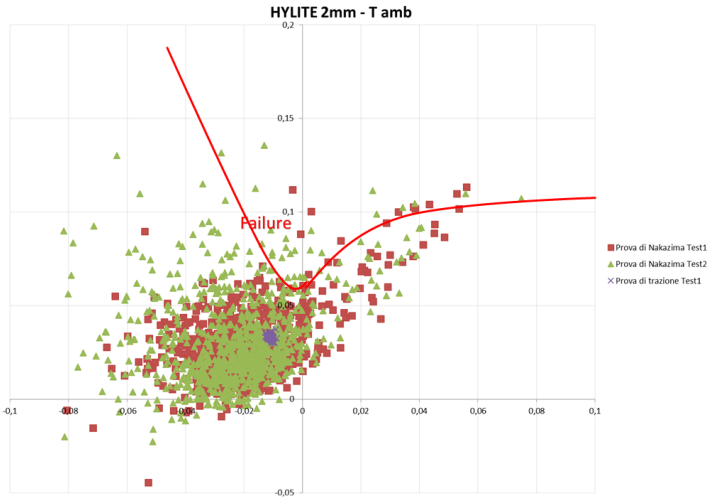

Figure 4.29 – HYLITE Forming Limit Diagram

4.3.5 Dibond

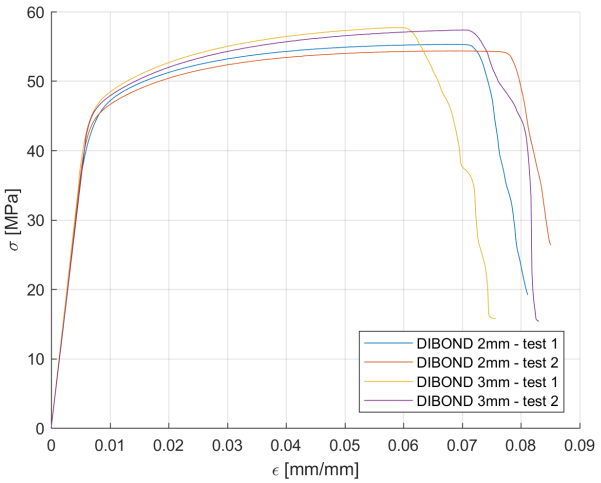

0°	testA	testB	testC	testD	MEDIA	Dev.Std.
σ_S [Mpa]	46,64	45,96	47,97	47,42	**47,00**	0,88
σ_R [Mpa]	55,91	54,83	58,30	57,98	**56,76**	1,66
A [%]	6,85	6,89	6,04	7,15	**6,73**	0,48

Figure 4.30 – DIBOND flow plastic curves

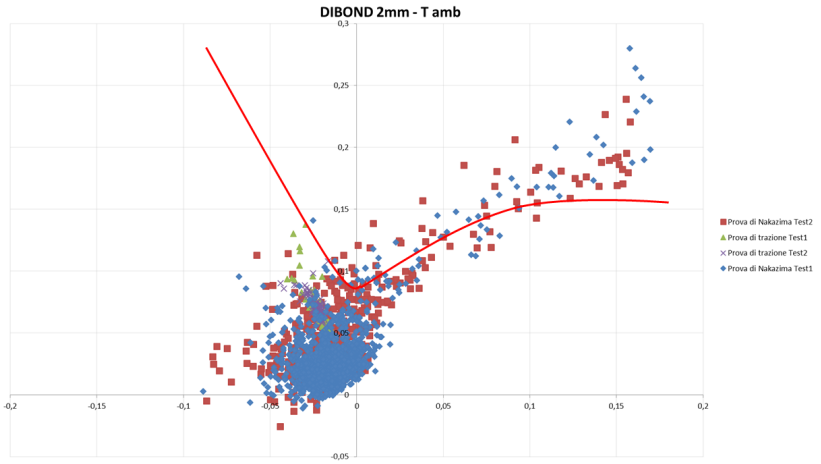

Figure 4.31 – DIBOND 2mm Forming Limit Diagram

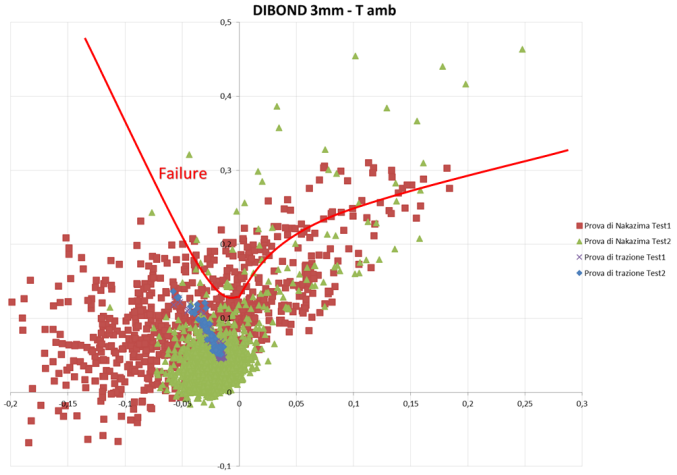

Figure 4.32 – DIBOND 3mm Forming Limit Diagram

4.4 Choosing the material

On the basis of all the characterizations shown above, 5182 and 5754 aluminium alloys were chosen as materials for all future analytical activities. Elongation at break and forming limit diagrams were the key criteria for material selection, with a view to the following step after the rolling process which is the hot forming one. So to recap:

- AA5182 showed a very good average value of the elongation at break (28.53%) with a slight normal anisotropy $R = 0.720$ along the 0° direction, , (in accordance with the 5182 aluminium alloys rolled products behaviour) whereas the planar anisotropy is almost zero, which is indicative of a negligible sensitivity to the "earing probem".
- AA5754 showed a good average value of the elongation at break (24.03%) with a slight normal anisotropy $R = 0.795$ along the 0° direction and a negative light value of the planar anisotropy coefficient. The physical significance being that this material may have become more susceptible to thinning and rupture when it is loaded in a 45° angle relative to the principal directions (RD and TD).
- also AA6016 showed a good average value of the elongation at break (24.17%) with a moderate normal anisotropy $R = 0.618$ along the 0° direction and an elevated value of the planar anisotropy coefficient. The physical significance being that this material may have become more susceptible to thinning and rupture when it is loaded in 0° and 90° angles relative to the principal directions (RD and TD). So AA6016 appears to be highly anisotropic and therefore not suitable for deep drawing.
- HYLITE®and DIBOND®showed very low values of elongation at break (5.52% and 6.73% respectively) and no anisotropy evaluations have been made due to its hybrid nature.

So summarizing, the 5xxx aluminium alloy series showed the best performances as material for stamping process, whereas hybrid materials appeared to be completely unsuitable for stamping processes due to their inadequate formability characteristics.

Particular attention should be paid to a singular phenomenon which arises from the 5754 aluminium alloy. This material, indeed, appears to be highly affected by the Portevin Le Chatelier effect which is marked by the formation of deformation bands that not only leave undesirable traces, with an unacceptable surface quality of the finished product, but also reduce the ductility of the alloy [12, 13]. This phenomenon was discussed at length by the author in [14].

.

Chapter 5

Preliminary numerical modeling

5.1 Introduction

Cold rolling represents a very common process in the industrial practice and a thorough bibliography about this is available. Given the wide variety of feasible products many applications still need a suitable design based on a know-how not available in the rolling handbooks. Cold rolled laminates with variable thickness are an example of such products.

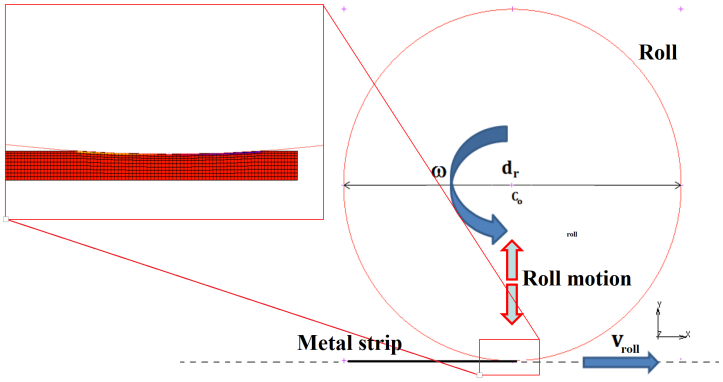

Figure 5.1 – 2D model of profile-rolling mill

Thanks to the evolution of computer technology it is now possible to develop finite element method (FEM) models which can help designers and technicians in evaluating feasibility of products, even before expensive experimental tests have been led. The main aims of the present research are reported below:

- establish the quality of thickness of the rolled product;
- analyse the material behaviour near the zones with thickness variation;
- quantify the deformation effects due to the removal of pay-off and tension reels.

Preliminary numerical 2D and 3D analysis have been recently discuss by Mattucci [29] and Vizzarri [30]. The cited master thesis only debated the development of bi- and three-dimensional finite element rolling models in MSC Marc. So the present research activity is really a follow-up to the cited work.

5.2 2D and 3D analysis

5.2.1 State of art

Previous studies on profile-rolling (2D) and patch-rolling (3D) only evaluated a brief behaviour of the material undergoing the process. In summary, the material showed a good response and results appear to be realistic and consistent with practice.

Two-dimensional case studies showed the right position of the neutral point within the contact arc length (Figure 5.2) and that the material seems to be easily worked into different thicknesses by only moving the upper work roll up and down as shown in Figure 5.1.

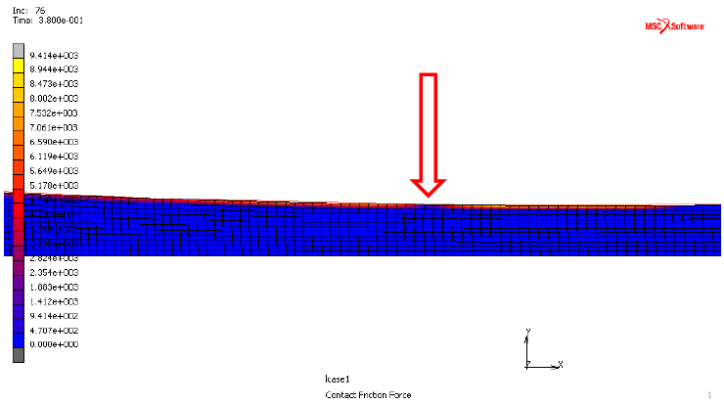

Figure 5.2 – Position of neutral point in profile rolling

Three-dimensional analysis, instead, pointed out the importance of pay-off and tension reels to reduce rolling forces. Moreover, looking at the plastic strain component averaged through the thickness of the plate, a thinning zone immediately follows the over-thickness area (Figure 5.3).

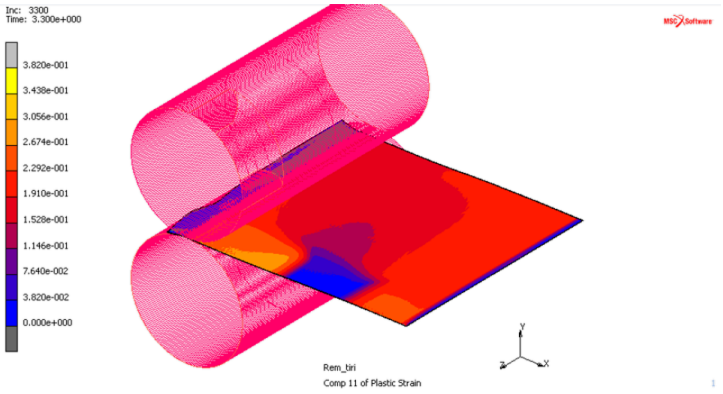

Figure 5.3 – 3D model of patch-rolling mill

This phenomenon can be interpreted as the material's attempt to recover by itself, in the lengthwise direction, the difference in deformation which is unbalanced with respect to the transverse dimension of the strip. In other words, the band of material corresponding to the over-thickness area prefers to be shorter than residual, being less rolled. However due to a kind of congruence, this event is being totally or at least partly balanced by the material itself. Although this sort of self correction seems a good thing for the process, it is not, because of its uncontrolled and undesirable nature. In addition, a sheet metal blank with a pre-existing thinning may be extremely dangerous for the stamping process.

In the wake of these preliminary simulations, several models were developed with different patch configurations and they are all discussed in the following paragraphs.

5.3 Finite Element Method analysis

All the geometries were modelled through Dassault Systemes SolidWorks or Catia due to the complexity of the three-dimensional solid. SolidWorks makes it possible to create parametric models in order to manage number, size and position of the "patch" entities by only acting on the editor commands and relations. Catia, moreover, gives the chance to develop particular geometries through the envelope of complex geometries on the base cylinder and then realizing the pocket relative to the strip patch. Assembly "Iges" files were then imported into MSC Marc as geometry input of the FE analysis as shown in Figure 5.4.

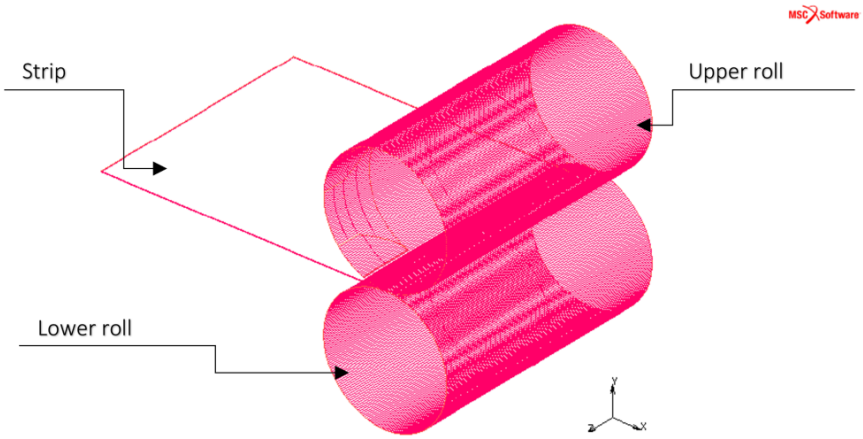

Figure 5.4 – 3D geometry of FE analysis

As reported in chapter 4, 5754 aluminium was chosen as material for the following analytical and experimental analyses. Even though several tests were led on 5754 specimens and many material flow plastic curves were available, a piecewise linear (strain hardening) material law as shown in Figure 5.5 was used in this case.

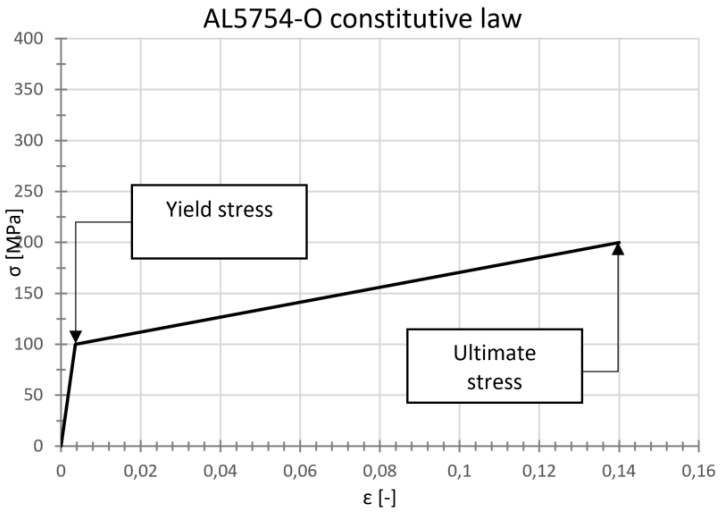

Figure 5.5 – AA5754 piecewise linear law

Subsequently upper and lower rolls and the sheet-metal plate were meshed by using different element types (Figure 5.6):

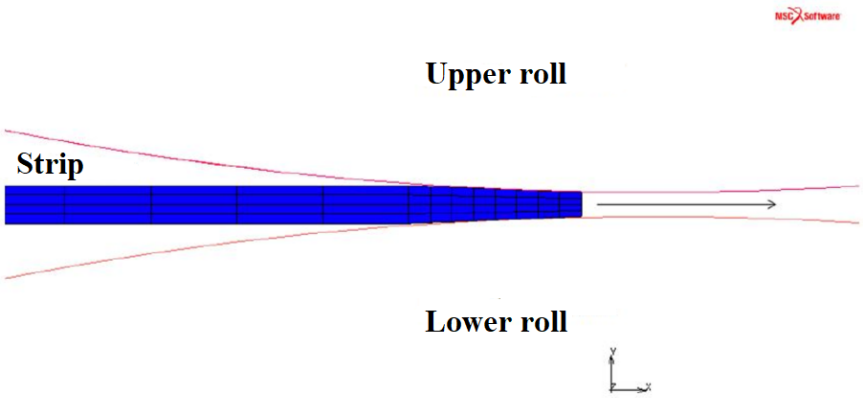

Figure 5.6 – Detail of the mesh in the thickness direction

- Default rigid elements were used to mesh upper and lower rolls, assuming them to be undeformable;
- Element type number 7 [**?**] has been used for aluminum plate.

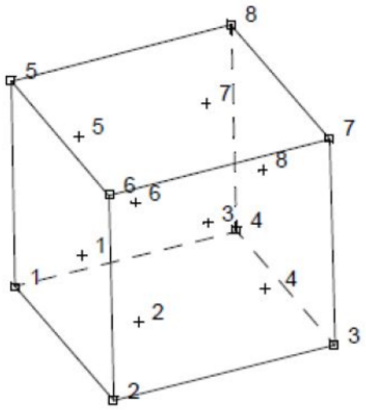

Figure 5.7 – Eight-node, isoparametric, arbitrary hexahedral n.7 element type

Deformable contacts between strip and rolls were set up in the program (Figure 5.8) paying particular attention to the friction coefficient in the roll bite, which is responsible of the realistic execution of the process. Friction and lubrication are important in the roll bite of cold rolling process as they influence the rolling forces and other rolling process parameters.

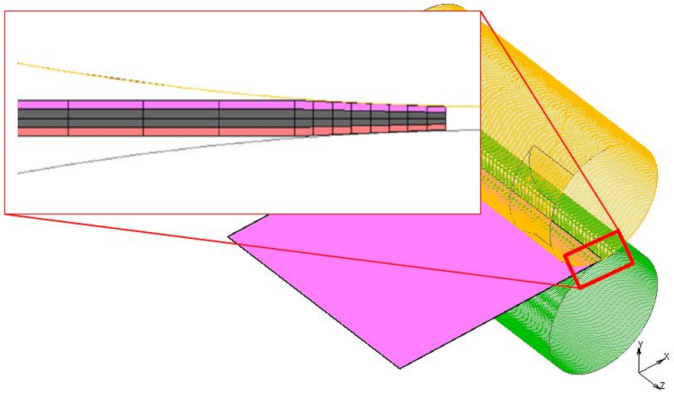

Figure 5.8 – Contact settings between upper and lower rolls and workpiece

In order to simulate the influence of pay-off and tension reels, nodal forces (Figure 5.9) were applied on front and rear workpiece surfaces as boundary conditions. Nodal forces were also removed at the end of the process in order

to simulate the spring back effect and evaluate the deformation of the workpiece due to the residual stresses.

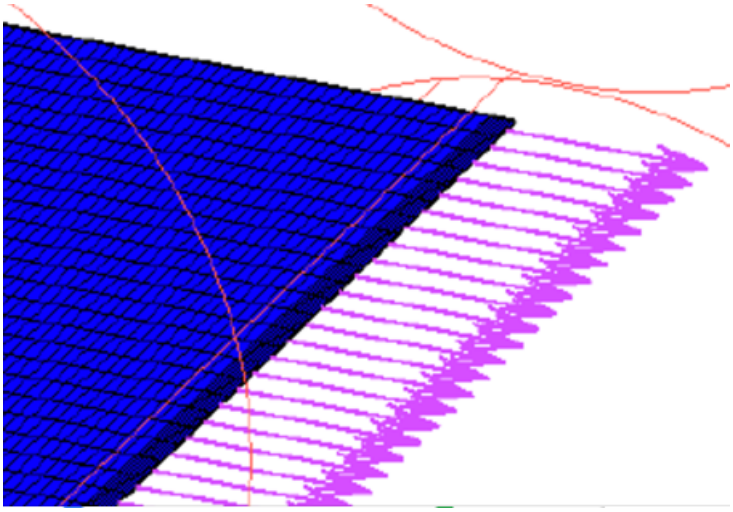

Figure 5.9 – Detail of the front surface boundary condition applied

Symmetry with respect to the width centreline of the work-piece was also set as a boundary condition, in order to significantly reduce the computational expense.

So all the following simulations, realised through SD SoWo, were led assuming a set of parameters to be constant and by varying size, number and shape of patches.

Constant geometrical characteristics of all the models are reported below:

workpiece length:	1200 mm;
workpiece width:	1500 mm;
rolls length:	1600 mm;
rolls diameter:	400 mm;
center to center distance:	401.4 mm;
initial thickness:	2.2 mm;
nomina rolled thickness:	1.4 mm;
overthickness value:	2 mm.

Other specifications will be described for each individual case.

5.3.1 Aluminum plate 1200x1500 with 3 patches

Patch rolling process with 3 patches on the finished product turns out to be of considerable interest. With reference to Figure 5.3, material appears to be deeply elongated due to the nominal high ratio of thickness reduction [1]

which is almost equal to 36% while in the over-thickness area is lower (almost equal to 9%) as is its elongation.

In order to avoid the formation of any kind of possible defect due to this sort of unbalanced condition, further over-thickness areas might help. Several patches were added to the previous geometry even though some bands were still stretched with the elongation value of 36% for the whole length of the strip.

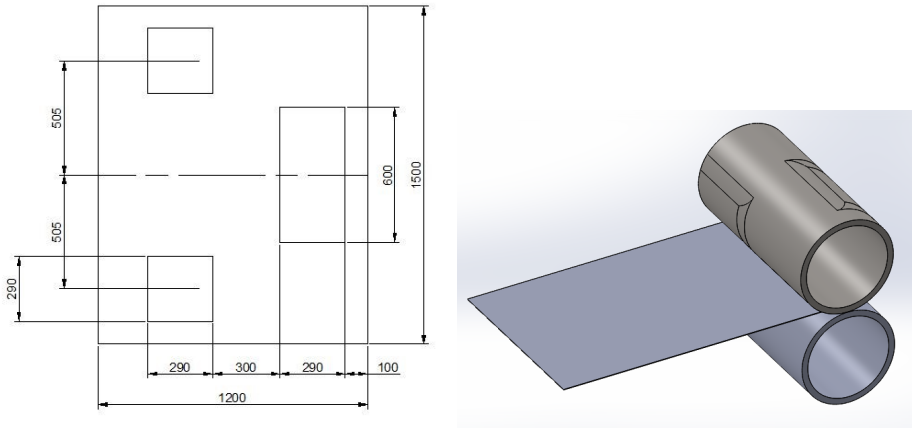

(a) Dimension drawing of 3 patches solution (b) CAD of 3 patches solution - symmetry BC

Figure 5.10

Figure 5.2 shows the contour bands distribution of lengthwise plastic strain component in the laminate product at the end of the load-case named "rolling" when pay-off and tension reels forces are still active. Looking at Figure 5.10b,

[1] Ratio of thickness reduction (r) is defined as the ratio of difference between final and initial thickness to the initial thickness:

$$r = \frac{\Delta H}{h_0} = \frac{h_0 - h_f}{h_0} \tag{5.1}$$

fillets generated on the edges of patches are clearly visible and they represent an attempt to dampen the difference of deformation which is unbalanced with respect to the transverse dimension of the strip. So from results in Figure 5.11 these fillets actually create some sort of a transition zone tending to stabilise the phenomenon but not completely erasing its effect.

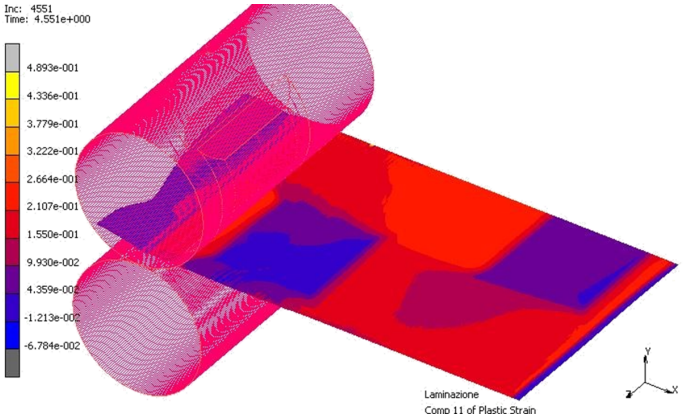

Figure 5.11 – Lengthwise component of plastic deformation

Two different paths were created on the surface of the laminated product (Figure 5.12a) in order to extrapolate numerical results, such as the displacement in x direction of all the nodes on the paths and plastic deformation as well. As shown in Figure 5.12b the presence of patches clearly influence the slope of the curves while the final total displacement remains almost the same.

Looking at the graph in Figure 5.13 equivalent plastic strain (Von Mises) was plotted on the ordinates while x-coordinate of the A path was plotted on the abscissa. Minimum value on the x-axis corresponds to the part of the strip still engaged in the roll bite whereas the maximum value is the part of material which were first rolled.

A peak of the equivalent strain within $600mm$ and $800mm$ is a clear indication of the influence of the over-thickness. Due to the presence of the patch, material that comes after appears to be more deformed than the nominal value. So it is clear that material tries to restore the congruence by itself, but does not entirely achieve it.

Another important aspect which has been investigated is the behaviour of

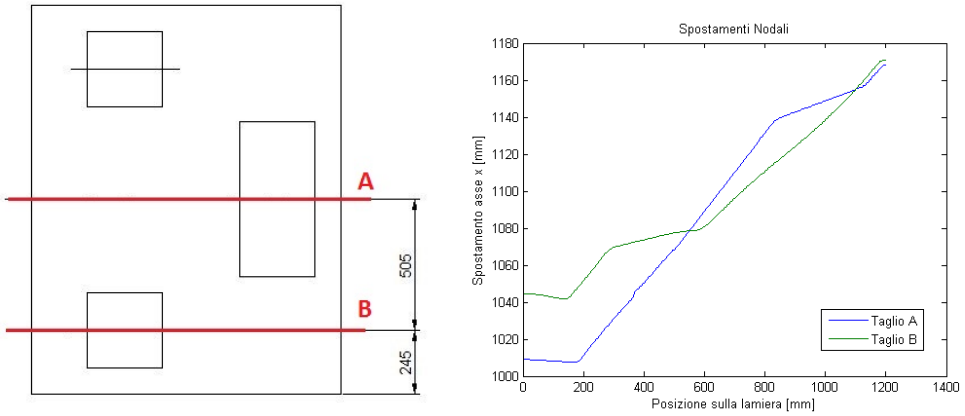

(a) Dimension drawing of 3 patches solution (b) CAD of 3 patches solution - symmetry BC

Figure 5.12

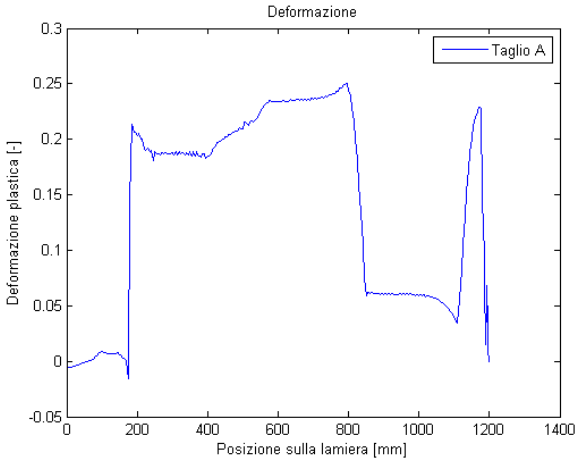

Figure 5.13 – Lengthwise component of plastic deformation at the end of rolling loadcase

the plate after the nodal forces have been removed. This load-case corresponds, in reality, to the cutting of a portion of metal sheet immediately after rolling. In this circumstance, the work-piece could severely deform, or even crumple up, due to an uneven distribution of residual stresses in the lengthwise direction. Compression forces, may cause the metal sheet to bend or even worse could make it possible for buckling phenomena to occur. So by removing the nodal forces of the FE model it is possible to predict how and how much the considered

work-piece will spring back.

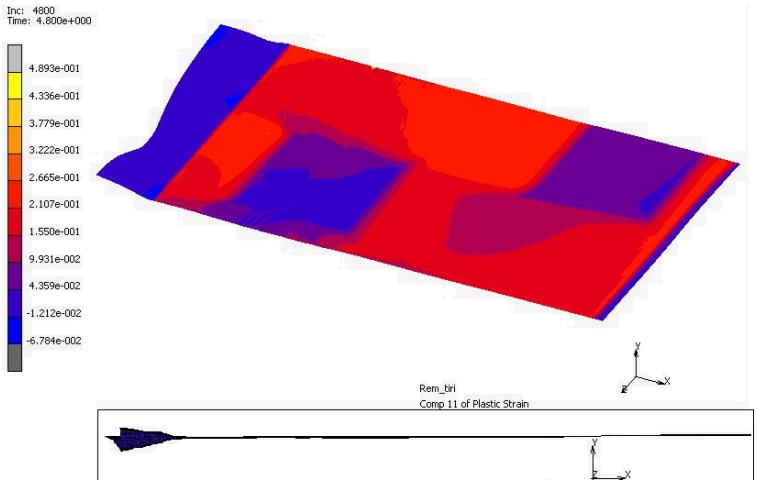

Figure 5.14 – Lengthwise component of ε_p and side view after forces removal

5.3.2 Aluminum plate 1200x1500 with 4 patches

The present FE model was developed with over-thickness areas smaller than the previous one. It also differs from the previous because of the absence of the central patch, as shown in Figure 5.15a, hence being more unbalanced than the configuration described above. So looking at Figure 5.15a and Figure 5.15b only two patches are visible due to the symmetry boundary condition.

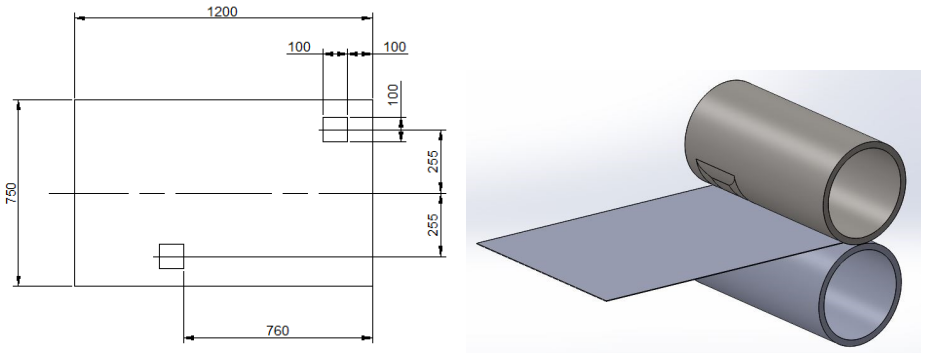

(a) Dimension drawing of 4 patches solution (b) CAD of 4 patches solution - symmetry BC

Figure 5.15

As in the previous case, the FE model highlights the formation of tinning areas immediately after the patches. Due to the smaller dimensions in length and width of the patch, the tinning effect appears to be softer with a deformation value similar to the nominal one.

A more significant result is represented by the deformation of the work-piece after the nodal forces have been removed. Looking at Figure 5.16 the spring back effect appears to be more evident than in the previous case. A possible reason of this phenomenon can be researched into the value of the ratio of the total transversal size of the patches to the strip width. Looking at the dimension drawings in Figure 5.10a and Figure 5.15a it can easily be calculated that the former is almost equal to 0.79 while the latter is only equal to 0.27.

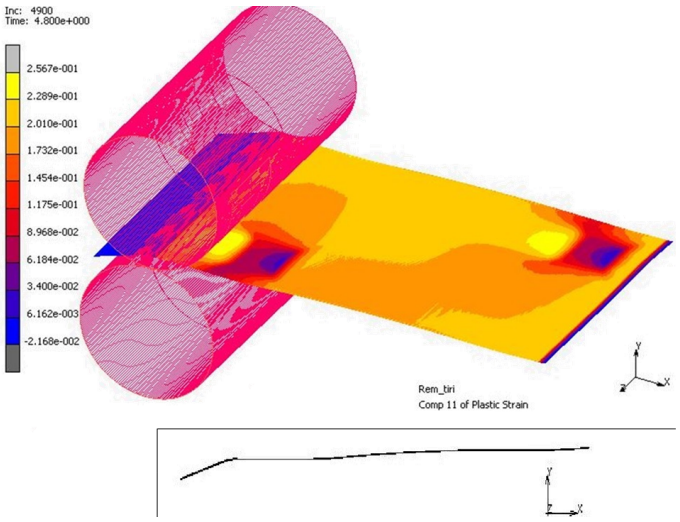

Figure 5.16 – Lengthwise component of ε_p of 2 patches model

5.3.3 Aluminum plate 1200x1500 with 6 repeated patches

This model was developed to investigate the behaviour of the material with several patches all centred along the same lengthwise axis, as shown in Figure 5.17a. Symmetry boundary condition was considered in this case also.

As in the previous two cases, FE model highlights the formation of tinning areas immediately after all of the patches. But in this case, it is worth noting

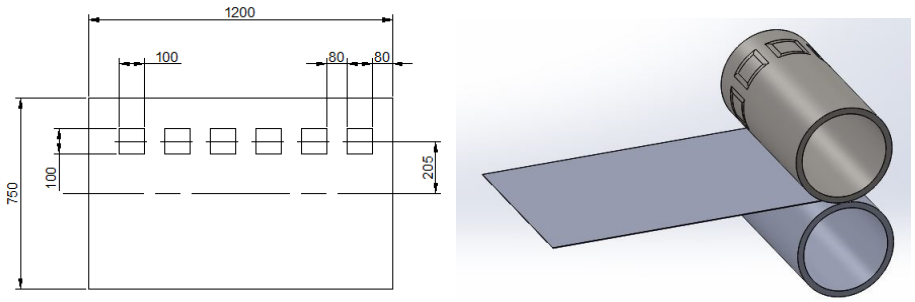

(a) Dimension drawing of 6 patches solution (b) CAD of 6 patches solution - symmetry BC

Figure 5.17

that this phenomenon tends to amplify after each patch as shown in Figure 5.18.

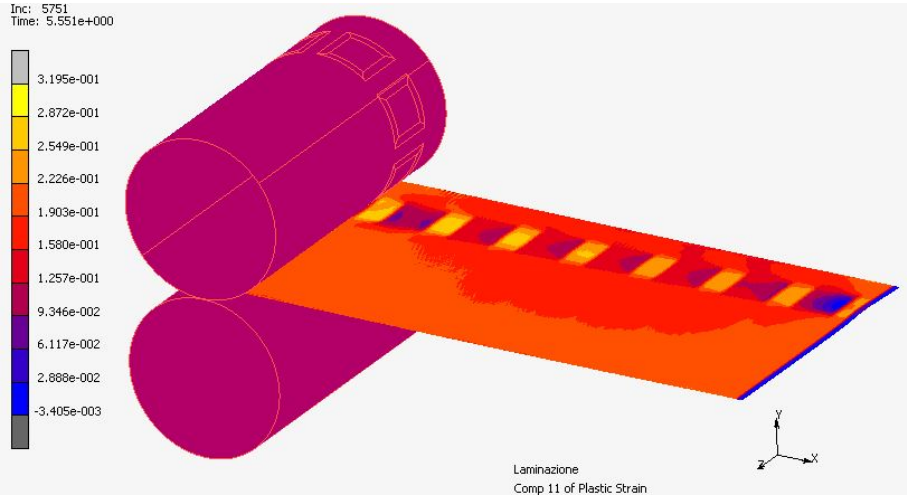

Figure 5.18 – Lengthwise component of ε_p of 6 patches model

5.3.4 Aluminum plate 1200x1500 with full width patch

This model is not so far away from the bi-dimensional simulation. The main difference is that in the 2D case the thickness variation was obtained by moving the upper roll up and down. In this case, however, the pocket was realised on the upper cylinder only. The aim of this simulation was to investigate the profile-rolling process, in order to evaluate if the finished product presents a thickness variation which is symmetrical to the middle line of thickness. So

only one pocket with constant length was realised, parallel to the cylinder's longitudinal axis and for the full width of it.

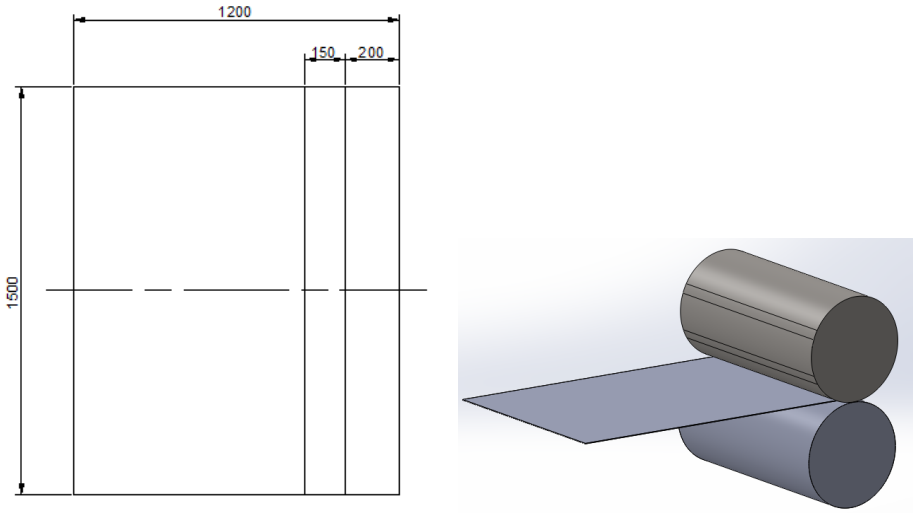

(a) Dimension drawing of profile rolling (b) CAD of profile rolling - symmetry BC

Figure 5.19

Unsurprisingly, there are no zones with which the material tries to restore the congruence because it is already fully balanced everywhere in the work-piece (Figure 5.20). Furthermore, the overthickness appears to be modelled upward only, demonstrating that there is no symmetry with respect to the thickness midline.

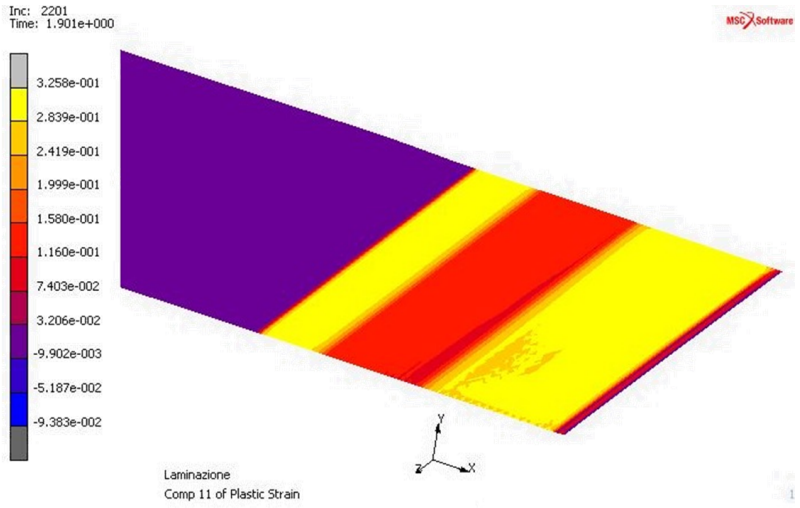

Figure 5.20 – Lengthwise component of ε_p of profile rolling

5.3.5 Aluminum plate 1200x1500 with arch patch

This over-thickness distribution is quite similar to the previous one. Like the model described above, the ratio in term of the total transversal size of the patch to the strip width, is equal to 1. Length of the patch is constant as well and its axis is not parallel to the cylinder's axis but it is an envelope onto the cylinders's surface of an arch centred downstream of the roll bite.

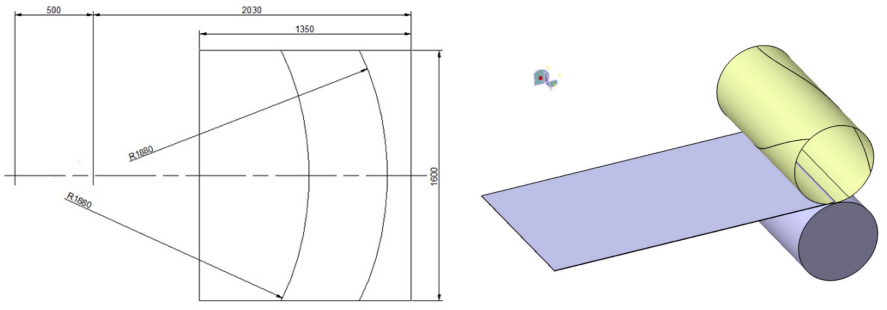

(a) Dimension drawing of arch patch solution (b) CAD of arch patch solution - symmetry BC

Figure 5.21

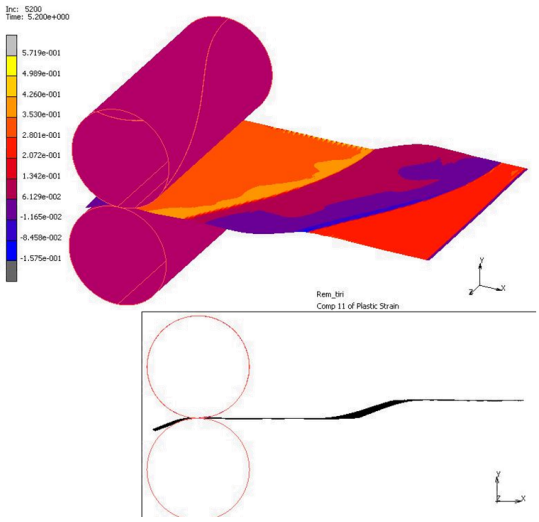

Figure 5.22 – Lengthwise component of ε_p of profile rolling with arch

Figure 5.22 shows the strain distribution over the finished work-piece. It should be noted that strain values on the over-thickness area are greater where the material has been rolled first. This means that material (in the symmetry region, where the patch comes first) is undergoing some sort of local stretch because it is trying to restore the congruence by itself, not knowing what will happen next to the nearby material bands.

As shown at the bottom in Figure 5.22, finished work-piece seems to be severely deformed after the removal of the forces. This phenomenon can be related to the process asymmetry which generates a kind of calendering effect.

5.4 Balance of the lengthwise deformation

In the light of the above results, the question of balancing the lengthwise deformation arises, since more than just one over-thickness area can be requested. Cold rolling process requires the sheet metal to present the same value of thickness reduction throughout the all width of the plate after a full round of cylinders, as well as its length variation. If not, bending or even tearing of the sheet metal can occur after additional rounds through the mill.

Macroscopically, this phenomenon can be explained through a discretisation

of the blank in n beam elements which would all show the same elongation value after the deformation in the rolling direction. If this is not done, the sheet metal plate will be unbalanced (Figure 5.23) and material will tend to restore the congruence by itself. As a consequence, residual stress states will occur: positive stress states (traction) in bands of material relative to the over-thickness area and negative stress states (compression) elsewhere. Every additional round of the cylinders will amplify this unbalanced state until a critical condition is achieved: local buckling phenomena (e.g. edge buckling or center buckling) due to the compressive residual stress or break of the plate because of propagation of micro-cracks due to the tensile residual stress.

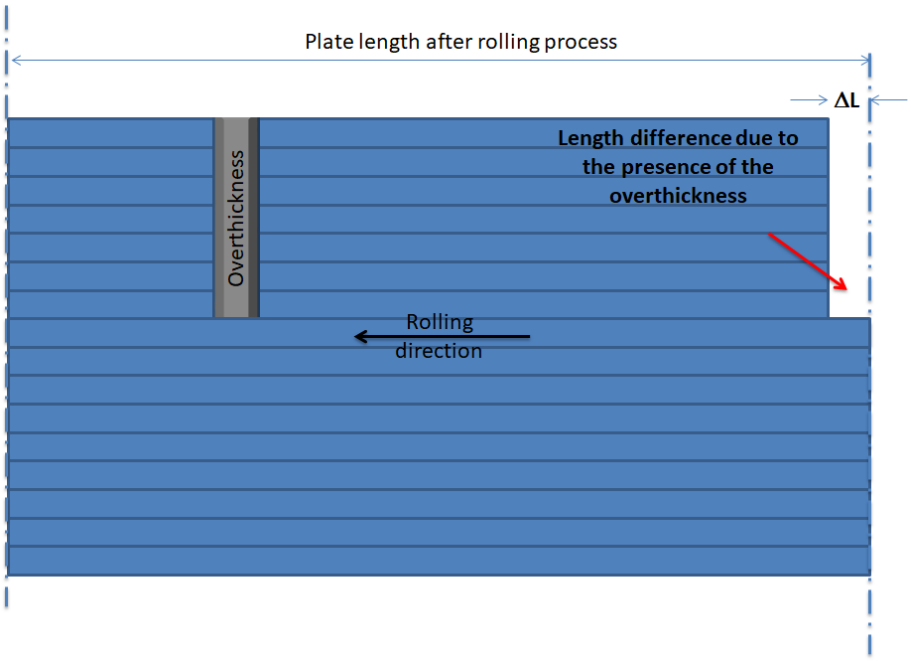

Figure 5.23 – Discretization of a plate with overthickness

These considerations were further confirmed by developing an analytical model in MATLAB ®able to evaluate the degree of imbalance of the considered work-piece.

Through data entry, such as:

- length of the workpiece [mm];

- width of the workpiece [mm];
- number of patches;
- center coordinates of the patches;
- fillet radius betwen different thickness zones;
- initial thickness of the strip;
- overthickness value;
- nominal thickness value;

the program starts returning the strain distribution preview of the desired work-piece (Figure 5.24a) and its 3D thickness appearance (Figure 5.24b).

So after a discretisation of the selected geometry into small elements, thereby defining a very fine mesh, the program calculates how the undeformed work-piece should look before being rolled (Figure 5.24c).

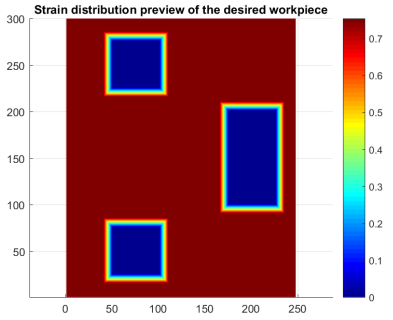

(a) Strain distribution preview

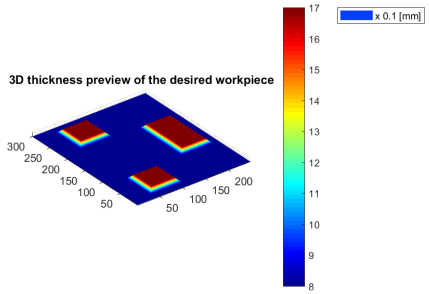

(b) 3D thickness preview

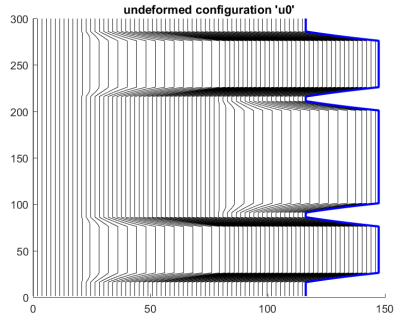

(c) Undeformed configuration

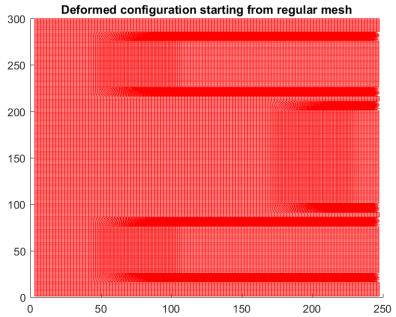

(d) Deformed configuration

Figure 5.24

In a similar way, Figure 5.24d shows how a regular, square starting-mesh appears after being patch-rolled, suggesting the process creates very different deformation states between the involved elements on the patches and those elsewhere.

The same considerations can be made for the other cases as described in paragraphs 5.3.2, 5.3.3 and 5.3.4. Running the program, the state of imbalance of the considered case can be evaluated and thus a preview of the deformed configuration and shear deformation state is reported below.

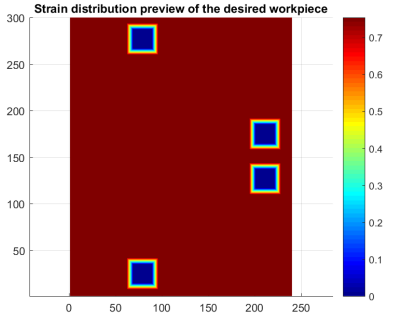

(a) Strain distribution preview

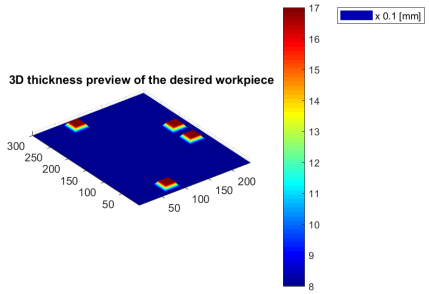

(b) 3D thickness preview

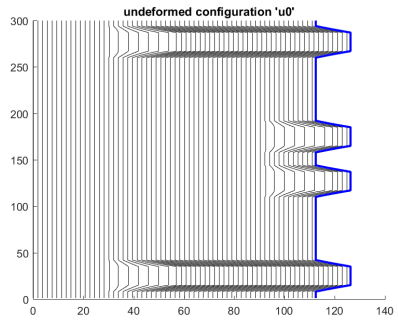

(c) Undeformed configuration

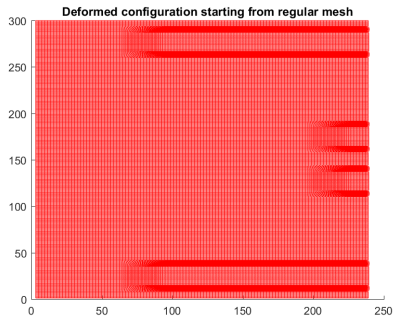

(d) Deformed configuration

Figure 5.25

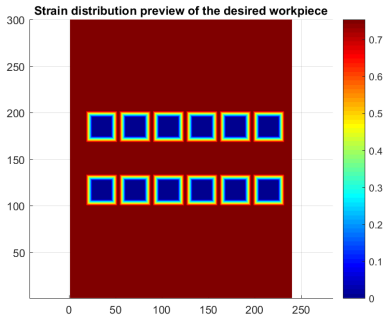

(a) Strain distribution preview

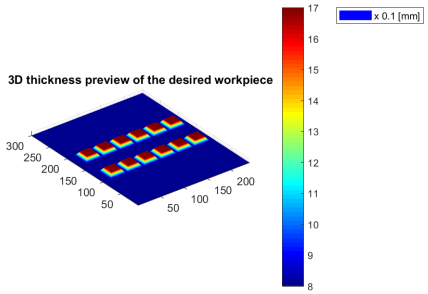

(b) 3D thickness preview

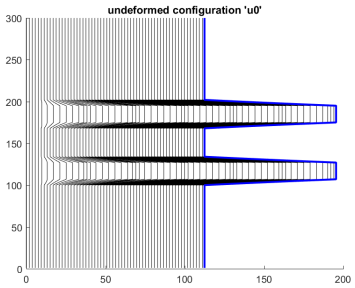

(c) Undeformed configuration

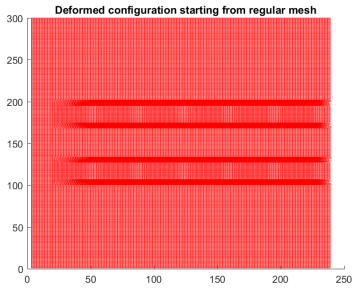

(d) Deformed configuration

Figure 5.26

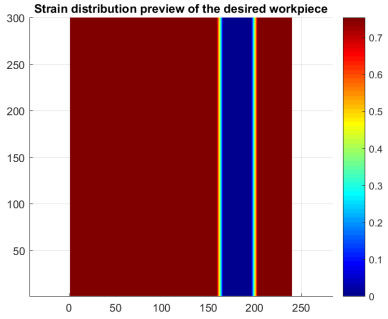

(a) Strain distribution preview

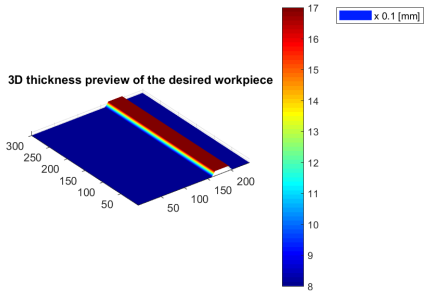

(b) 3D thickness preview

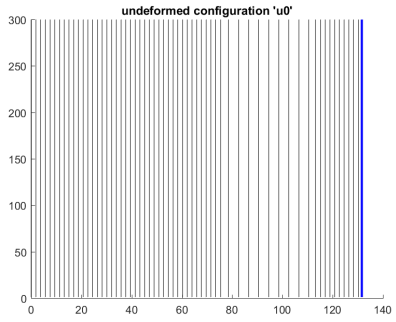

(c) Undeformed configuration

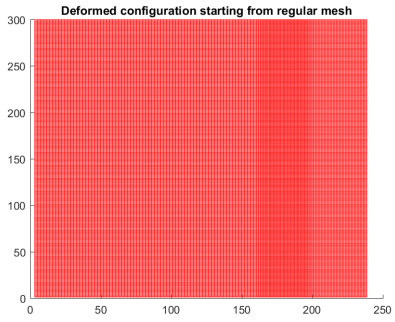

(d) Deformed configuration

Figure 5.27

5.5 Hypothetical real case application

So considering a real case like the one shown in Figure 5.28, plenty of solutions can be considered but from the discussion above the main condition to respect is a complete balance of the deformation.

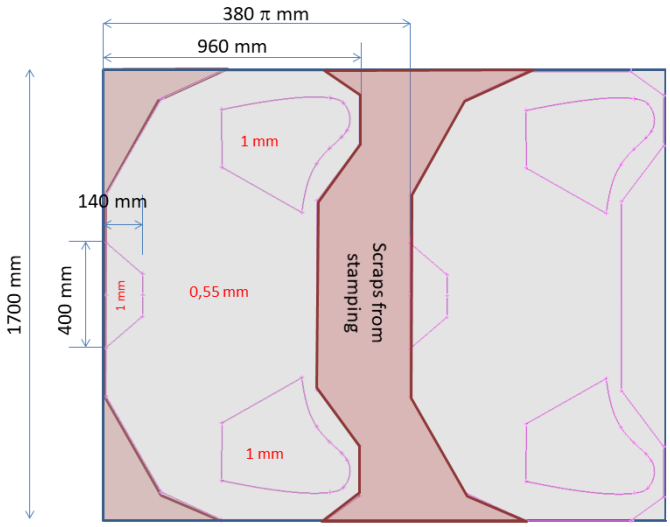

Figure 5.28 – Real application case of patch-rolling process

After the length value of the ideal full-balanced patch is defined (Figure 5.29),

a more complex geometry of the rolled product can be defined. Patches can be distributed along the rolled geometry, assuming the balance to be already guaranteed. In this case a configuration like the one shown in Figure 5.30 is the one which best fit the customer's needs.

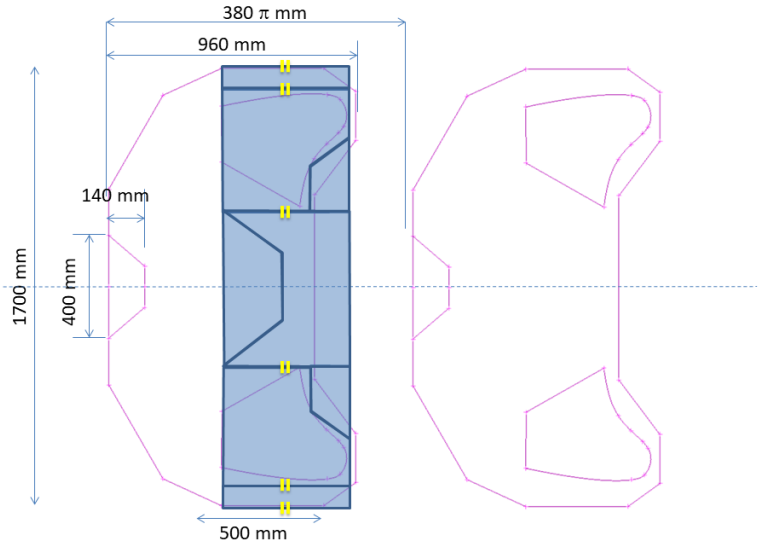

Figure 5.29 – Ideal full-balanced patch

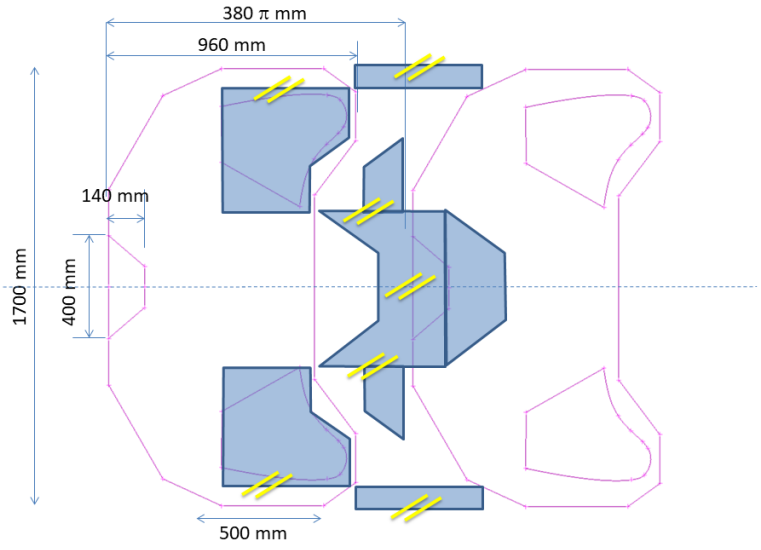

Figure 5.30 – Full-balanced patches distribution

Even though a 100% balance is obtained, a F.E.M. model is still necessary to analyse how the strip will behave. Complex configurations require complex CAD geometries. To this purpose, DS Catia was very helpful due to a particular function which allowed a complex sketch (Figure 5.31) on the base cylinder to be enveloped and thus establish the pocket to which the patches relate.

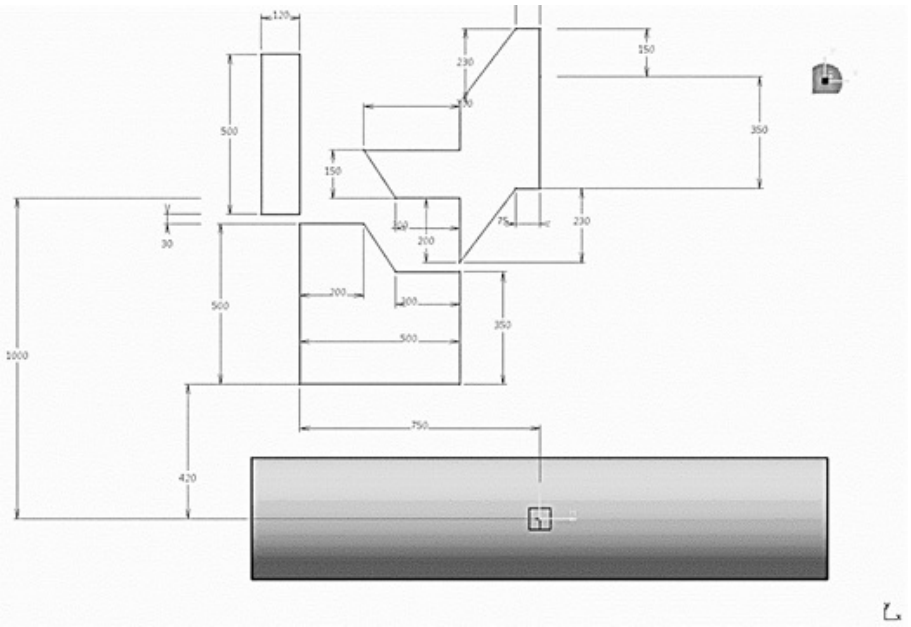

Figure 5.31 – Particular of the sketch enveloped on the cylinder

Figure 5.32 shows the surface contour bands of the lengthwise component of plastic strain in the work-piece at the end of the rolling process. The transition zones were not sufficient to guarantee a soft distribution of the deformation in proximity of the over-thicknesses.

Despite the complete balance a remarkable edge buckling phenomenon occurred and it is clearly visible on the far side of the strip near the main patch. However, this phenomenon might be only related to the fact that the main patch was not yet balanced and that it was too close to the free edge of the strip. To overcome this issue, a model with 2 or more rotations of the cylinder might be run.

As in the previous cases, reel forces were removed and the strip behaviour

was observed. In this case, after the forces were removed, the only part of the finished work-piece which appears to be lightly bent is the part that enters first into the roll bite.

All these results demonstrated a good efficiency of the balanced model.

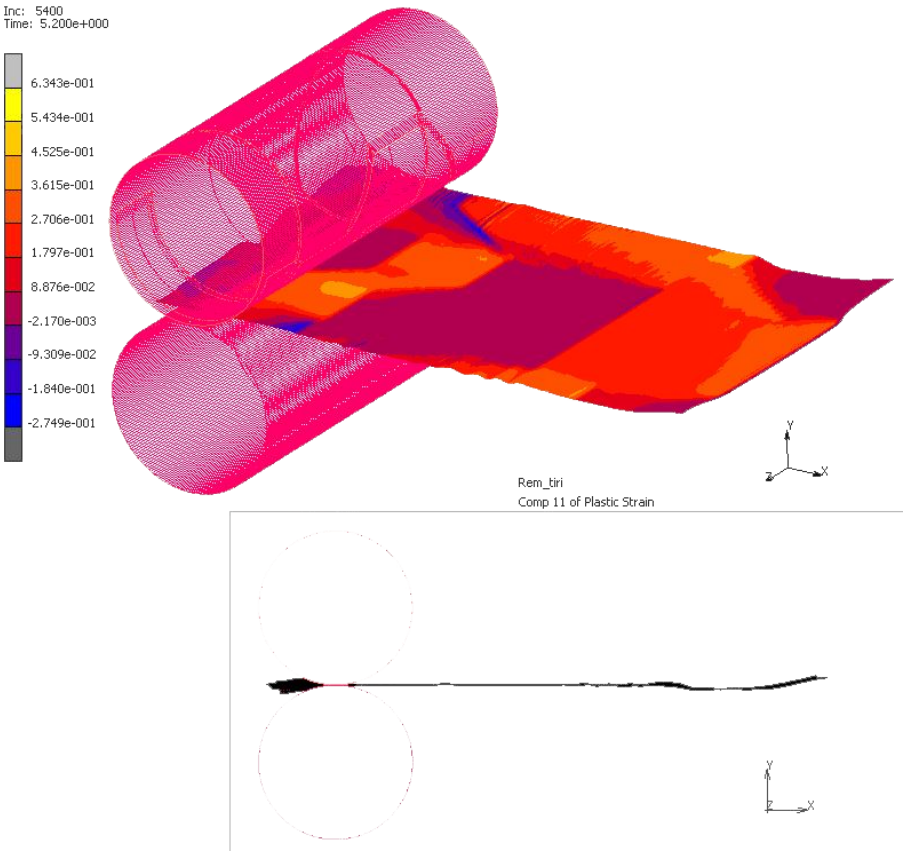

Figure 5.32 – Lengthwise component of ε_p of real application case profile rolling

Chapter 6

Design Of Experiments and analysis of the results

Chapter 5.3 showed a qualitative response of the material to different shapes and sizes of patches. Chapter 5.4, therefore, demonstrated the importance of a complete balance of patch distribution on the surface of the desired workpiece, in order to guarantee continuous production. Together, these chapters gave a rough indication of the feasibility of the process and also identify its limits and possible defects. Overall, several cases have been investigated and each one was very different from the rest. However, in a production scenario, the client's request might be very customized according to his specific needs, so these few models are not sufficient in providing a global predictive description of this innovating rolling process.

In order to avoid the necessity of specific simulations for every client's request, the possibility to identify some safe ranges of all the parameters involved in the patch rolling process could achieve a cost reduction and better quality of the product.

6.1 Identification of the process parameters

Feasibility of the process is strictly related to numerous process variables, each one having a different importance. A lot of parameters were identified to be involved in the process, but in hypothesizing a real case application

(Figure 6.1) some of them must be defined as constant whereas the others have to vary in order to identify the limits of the process.

In the following case, an automotive application is investigated. The work-piece of the size of $1250mm \times 1500mm$ and finished thickness of $1.4mm$ is rolled with 3 total patches with a thickness of $2.1mm$. The initial thickness value is equal to $2.2mm$. The size of the principal patch, that the door hinge will be welded onto, is $400mm \times 240mm$, with a transition zone of $35mm$ length. The other two patches, the length of which is equal to the remaining transversal size, were modelled to guarantee the complete balancing of the lengthwise deformation.

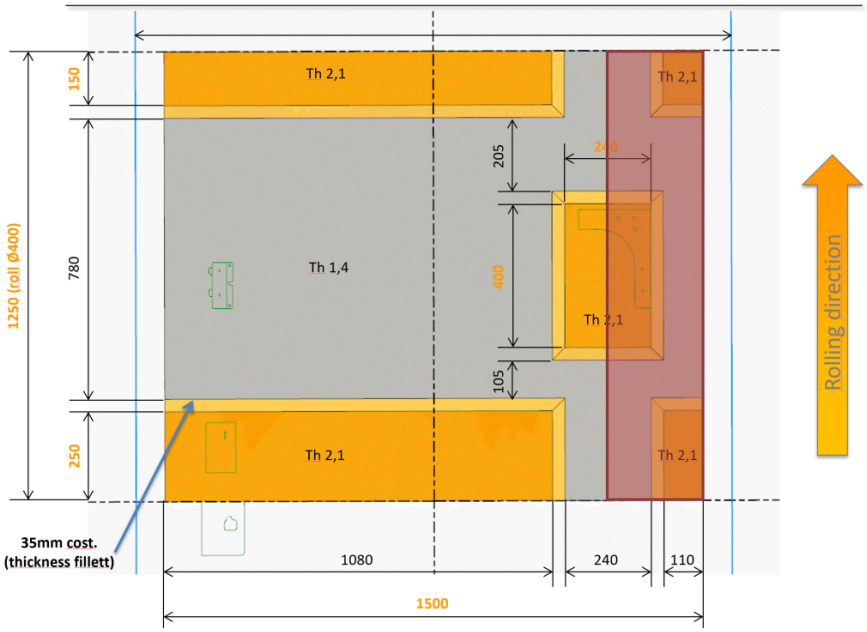

Figure 6.1 – Real case application example of the patch rolling process

In order to evaluate different study cases, by iteratively changing the value of some of the involved parameters, and in order to make the computational analysis lighter and therefore to take less than ten days, only a small portion of the whole work-piece will be analysed.

So considering the red highlighted zone only, the involved parameters can be divided as follows:

Constant parameters:

- ϕ_{rolls} - rolls diameter ;
- Δt_{patch} - patch depth ;
- Δt_{total} - nominal reduction ;
- H - work-piece width ;
- $h_2 = H - h_1 - r$ - 2nd patch width ;

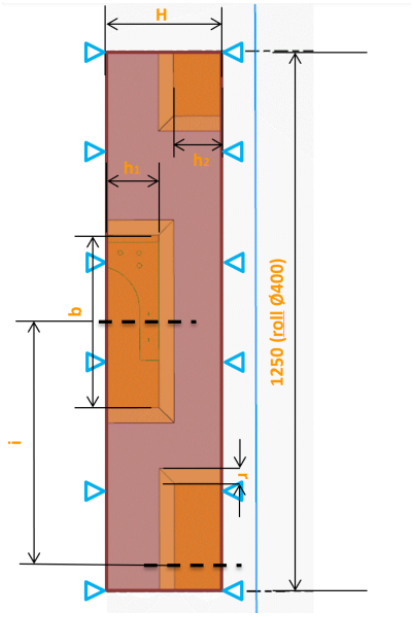

DoE parameters:

- t_0 - initial thickness ;
- b - 1st patch length ;
- h_1 - 1st patch width ;
- r - fillet radius ;
- i - centre to centre distance ;

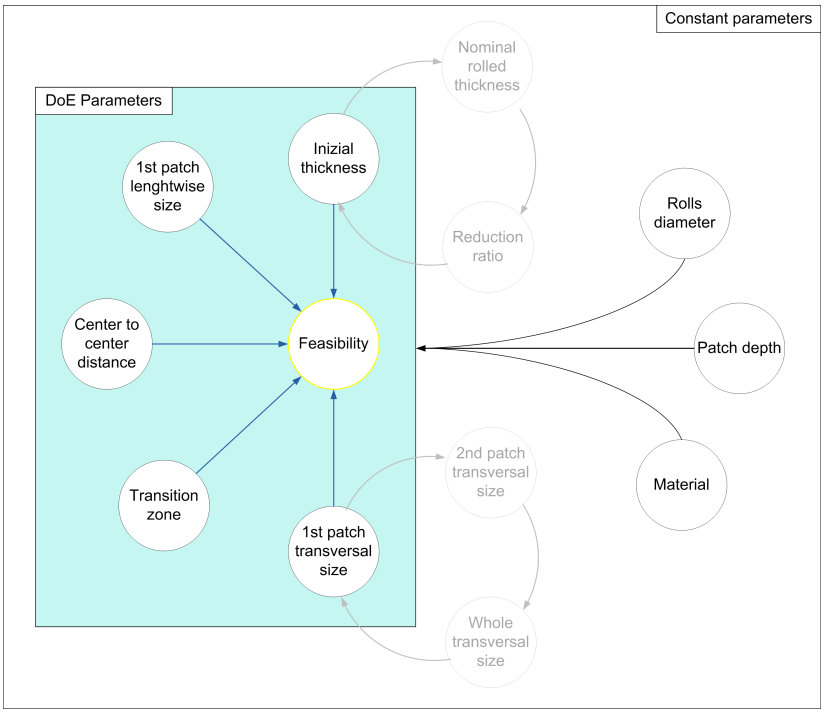

Figure 6.2 – Graph of all the process variables

The study of how these factors (main variables) can affect the feasibility of the process was performed through a FEM experimentation organized ac-

cording to the Design of Experiments (DoE) techniques. The adoption of this methodology was motivated by the need to reduce the number of tests without preventing a good estimation of the influence that individual factors may have and of their possible interaction.

6.2 A brief reference to the Design Of Experiments

The Design of Experiments [35, 36] or experimental design, is a widely used method for statistically quantifying the measures taken on the factors and on their interactions by observing the forced changes made in logical order and directed by mathematically obtained tables.

Designing an experiment means performing a series of tests where the input variables vary in a programmed way to identify the reasons why the result in question has changed. Generally, the most intuitive experimental scheme consists of performing one or more tests for each value, or level, of the independent selected variable, keeping any other conditions constant. In order to evaluate the effects of other parameters, the procedure is repeated for each one. This *mono-varied* procedure, however, presents the disadvantage that the effect of each parameter is evaluated for one and only one particular combination of the levels of the other parameters. In other words, the estimate of the interactions between the various parameters is omitted, omitting to study the effects of simultaneous variations of two or more parameters. The DoE, on the other hand, is based on a *multi-variated* approach, as the tests present the simultaneous variation of more than one parameter. Once the number of levels for each variable is fixed, the maximum information is obtained through a complete factorial plan, which provides for tests that correspond to all the possible combinations of levels. This way it is possible to get a regression model that contains all the terms of interaction between the parameters at stake.

When the number of involved parameters is large, the use of complete factorial plans requires an increase in the number of tests needed in geometric progression as the parameters heighten. On the other hand, since in many cases it is not necessary to resort to models containing all the terms of interac-

tion between the parameters, since generally the higher order interactions are of decreasing entity, fractional factor plans can be used. By exploiting a priori knowledge of the experimental context in which they work, they can estimate the not-so-negligible parameters of the model without resorting to exhaustive comprehensive plans.

So the steps needed to make a DoE, after the problem has been defined, are summarized in the following:

1. choosing variables definition intervals and possible sampling levels;
2. defining the response variable;
3. choosing the appropriate DoE;
4. performing the experiments;
5. analysing the data;
6. validating results.

Choosing the number of levels per variable is essentially related to the linearity of the effects: choosing a 2-level sampling presupposes that the response is x-linked linearly. If the variable definition interval is very extensive, the x-y link analysis will be less and less correct as you move away from the linear trend hypothesis. The crucial role of point 1 in the development of tests is therefore clear. To overcome these inconveniences, two different methods can be utilised: the first one requires the choice of three or more levels of sampling and is recommended only in the case of wide intervals and highly non-linear problems, taking into account that it requires a high number of tests; the other one proposes the choice of planes on two levels to be expanded through additional intermediate point tests to estimate the curvature of the relationship in the studio.

In order to reliably process the data obtained from an experimental test, it is important to know their quality or in other words to identify the possible causes of uncontrolled variability that can produce dirty results. These causes can be intrinsic to the phenomenon (internal and external noise), or related to the data acquisition process (measurement errors). Their estimation is necessary to avoid confusing noise with the effects of treatments. To distinguish exper-

imental phenomena independently from the sources of noise, it is advisable to follow three basic rules: *replicate*, *randomize* the order of tests and *realize* them after a subdivision into blocks. The first one allows the evaluation of the dispersion of response data, the second helps in reducing system errors, and the third allows the results at the end of each testing session to be processed.

6.3 Implementation of a Design of Experiments

For the considered Design of Experiments, three sampling levels were defined, in order to evaluate the non-linearity of the chosen parameters, which are five in total: initial thickness of the strip, lengthwise size of the central patch, transversal size of the central patch, lengthwise and transversal size of the transition zone between the different thickness areas, centre to centre distance between the central patch and the recovery one.

Table 6.1 – Definition of DoE (variables)

Variables		Min [mm]	Max [mm]
Thickness	t_0	1.7	2.7
1st patch width	b	50	200
1st patch length	h_1	60	200
Transition size	r	35	70
Centre to centre	i	200	500
Rolls diameter	ϕ_{rolls}	400	
Patch depth	Δt_{patch}	0.7	
Nominal reduction	Δt_{total}	0.9	
Work-piece width	H	450	
2nd patch width	h_2	$H - h_1 - r$	

The complete design of experiment, thus defined, provides 243 different sim-

ulations (3^5). This number clearly appears to be too elevated for an implicit F.E.M. model that, due to its complexity, requires almost $3-4$ days to be completed. Wanting to run them all, it would take more than 2 years of simulations.

To avoid this drawback, it was necessary to develop a simplified DoE, in other words a Design of Experiments with a lower number of simulations.

Table 6.2 – Definition of DoE (levels)

	Levels [mm]		
	-1	0	1
t_0	1.7	2.2	2.7
b	50	100	200
h_1	60	130	200
r	35	50	70
i	200	350	500

Table 6.3 – Adopted DoE

Run	t_0	b	h_1	r	i
1	*0*	*0*	*0*	*0*	*0*
2	*-1*	*0*	*0*	*0*	*0*
3	*1*	*0*	*0*	*0*	*0*
4	*0*	*-1*	*0*	*0*	*0*
5	*0*	*1*	*0*	*0*	*0*
6	*0*	*0*	*-1*	*0*	*0*
7	*0*	*0*	*1*	*0*	*0*
8	*0*	*0*	*0*	*-1*	*0*
9	*0*	*0*	*0*	*1*	*0*
10	*0*	*0*	*0*	*0*	*-1*
11	*0*	*0*	*0*	*0*	*1*

Table 6.2 shows the effective values which correspond to each level of the investigated variable; the whole DoE and the levels of each FEM simulation are reported in Table 6.3.

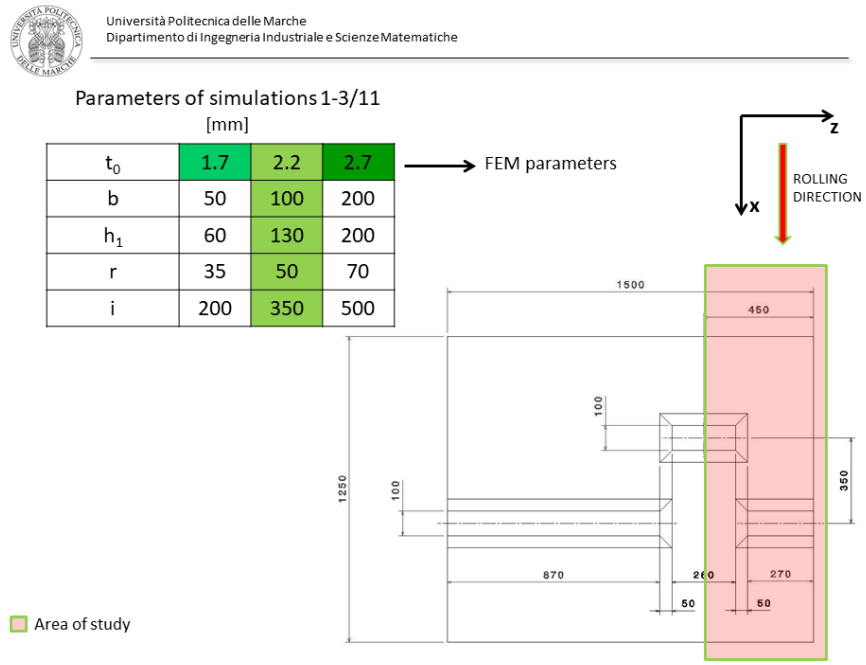

Figure 6.3 – First three analyses settings

The first analysis was performed with the intermediate level of all five parameters; the others, meanwhile, were performed by making one of the five parameters assume iteratively one of the extreme values of its level, while keeping the other four at the middle level, for a total of 10 simulations. In conclusion 11 simulations were carried out (Figure 6.3 , 6.4a, 6.4b, 6.4c, 6.4d, 6.4e, 6.4f, 6.4g, 6.4h), certainly a more feasible number, which also provided a thorough analysis of the results predicting also the quality of the finished laminate, by interpolating data with a combination of parameters which have not been analysed directly.

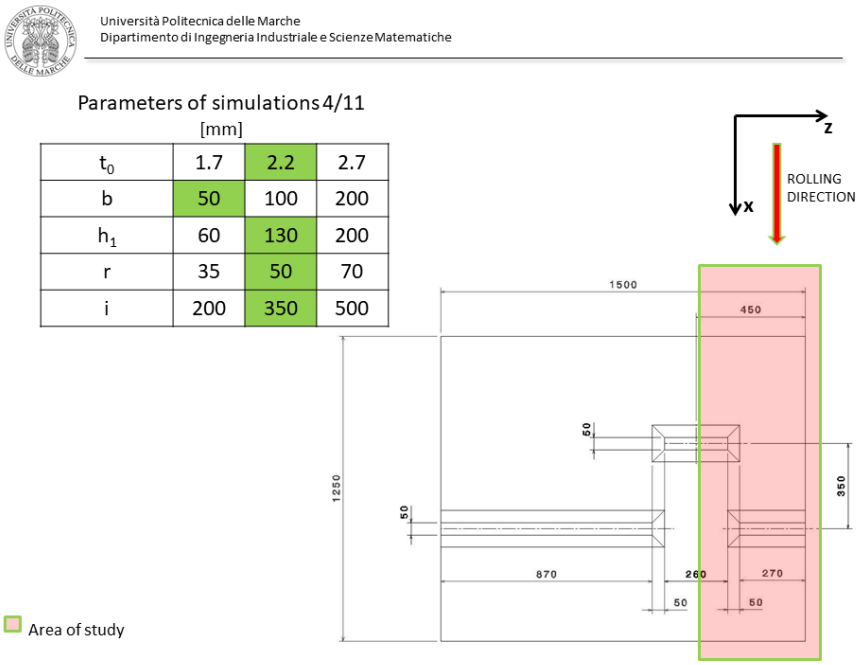

t_0	1.7	2.2	2.7
b	50	100	200
h_1	60	130	200
r	35	50	70
i	200	350	500

(a) Fourth analysis settings

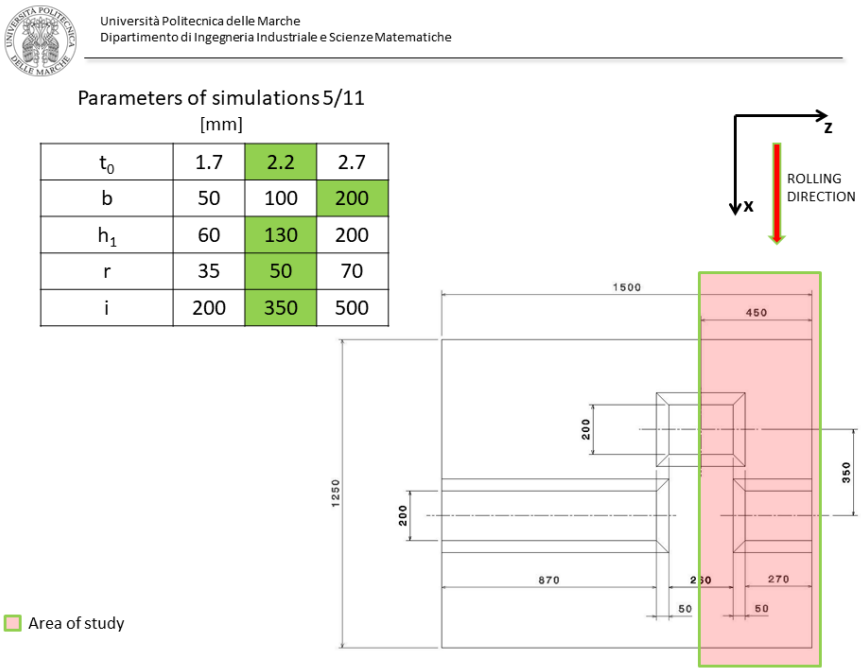

t_0	1.7	2.2	2.7
b	50	100	200
h_1	60	130	200
r	35	50	70
i	200	350	500

(b) Fifth analysis settings

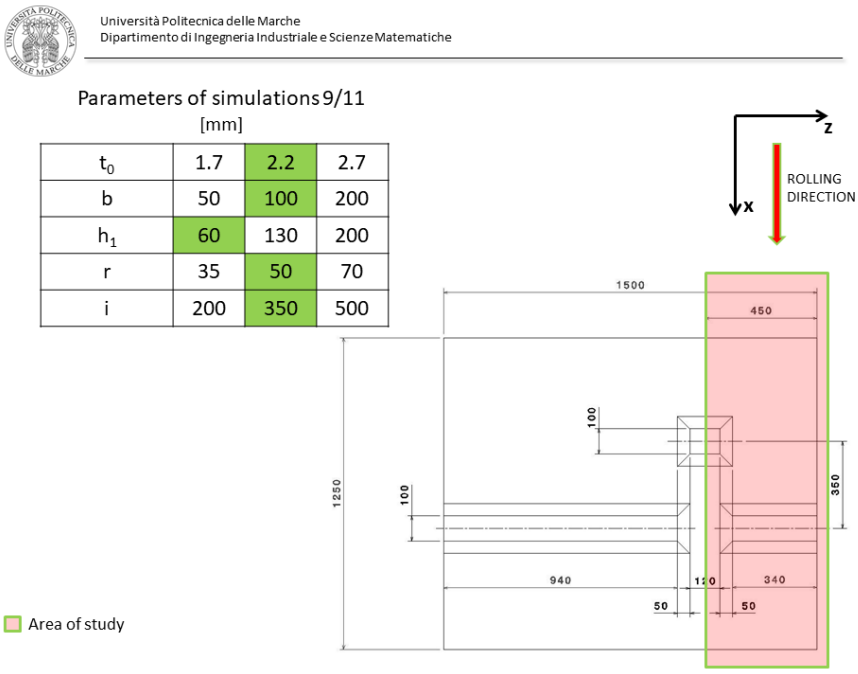

(c) Sixth analysis settings

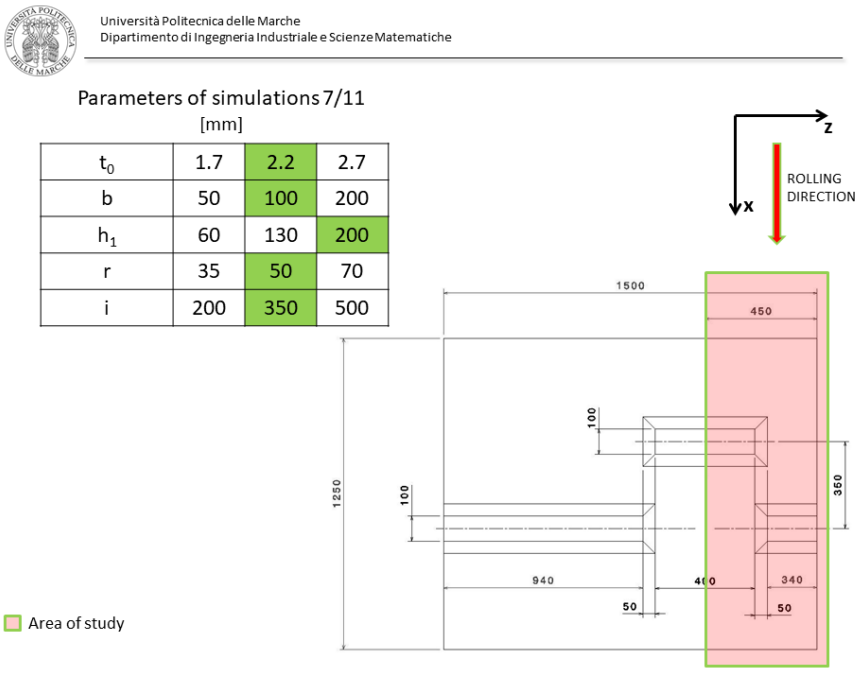

(d) Seventh analysis settings

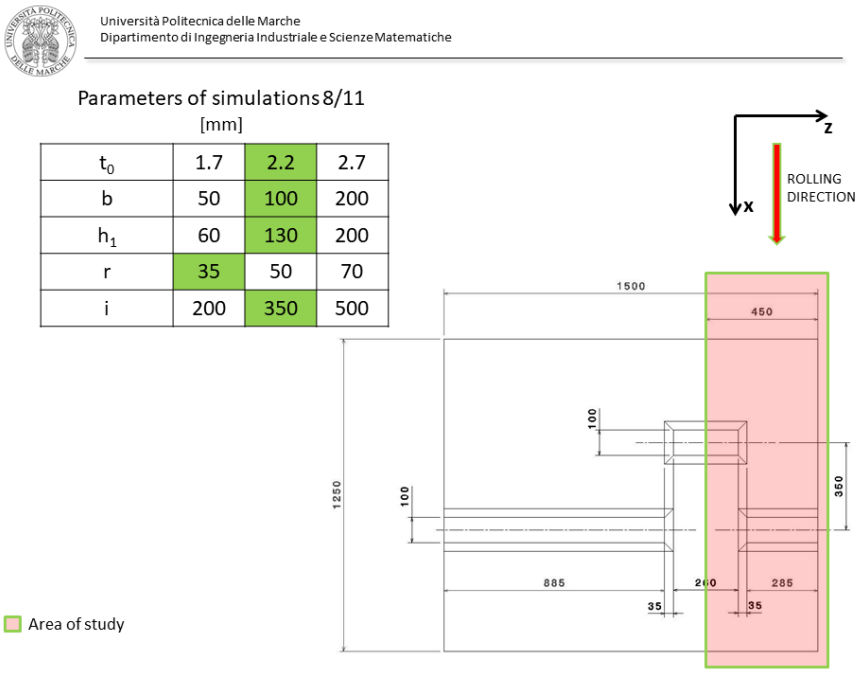

(e) Eigth analysis settings

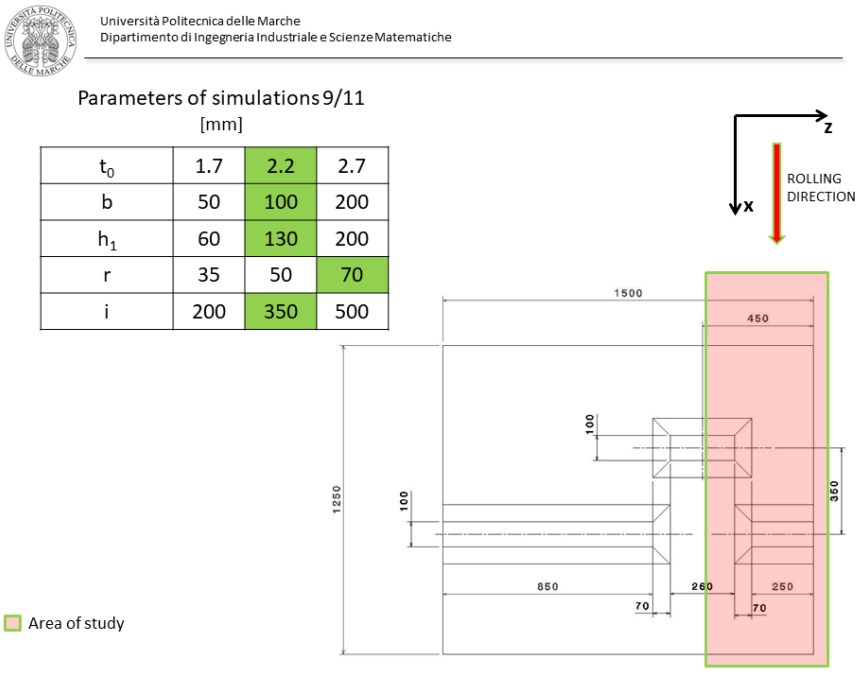

(f) Ninth analysis settings

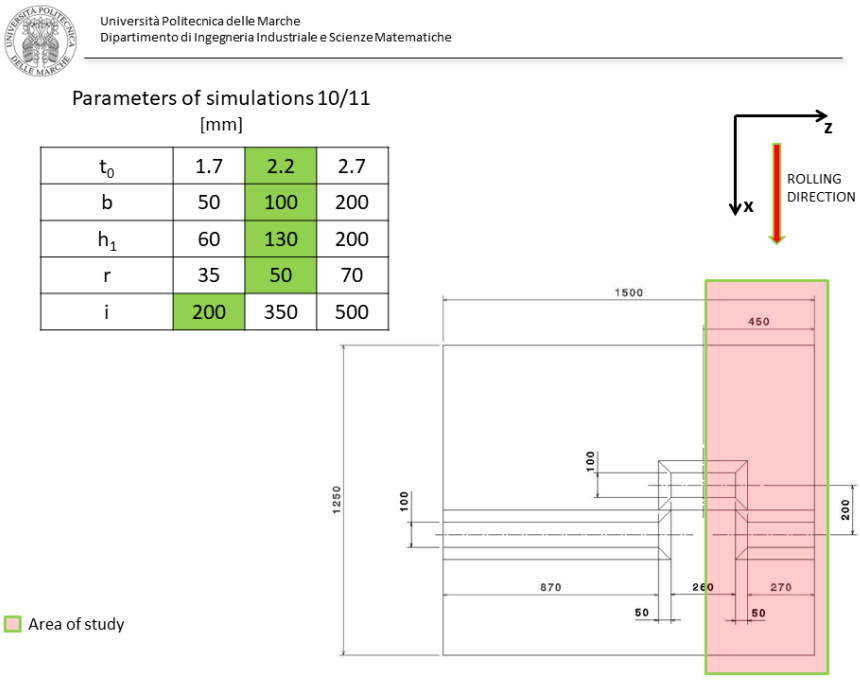

(g) Tenth analysis settings

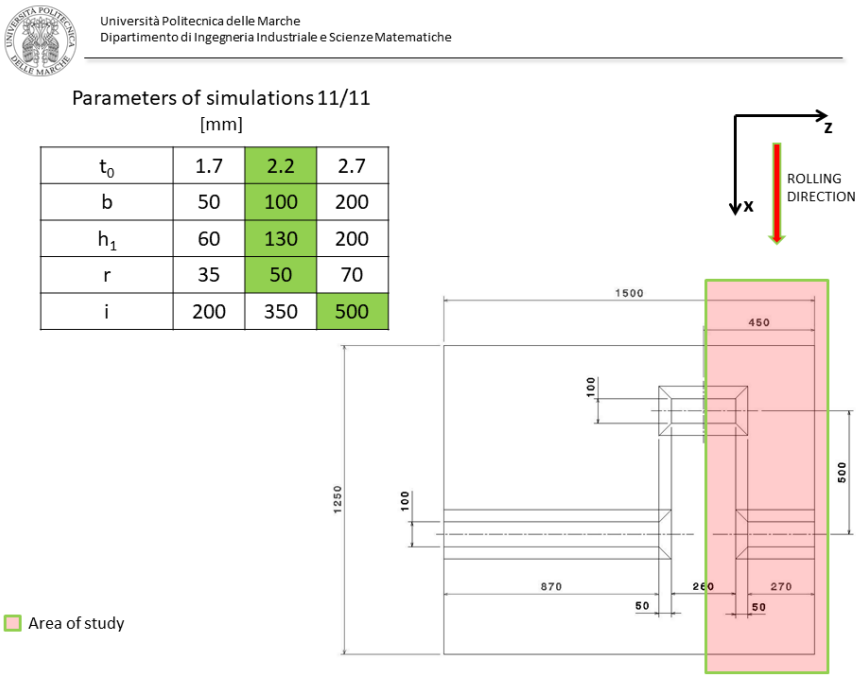

(h) Eleventh analysis settings

Figure 6.4

6.4 Analysis of the results

Different results were analysed to identify a strong correlation between parameters. Chapter 5.3 already identified critical points and possible defects of the finished work-piece. So great attention was paid to the thinning zone which usually appears after every patch, shear deformations magnitude and vertical displacement of the not-yet-laminated strip during the whole rolling history, which corresponds to the deformation generated by the temporary unbalanced state. For the first two result analyses, contour maps and extrapolated path data were used. For the last one, however, history plots of the displacement of a few nodes were generated by the program.

6.4.1 Analysis of the thinning areas

Maps of plastic strain vertical component and relative path plots will be reported hereafter. However, for a clear interpretation of the following results it is necessary to localize the considered paths. The Figure 6.5 shows the position of the 3 paths on the finished work-piece surface: path n.1 is located in the middle of the h_1 wide patch, path n.2 in the middle of the lengthwise transition zone and path n.3 in the middle of the h_2 wide patch.

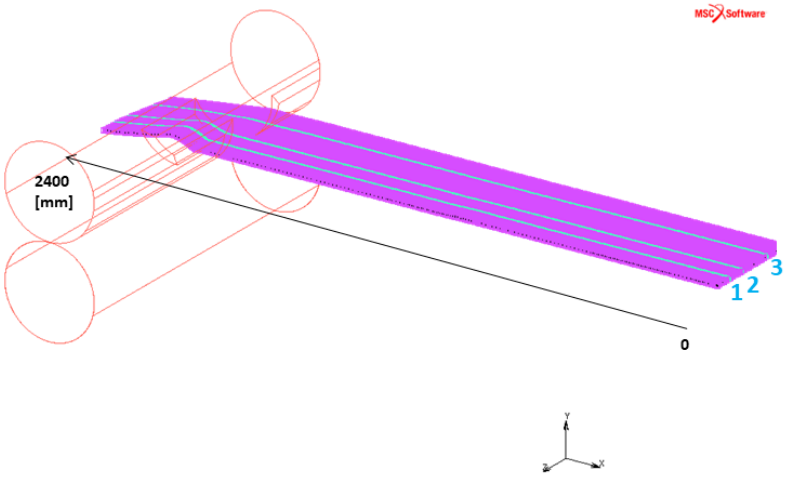

Figure 6.5 – Location of the paths for ε_{22} and $\varepsilon_{VonMises}$ evaluation

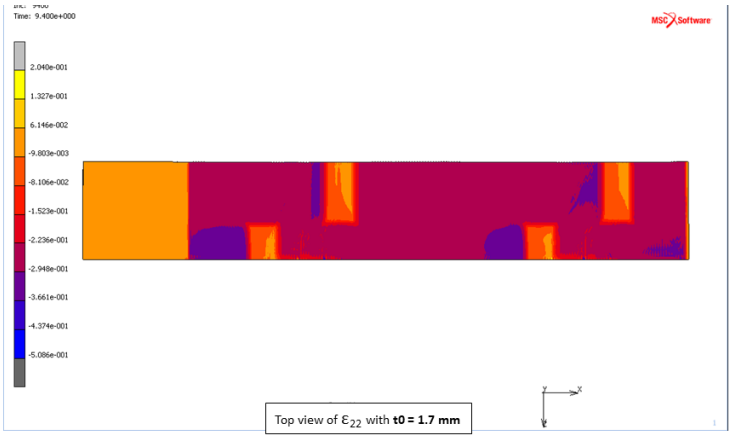

(a) ε_{22} with $t_1 = 1.7mm$

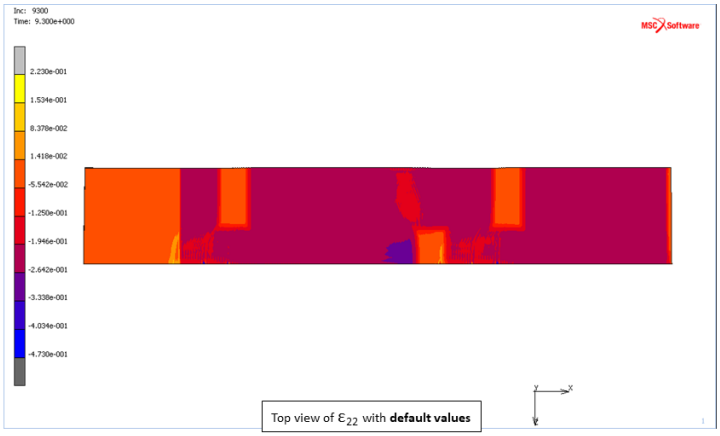

(b) ε_{22} with $t_1 = 2.2mm$

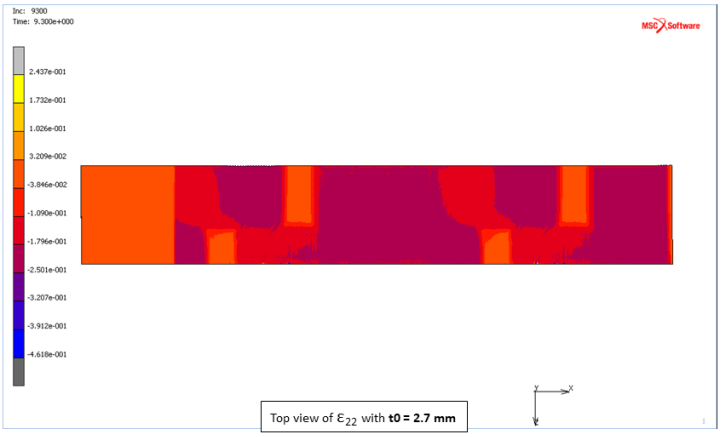

(c) ε_{22} with $t_1 = 2.7mm$

Figure 6.6

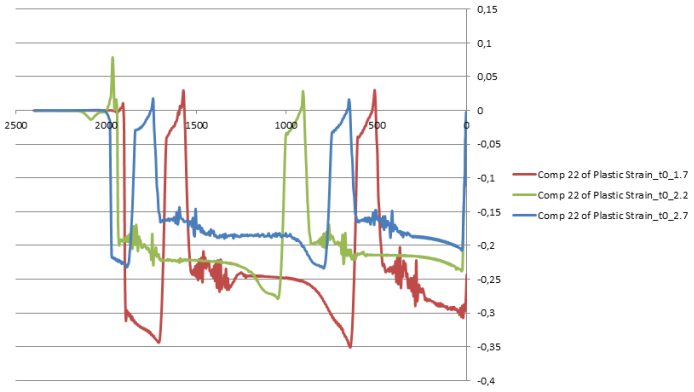

(a) ε_{22} - varying parameter:t_0 - Path n.1

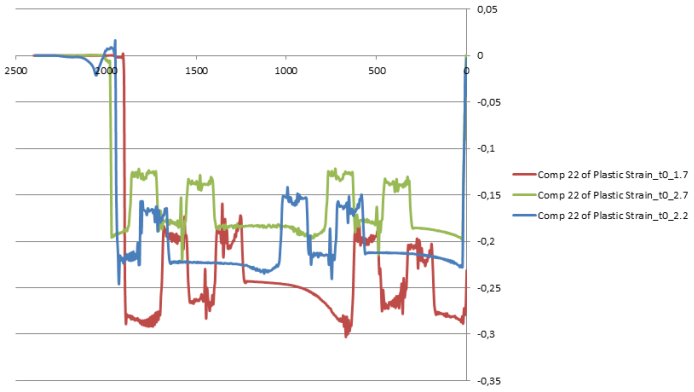

(b) ε_{22} - varying parameter:t_0 - Path n.2

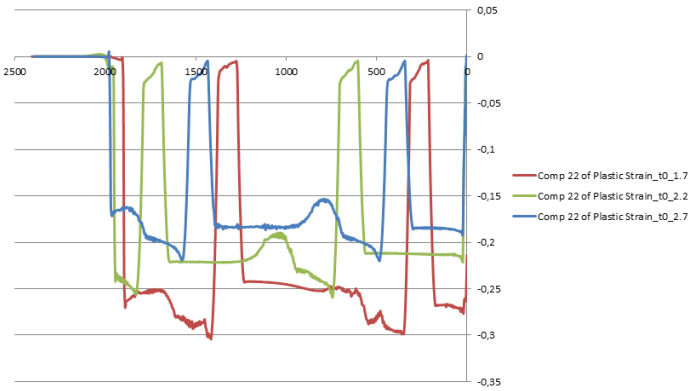

(c) ε_{22} - varying parameter:t_0 - Path n.3

Figure 6.7

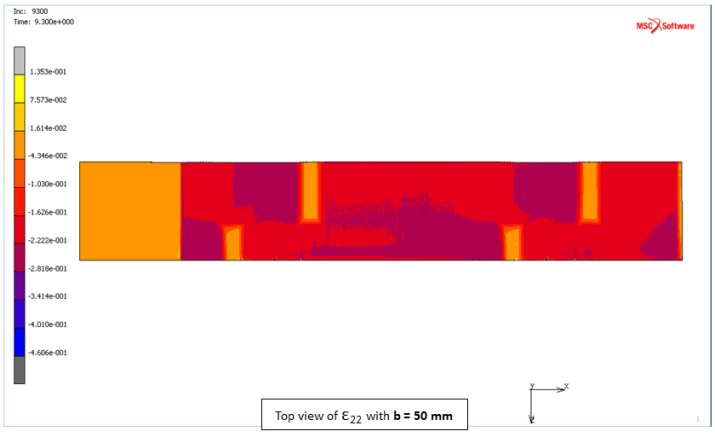

(a) ε_{22} with $b = 50mm$

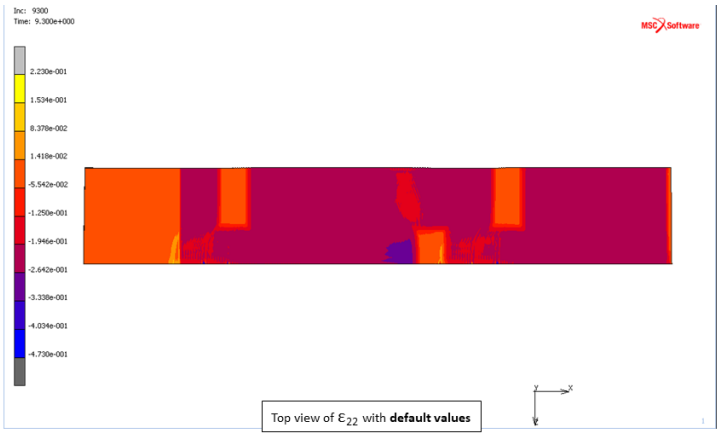

(b) ε_{22} with $b = 100mm$

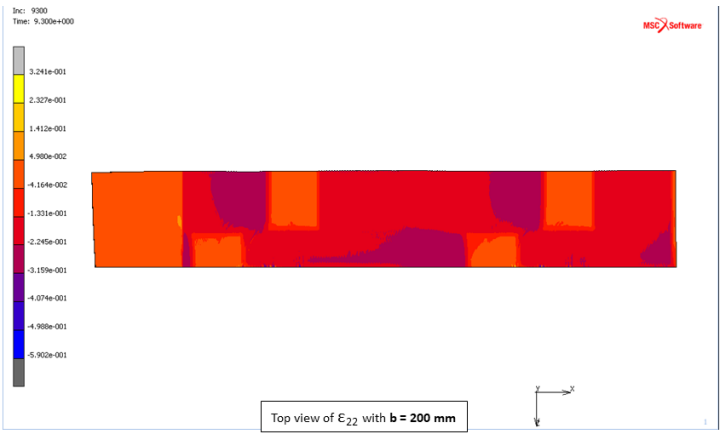

(c) ε_{22} with $b = 200mm$

Figure 6.8

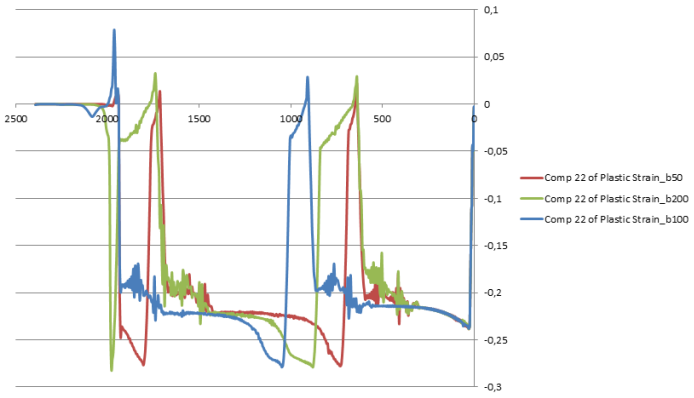

(a) ε_{22} - varying parameter:b - Path n.1

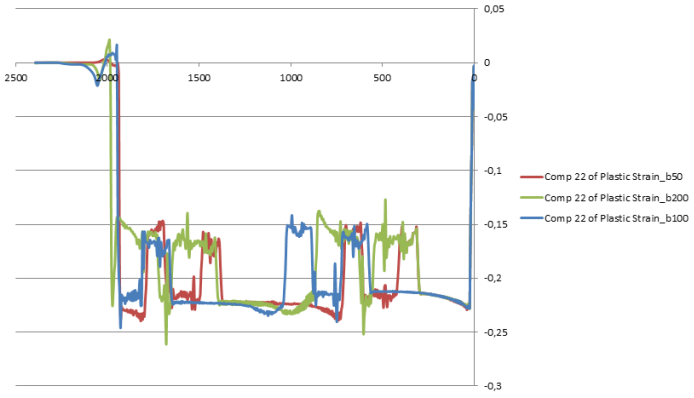

(b) ε_{22} - varying parameter:b - Path n.2

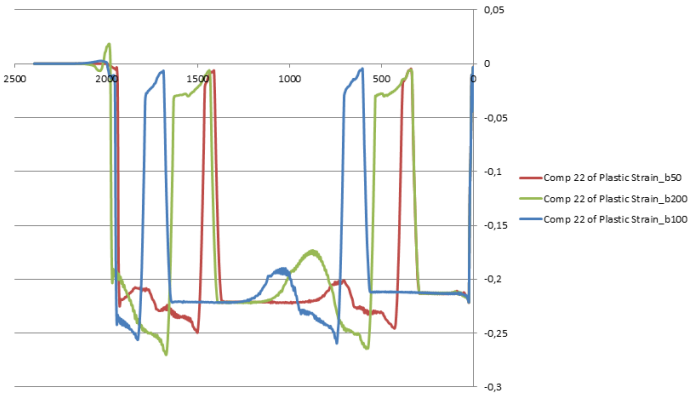

(c) ε_{22} - varying parameter:b - Path n.3

Figure 6.9

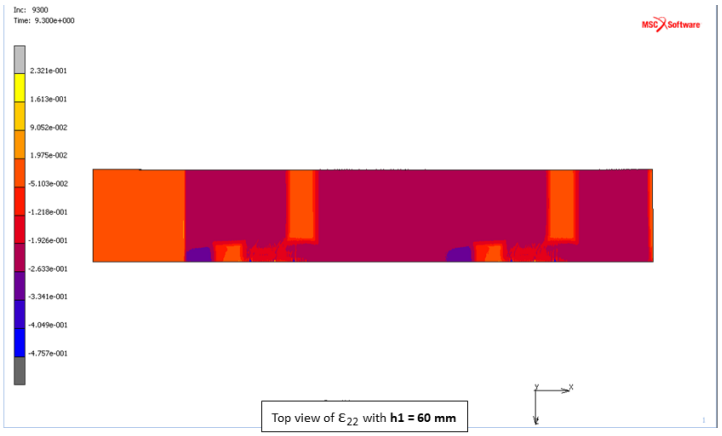

(a) ε_{22} with $h_1 = 60mm$

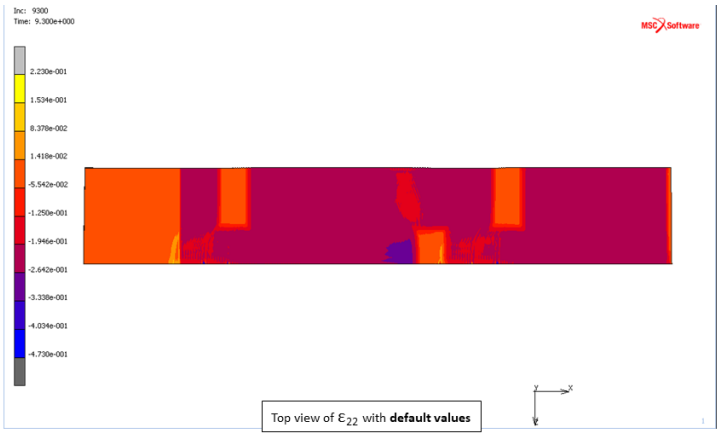

(b) ε_{22} with $h_1 = 130mm$

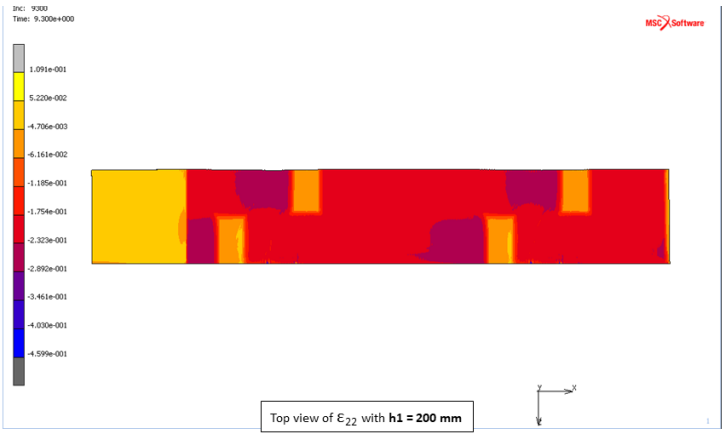

(c) ε_{22} with $h_1 = 200mm$

Figure 6.10

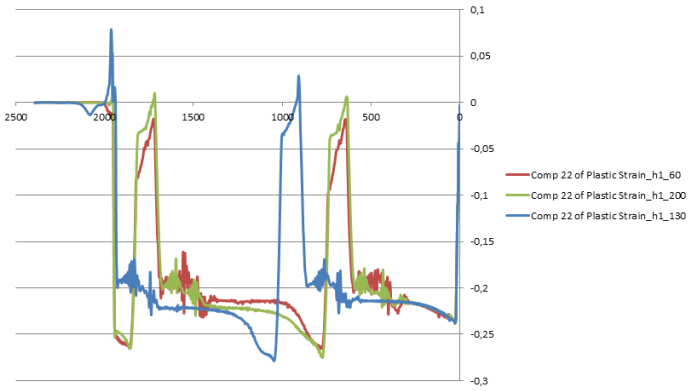

(a) ε_{22} - varying parameter:h_1 - Path n.1

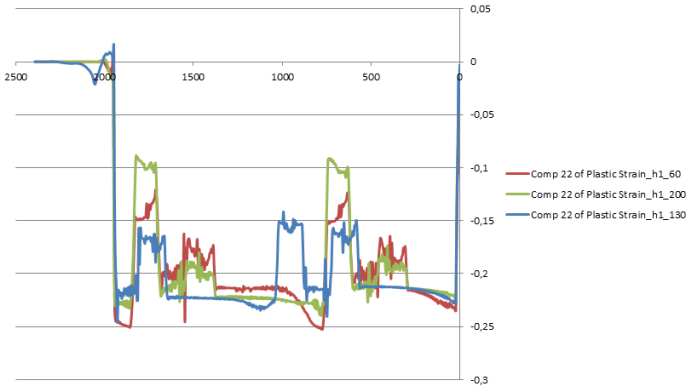

(b) ε_{22} - varying parameter:h_1 - Path n.2

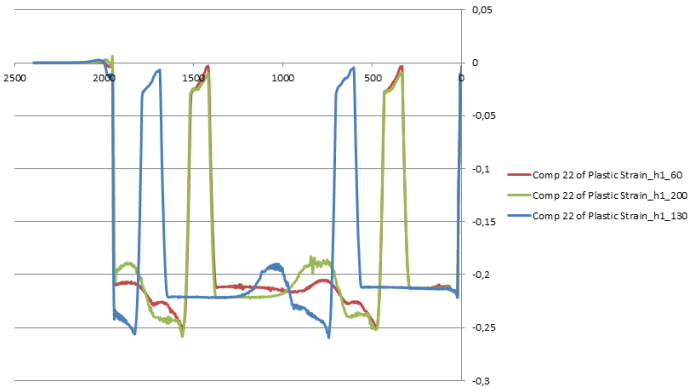

(c) ε_{22} - varying parameter:h_1 - Path n.3

Figure 6.11

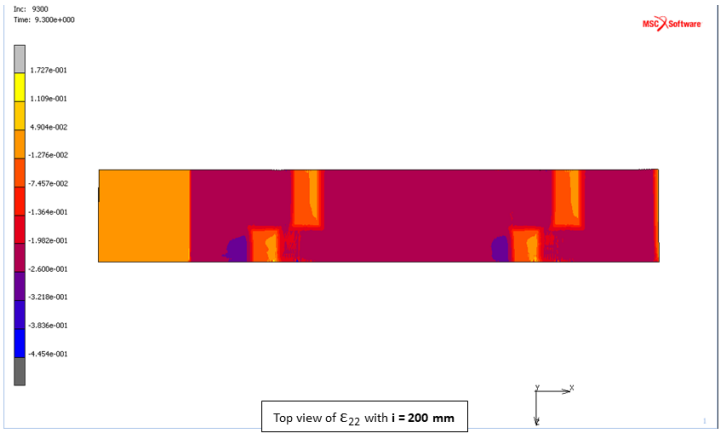

(a) ε_{22} with $i = 200mm$

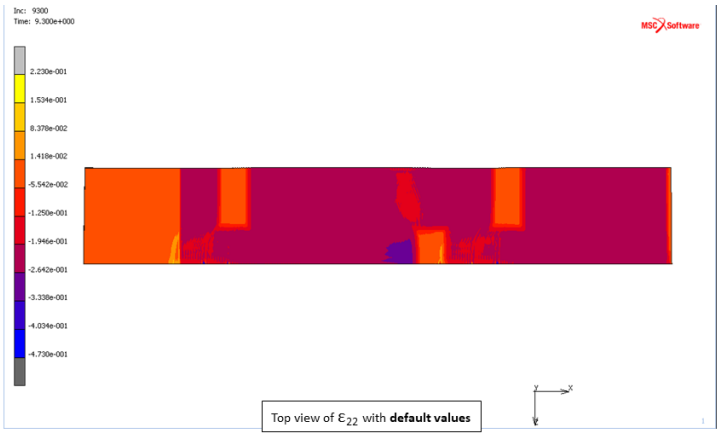

(b) ε_{22} with $i = 350mm$

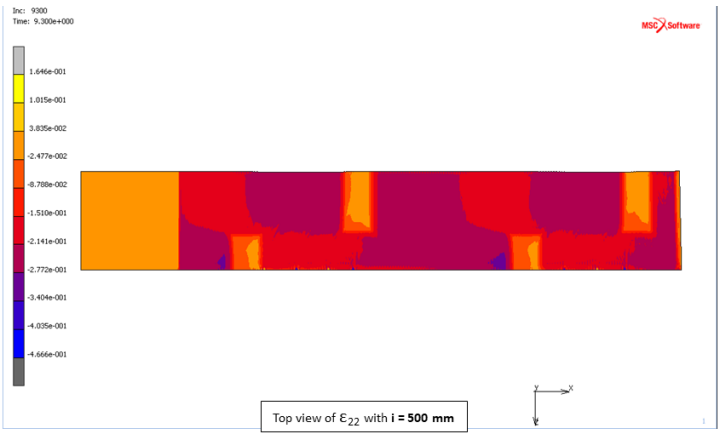

(c) ε_{22} with $i = 500mm$

Figure 6.12

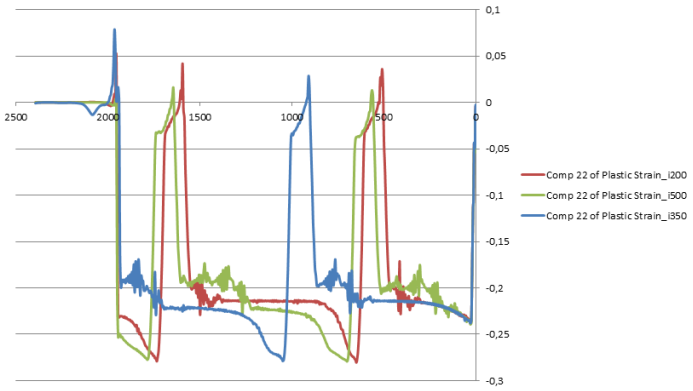

(a) ε_{22} - varying parameter:i - Path n.1

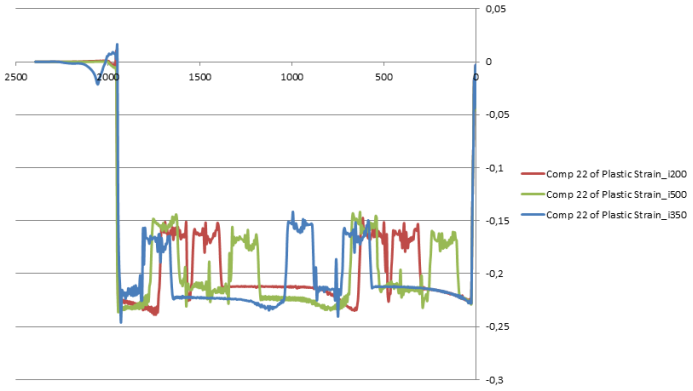

(b) ε_{22} - varying parameter:i - Path n.2

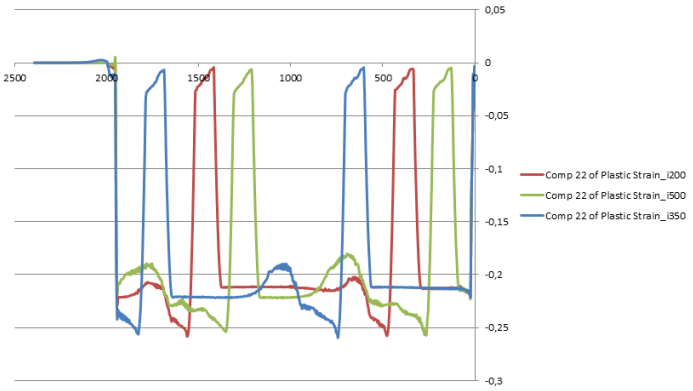

(c) ε_{22} - varying parameter:i - Path n.3

Figure 6.13

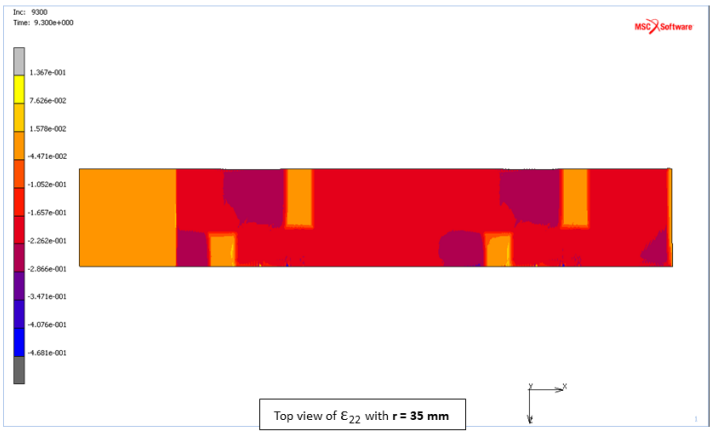

(a) ε_{22} with $r = 35mm$

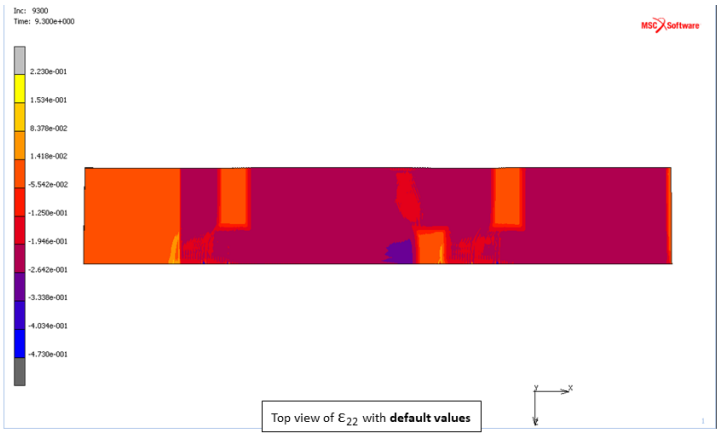

(b) ε_{22} with $r = 50mm$

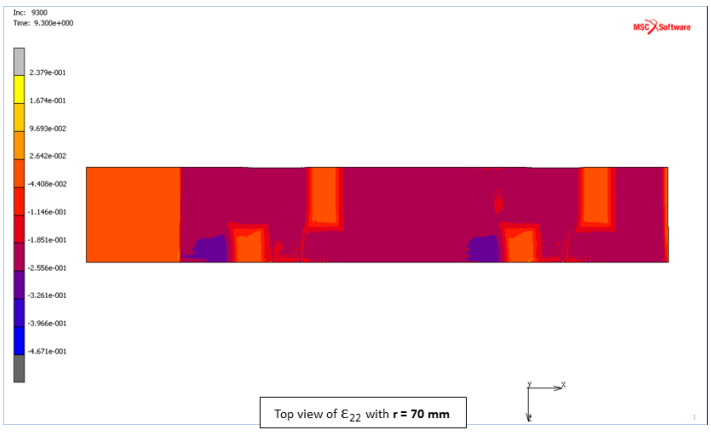

(c) ε_{22} with $r = 70mm$

Figure 6.14

Results were also analysed according to the DoE techniques. Table 6.4 shows the minimum value of ε_{22}, which corresponds to the size of the thinning area, for each simulation of the DoE.

Table 6.4 – DoE results in terms of ε_{22} minimum value

	t_0	b	h_1	r	i
-1	*-0,35076*	*-0,27771*	*-0,265567*	*-0,28039*	*-0,27999*
0	*-0,2789*	*-0,2789*	*-0,278898*	*-0,2789*	*-0,2789*
1	*-0,23392*	*-0,28131*	*-0,275263*	*-0,27918*	*-0,27673*

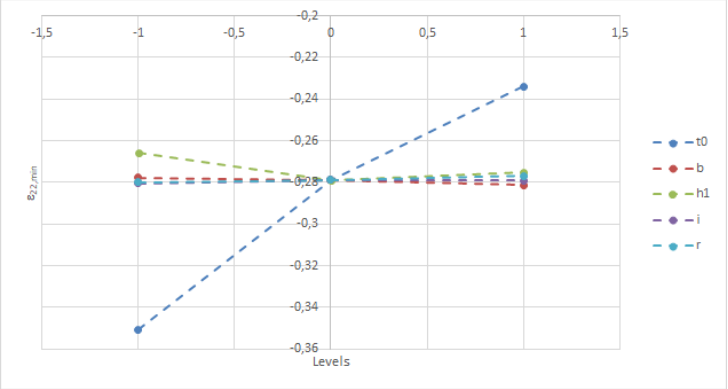

Figure 6.15 – Principal effects on ε_{22}

Table 6.5 – DoE results in terms of length of the thinning area

	t_0	b	h_1	r	i
-1	*195*	*115,27*	*148,11*	*151,25*	*147,17*
0	*150,74*	*150,74*	*150,74*	*150,74*	*150,74*
1	*125*	*205*	*152,16*	*149,15*	*151,46*

The study of the effects of the principal variables on the magnitude of the thinning area is shown in Figure 6.15. Curves highlight that characteristics of the thinning area only depend on t_0 and b. t_0, indeed, not only influences the magnitude of the thickness plastic strain in the area downstream of the patch, but also its length. b, on the other hand, only affects the extension of the

thinning area, which appears to be directly proportional to the patch length. h_1, i and r do not seem to have a direct influence on the thinning area.

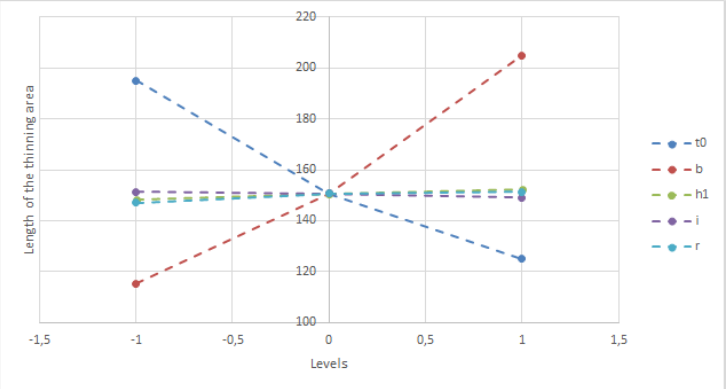

Figure 6.16 – Principal effects on length of the thinning area

6.4.2 Analysis of the shear deformation

Maps of the shear deformation component and its relative path plots will be reported hereafter. In this case also, for a clear interpretation of the results it is necessary to localize the considered paths. The Figure 6.17 shows the position of the 3 paths on the finished work-piece surface: path n.1 is located at the end of the h_1 wide patch where the transition area starts, path n.2 in the middle of the lengthwise transition zone and path n.3 at the end of the h_2 wide patch where the transition area starts.

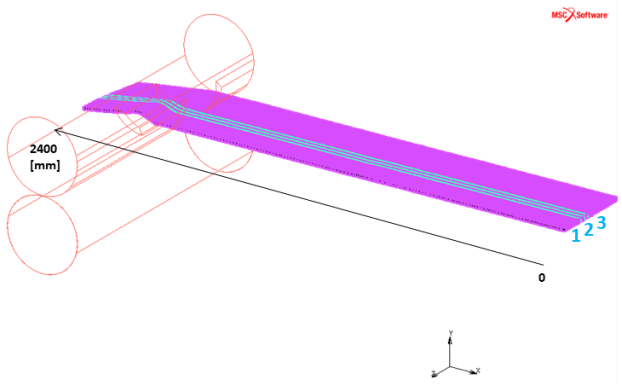

Figure 6.17 – Location of the paths for $\varepsilon_{31} = \frac{\gamma_{31}}{2}$ evaluation

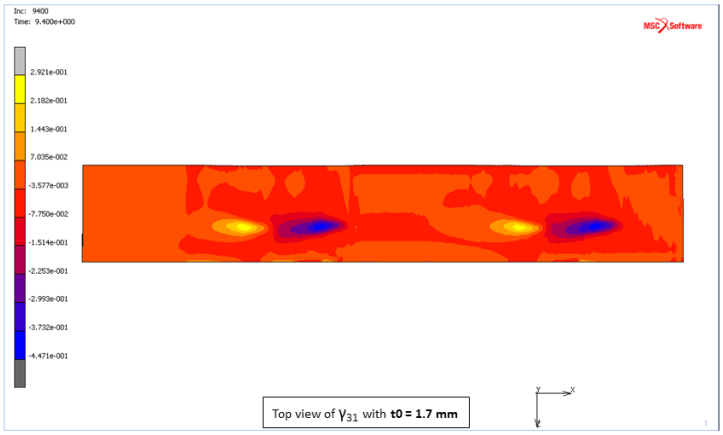

(a) $\varepsilon_{31} = \frac{\gamma_{31}}{2}$ with $t_0 = 1.7mm$

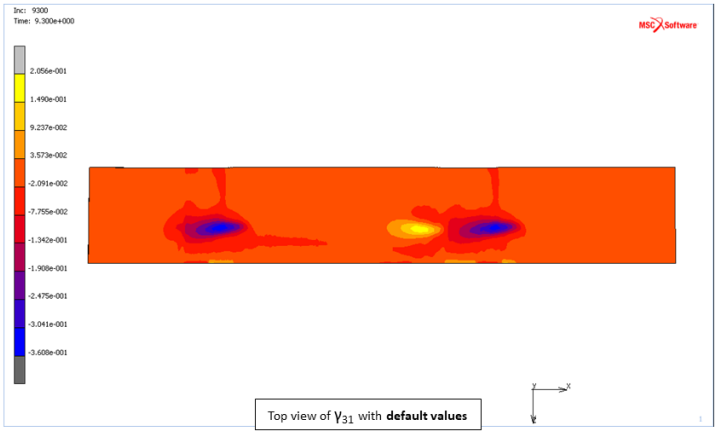

(b) $\varepsilon_{31} = \frac{\gamma_{31}}{2}$ with $t_0 = 2.2mm$

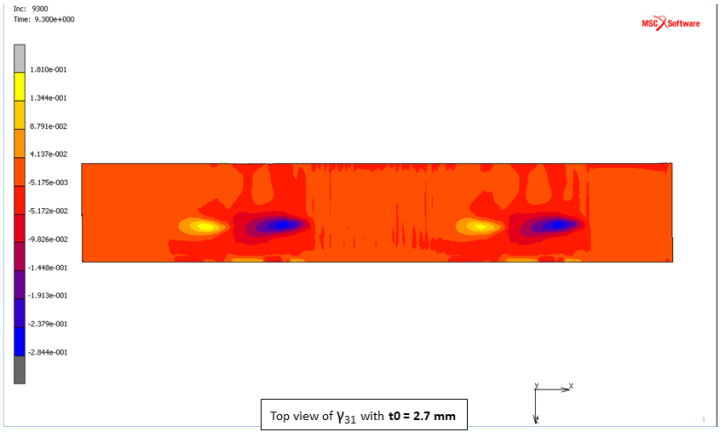

(c) $\varepsilon_{31} = \frac{\gamma_{31}}{2}$ with $t_0 = 2.7mm$

Figure 6.18

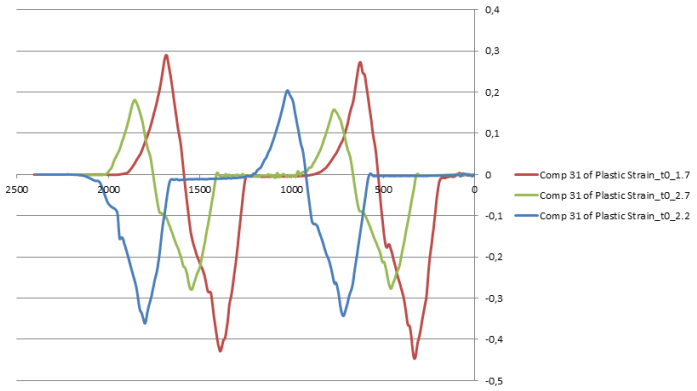

(a) $\varepsilon_{31} = \frac{\gamma_{31}}{2}$ - varying parameter:t_0 - Path n.1

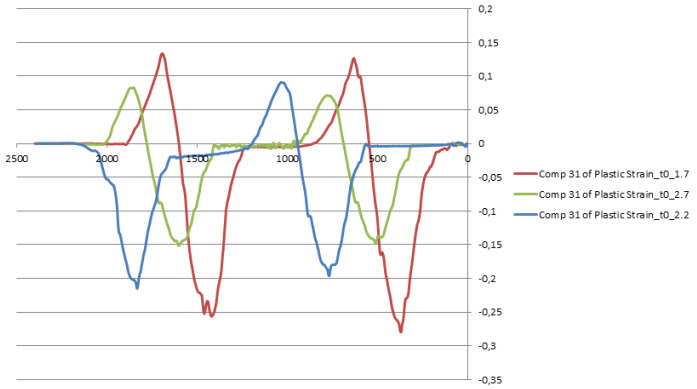

(b) $\varepsilon_{31} = \frac{\gamma_{31}}{2}$ - varying parameter:t_0 - Path n.2

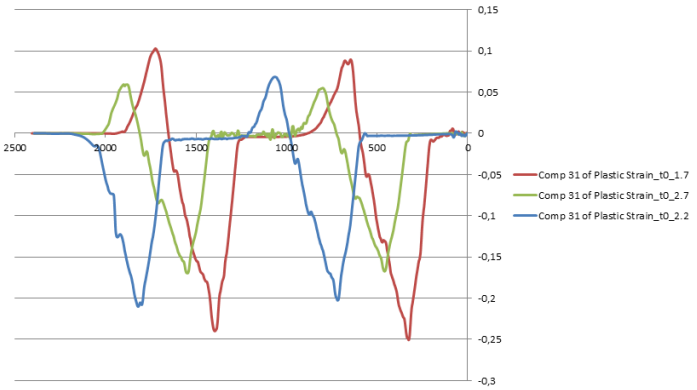

(c) $\varepsilon_{31} = \frac{\gamma_{31}}{2}$ - varying parameter:t_0 - Path n.3

Figure 6.19

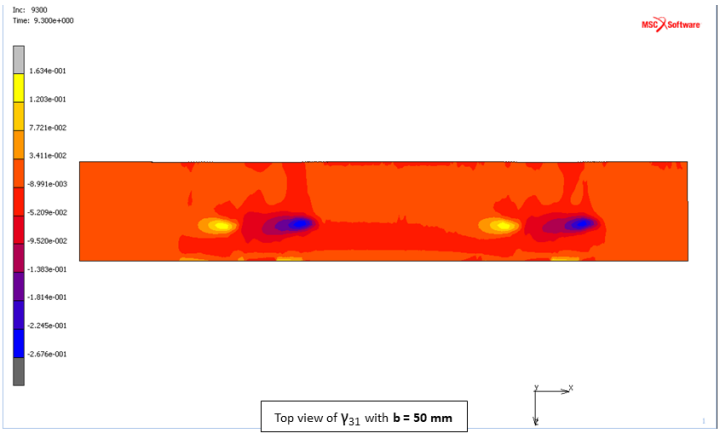

(a) $\varepsilon_{31} = \frac{\gamma_{31}}{2}$ with $b = 50mm$

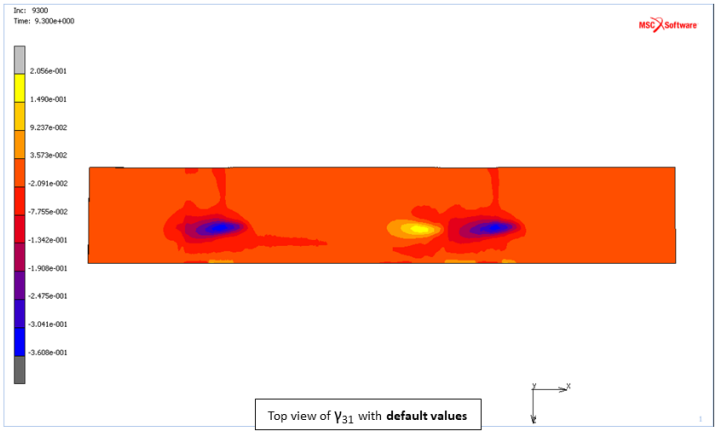

(b) $\varepsilon_{31} = \frac{\gamma_{31}}{2}$ with $b = 100mm$

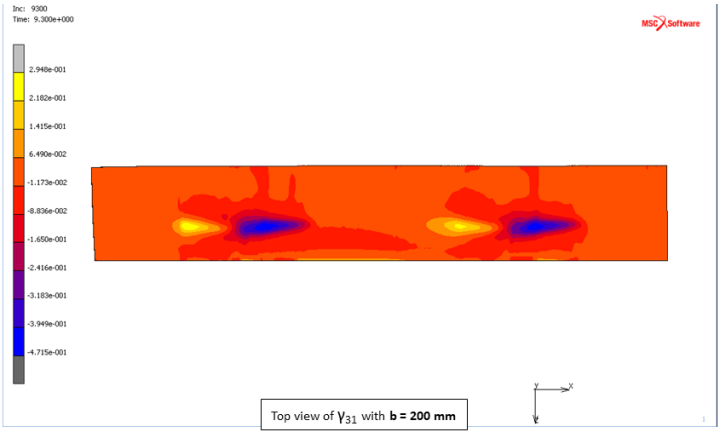

(c) $\varepsilon_{31} = \frac{\gamma_{31}}{2}$ with $b = 200mm$

Figure 6.20

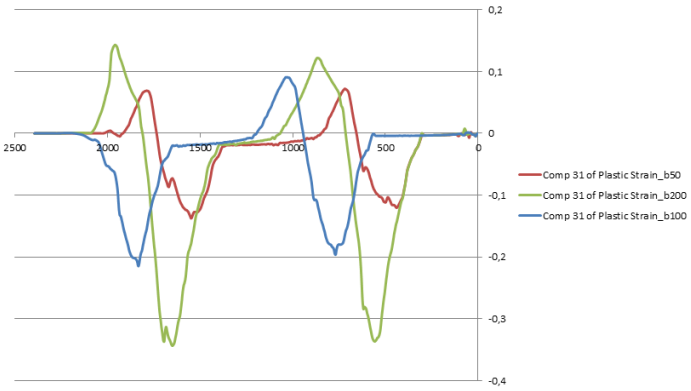

(a) $\varepsilon_{31} = \frac{\gamma_{31}}{2}$ - varying parameter:b - Path n.1

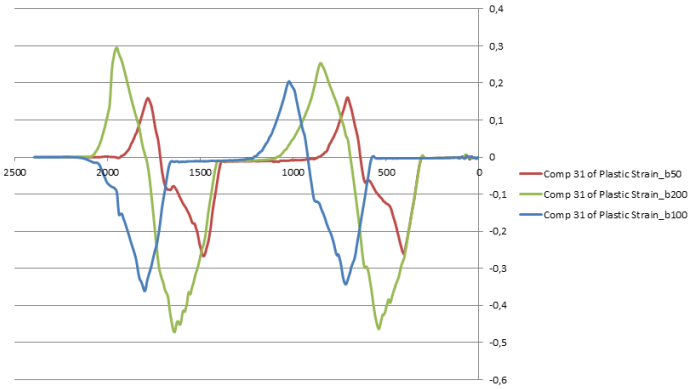

(b) $\varepsilon_{31} = \frac{\gamma_{31}}{2}$ - varying parameter:b - Path n.2

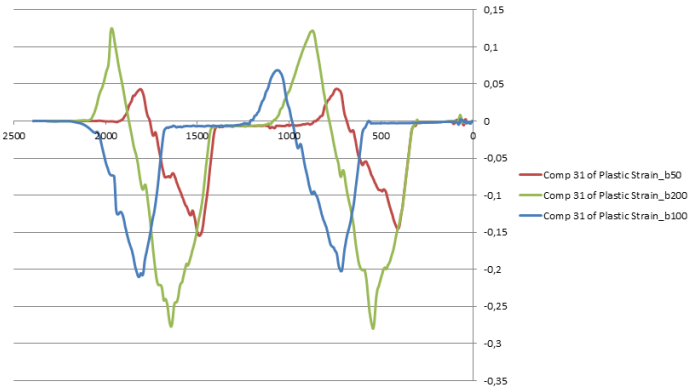

(c) $\varepsilon_{31} = \frac{\gamma_{31}}{2}$ - varying parameter:b - Path n.3

Figure 6.21

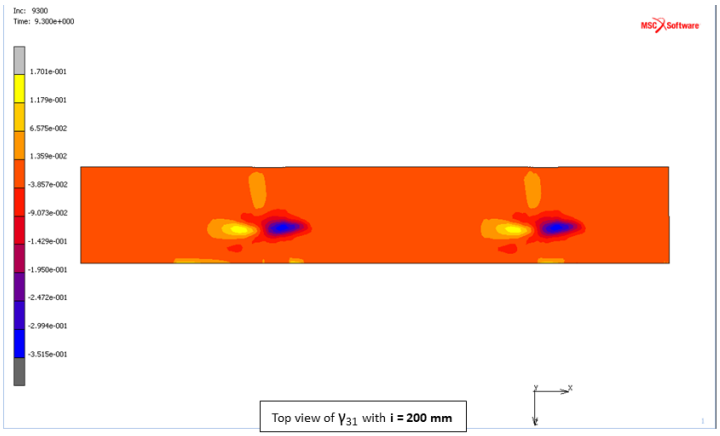

(a) $\varepsilon_{31} = \frac{\gamma_{31}}{2}$ with $i = 200mm$

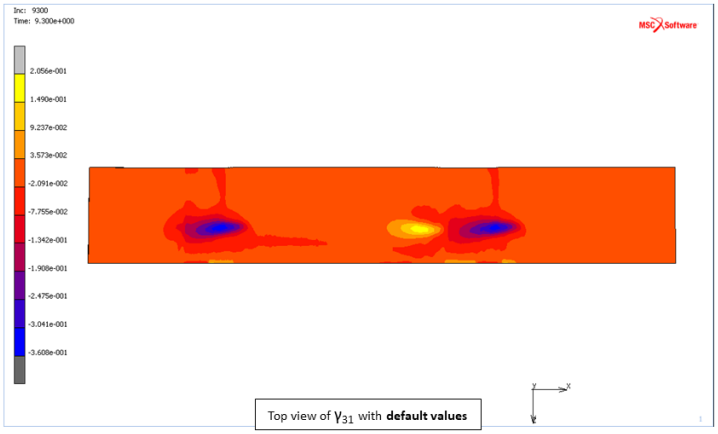

(b) $\varepsilon_{31} = \frac{\gamma_{31}}{2}$ with $i = 350mm$

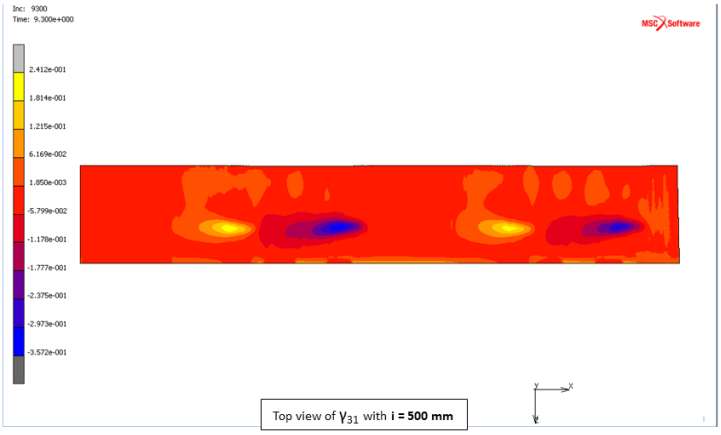

(c) $\varepsilon_{31} = \frac{\gamma_{31}}{2}$ with $i = 500mm$

Figure 6.22

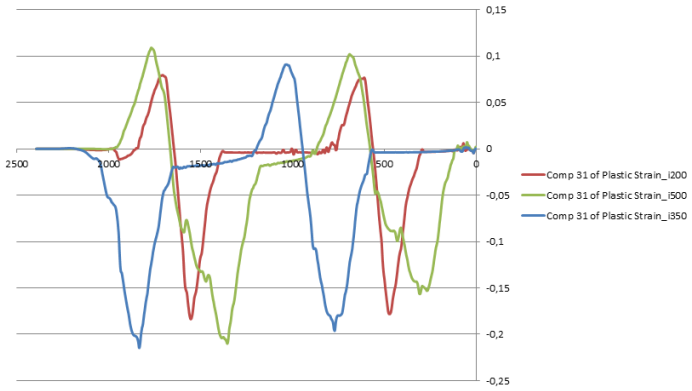

(a) $\varepsilon_{31} = \frac{\gamma_{31}}{2}$ - varying parameter:i - Path n.1

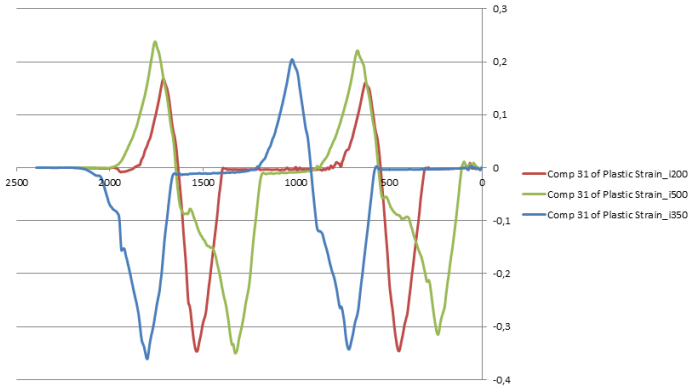

(b) $\varepsilon_{31} = \frac{\gamma_{31}}{2}$ - varying parameter:i - Path n.2

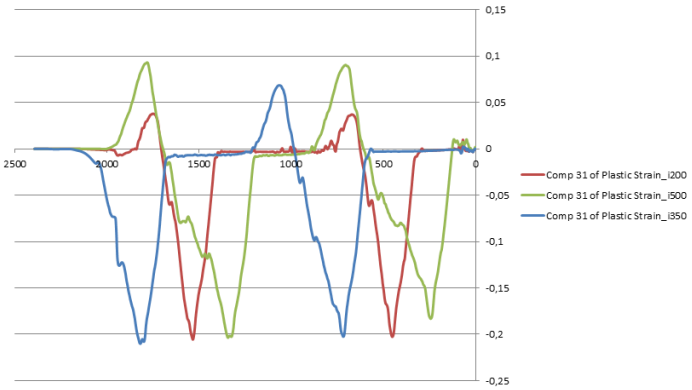

(c) $\varepsilon_{31} = \frac{\gamma_{31}}{2}$ - varying parameter:i - Path n.3

Figure 6.23

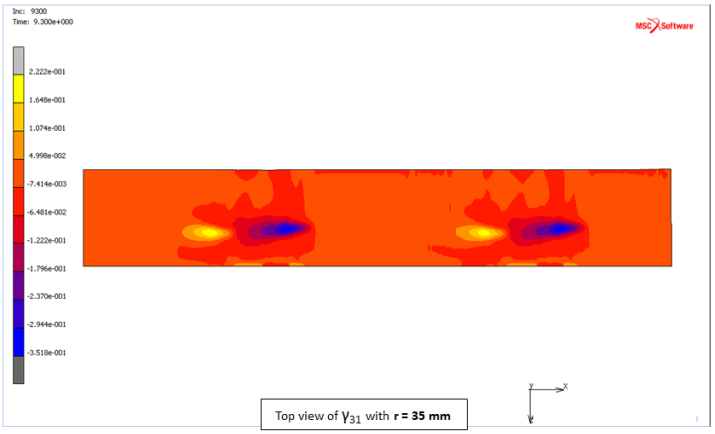

(a) $\varepsilon_{31} = \frac{\gamma_{31}}{2}$ with $r = 35mm$

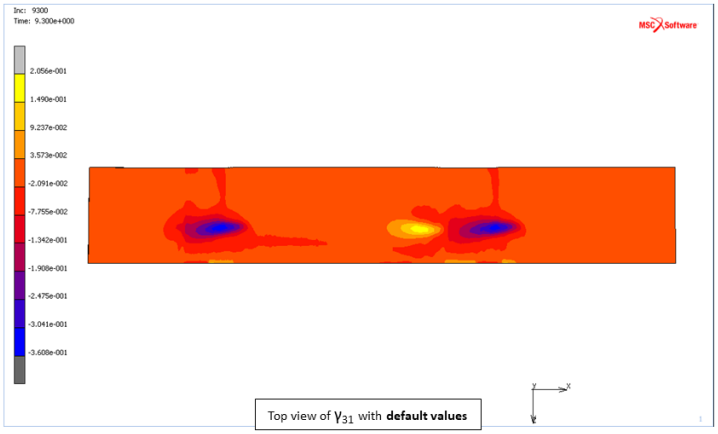

(b) $\varepsilon_{31} = \frac{\gamma_{31}}{2}$ with $r = 50mm$

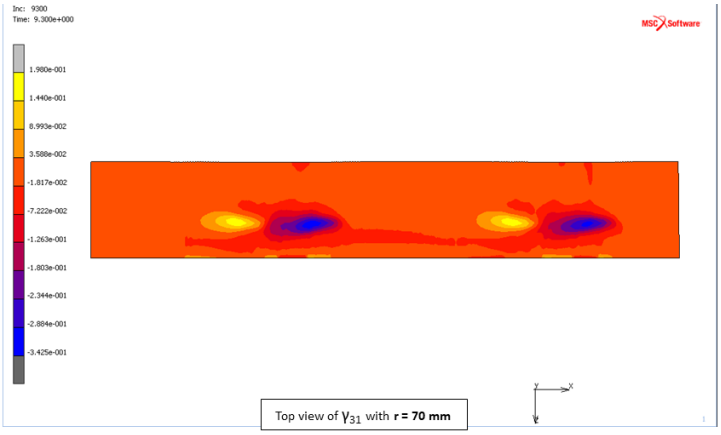

(c) $\varepsilon_{31} = \frac{\gamma_{31}}{2}$ with $r = 70mm$

Figure 6.24

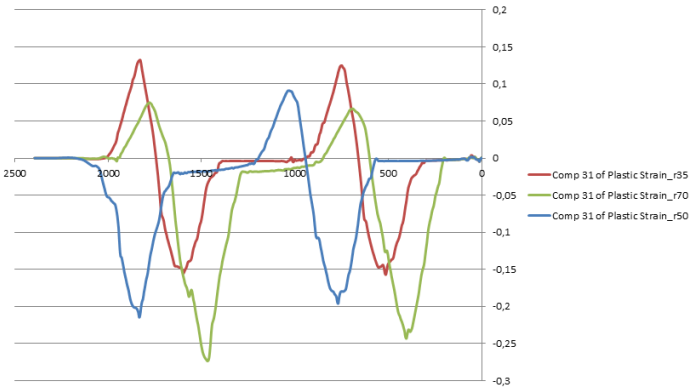

(a) $\varepsilon_{31} = \frac{\gamma_{31}}{2}$ - varying parameter:r - Path n.1

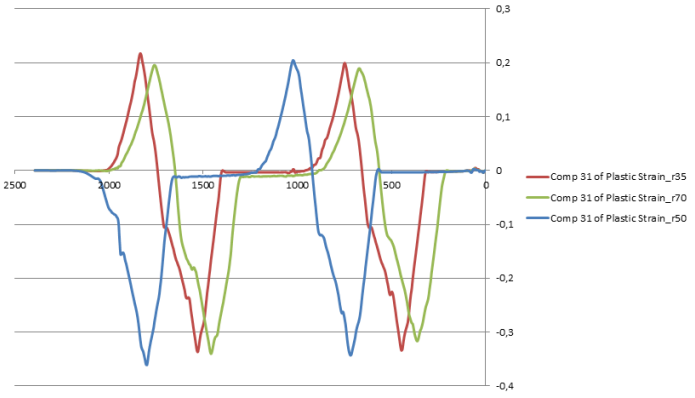

(b) $\varepsilon_{31} = \frac{\gamma_{31}}{2}$ - varying parameter:r - Path n.2

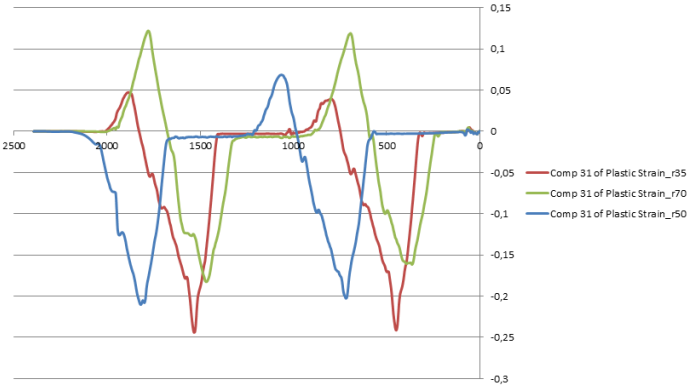

(c) $\varepsilon_{31} = \frac{\gamma_{31}}{2}$ - varying parameter:r - Path n.3

Figure 6.25

Results were also analysed according to the DoE techniques. Table 6.6 shows the minimum value of ε_{31} for each simulation of the DoE.

Table 6.6 – DoE results in terms of ε_{31} minimum value

	t_0	b	h_1	r	i
-1	*-0,4467*	*-0,26707*	*-0,33301*	*-0,34681*	*-0,33658*
0	*-0,36075*	*-0,36075*	*-0,36075*	*-0,36075*	*-0,36075*
1	*-0,27902*	*-0,47152*	*-0,29938*	*-0,34999*	*-0,34007*

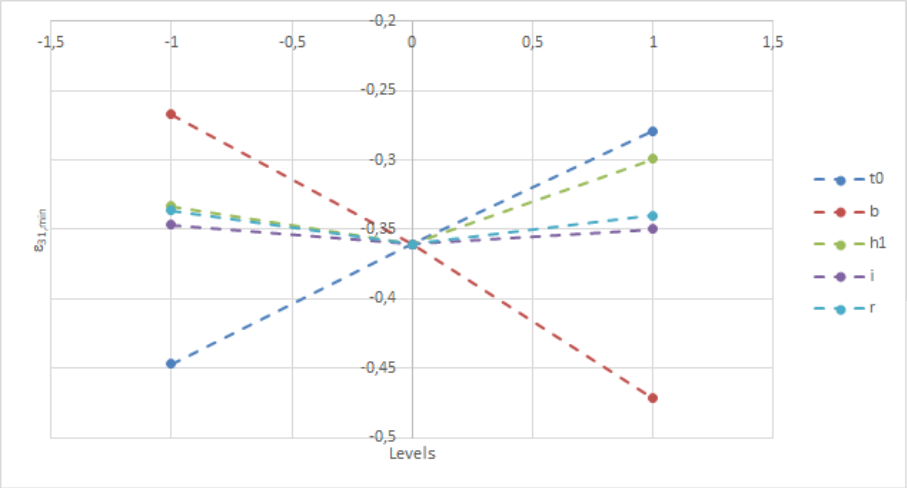

Figure 6.26 – Principal effects on ε_{31}

Table 6.7 – DoE results in terms of amplitude of shear deformation range

	t_0	b	h_1	r	i
-1	*0,736688*	*0,428107*	*0,560075*	*0,514528*	*0,553776*
0	*0,565158*	*0,565158*	*0,565158*	*0,565158*	*0,565158*
1	*0,459583*	*0,765848*	*0,517272*	*0,588052*	*0,535596*

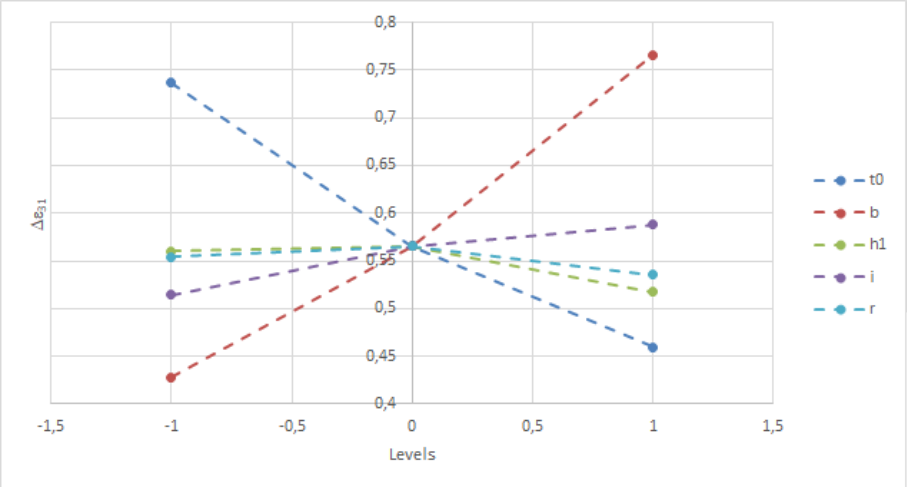

Figure 6.27 – Principal effects on the amplitude of shear deformation range

Results showed a strong relationship between the shear deformation magnitude and initial thickness, lengthwise size of the patch and transition zone. The magnitude of t_0, as well as b, highly affects the maximum value or rather the amplitude of the ε_{31} as shown in Figure 6.26 and Figure 6.27. Similar remarks may be made about the influence of r. Figure 6.27 shows that the Δ between minimum and maximum peaks tends to decrease as the transition zone grows. Unfortunately, the selected values are too similar to appreciate the influence of r, so an analytical investigation was conducted as well.

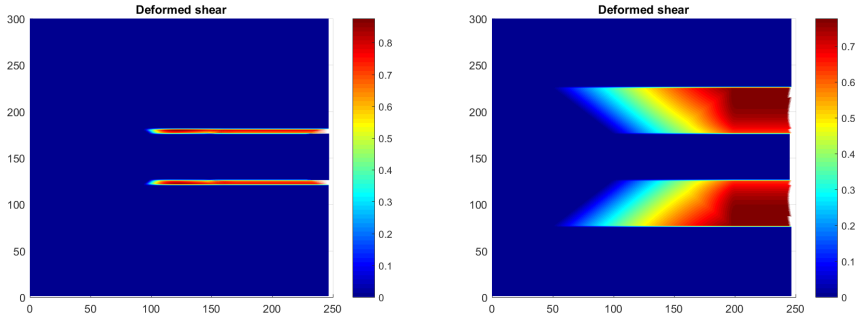

(a) Shear deformation - fillet radius: r = 5mm (b) Shear deformation - fillet radius: r = 50mm

Figure 6.28

Exploiting the same Matlab procedure in Chapter 5.4, further important considerations were taken about the transition zones. This size is strictly related to the fillet radius applied between the two different thickness areas. So the greater value is the fillet radius and the lower value is the shear deformation maximum in modulus, as shown in Figure 6.28a and Figure 6.28b.

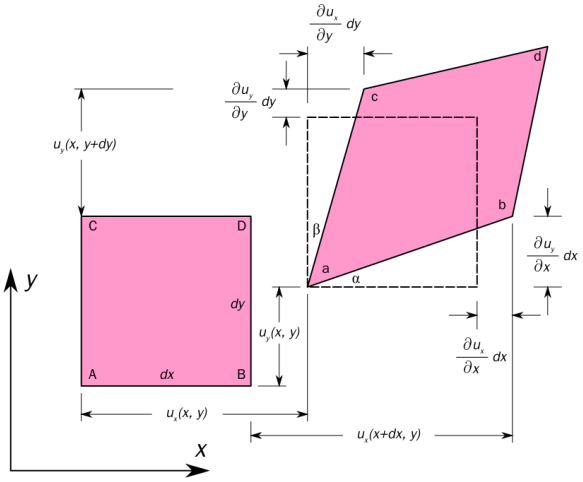

Figure 6.29 – 2D geometric deformation of an infinitesimal material element

This concept can be easily explained through simple math considerations. The engineering definition of shear strain (γ_{xy}), that is the change in angle between two lines of an infinitesimal material element (e.g. $\bar{AC}$ and $\bar{AB}$ in Figure 6.29), can be applied to the transition zone of the present case study. In addition, a very easy finite element method model was developed, to better demonstrate the issue.

Assuming the patch length and the reduction ratio to be constant, γ_{xy} can be calculated for the two different fillet radii where the former is equal to 5mm (Figure 6.30a) and the latter is equal to 50mm (Figure 6.30a).

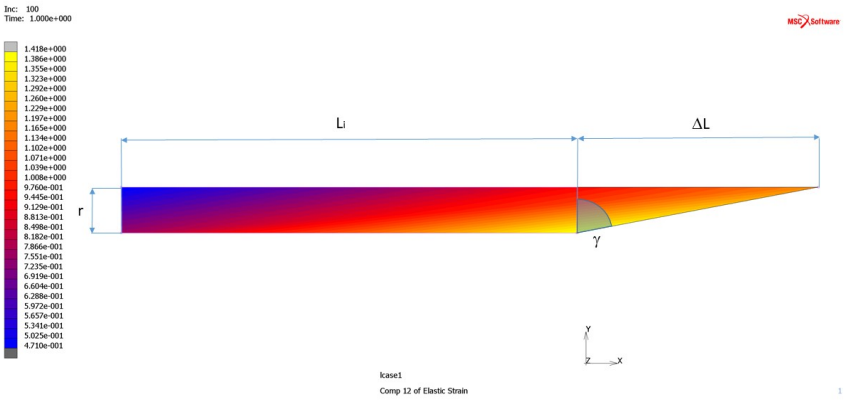

(a) FEM Shear deformation - fillet radius 5mm

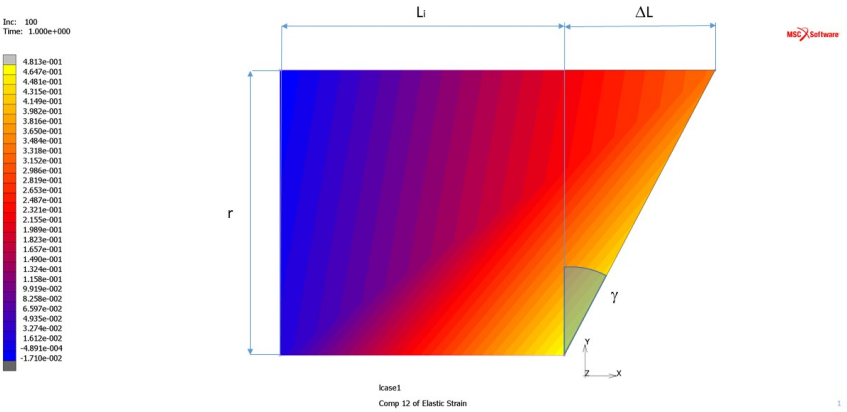

(a) FEM Shear deformation - fillet radius 50mm

Figure 6.30

Chapter 7

Real case application

In light of all the previous results and considerations, a real case application was analysed starting from the patch distribution until the prototype realisation. The study concerned the weight- and cost reduction of a VAN, and specifically its lateral sliding door.

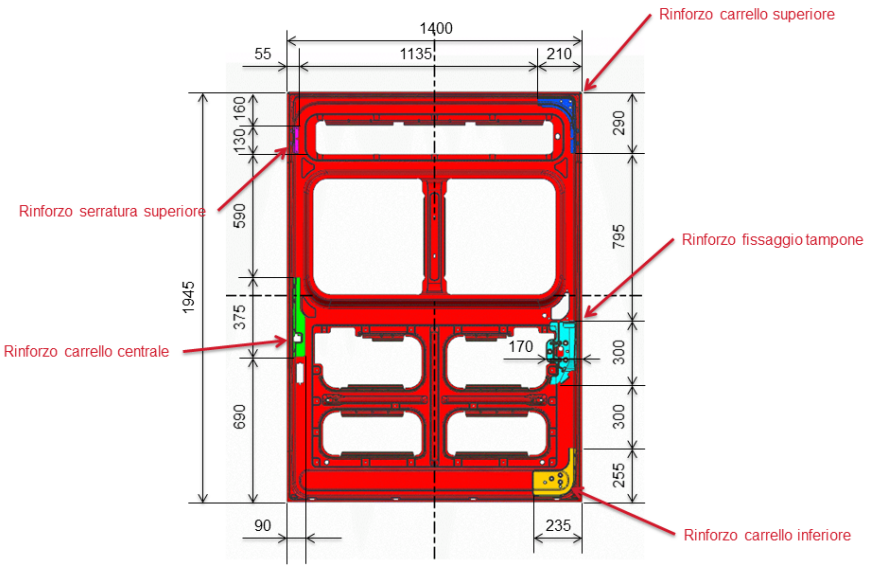

Figure 7.1 – Basic frame of the considered sliding door

The frame, which was previously made by steel, had to be redesigned using an aluminium alloy with a nominal thickness of $1.4mm$. The rolled product, moreover, had to be manufactured with the desired over-thickness areas exactly

where the following welded joints were planned. Previously, once the door frame was stamped and cut out, five metal plates had to be welded on it as reinforcement for the following application by welding of catches and latches, as shown in Figure 7.1

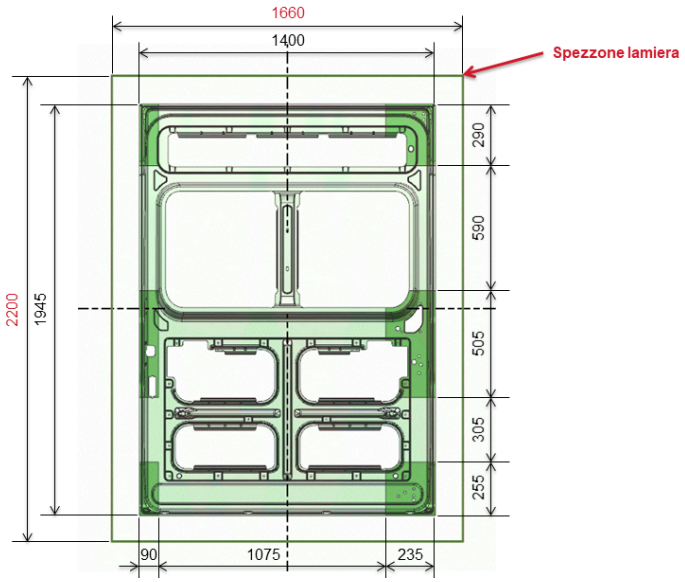

Figure 7.2 – Over-thickness areas identification

Figure 7.2 shows a hypothetical distribution of the over-thickness areas with a local thickness value of $2.1mm$.

In order to construct the present prototype, an aluminium producer decided to make its cold rolling mill plant available, introducing this way the width limit of $1660mm$ and the length limit of $1250mm$ of the laminated product. To overcome this issue, the considered work-piece had to be obtained by two rotations of cylinders. The research group could not find a good solution for a unique continuous work-piece because of the different patch distribution needed between the first rotation and the second one. So by exploiting an axial symmetry, the work-piece was obtained as shown in Figure 7.3 and 7.4.

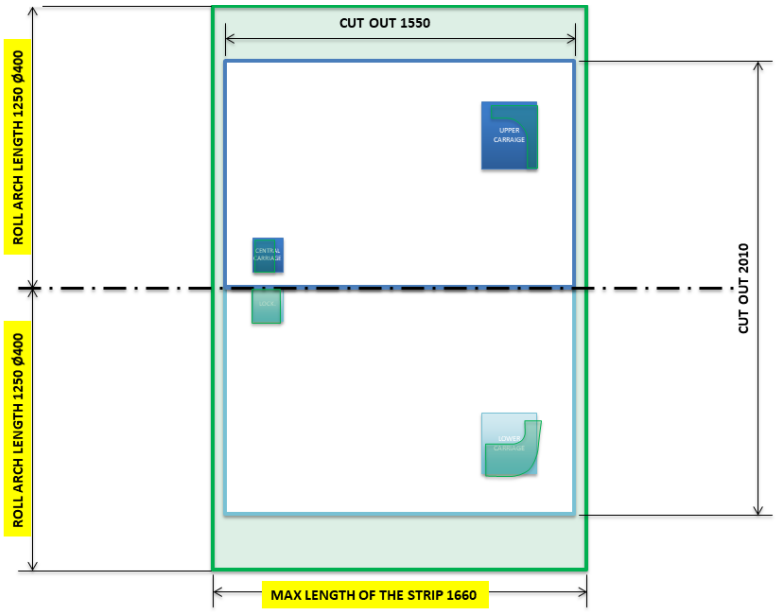

Figure 7.3 – Ideal patch distribution on the welded blank

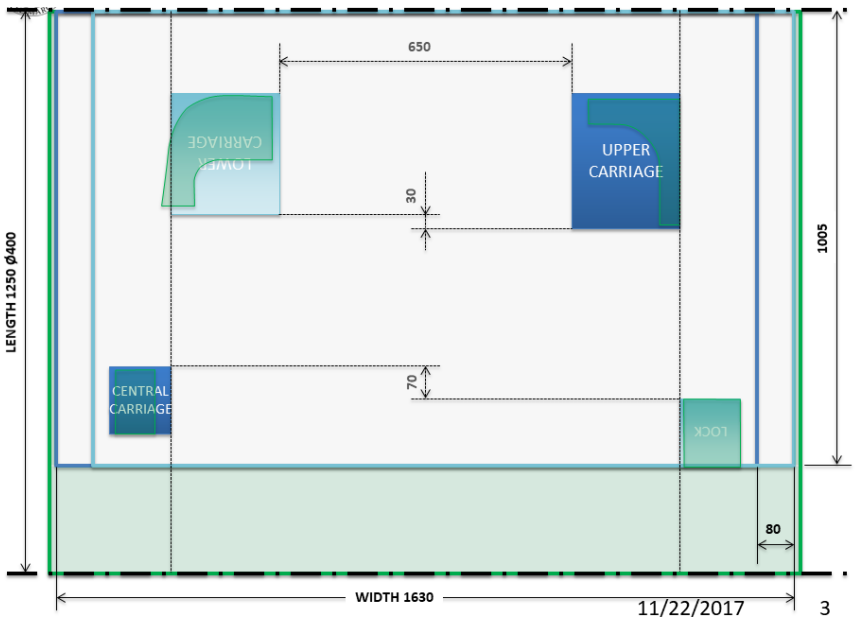

Figure 7.4 – Patch distribution according to the symmetry

Figure 7.5 shows a hypothetical distribution of the patches, including the

diamond shaped tips of the patches, in order to reduce the shear deformation magnitude.

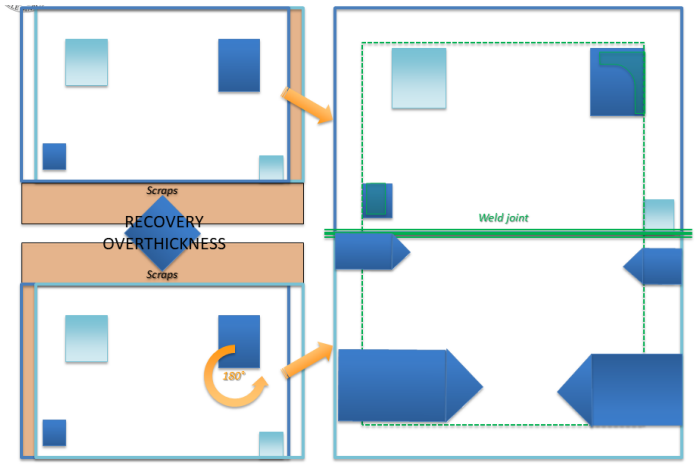

Figure 7.5 – Definitive patch shape and distribution

Figure 7.6 shows the sketch of the patch distribution to be enveloped on the cylinder to create the work-roll. So the obtained work-roll is shown in Figure 7.7.

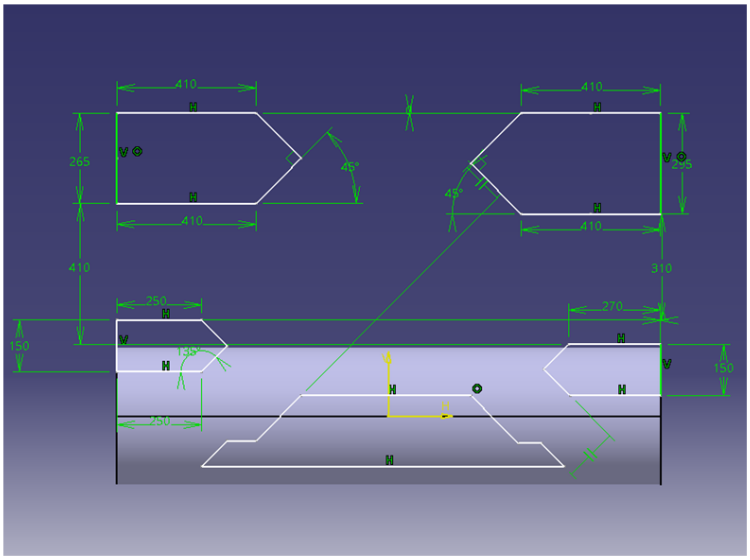

Figure 7.6 – Patch sketch to be enveloped on the base cylinder

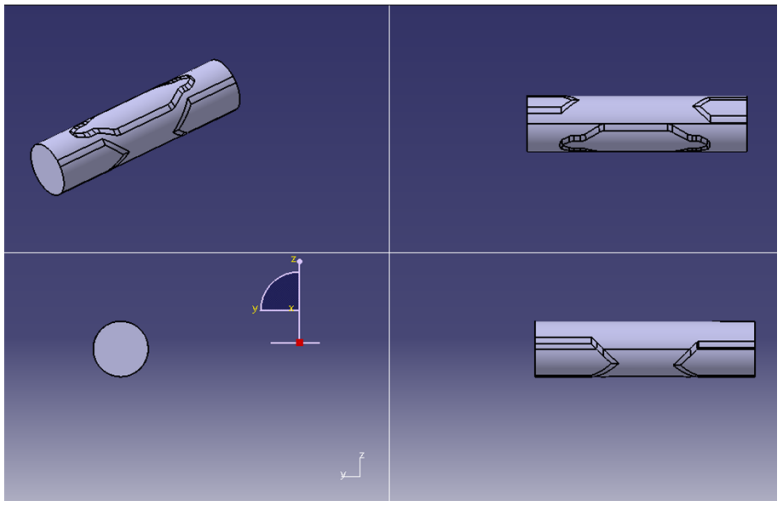

Figure 7.7 – Views of the obtained work-roll

A F.E.M. model with the geometry in question was performed to validate the chosen patch distribution. Looking at the results, it is worth noting how a complete rotation of the work-roll can influence the deformation of the work-piece. The different deformation of the strip between a complete rotation [Figure 7.8a] and a partial one [Figure 7.8b] confirms the importance of the complete balance. Whilst the complete balance is guaranteed, the twist of the strip during the rolling process may lead to considerable plastic deformation.

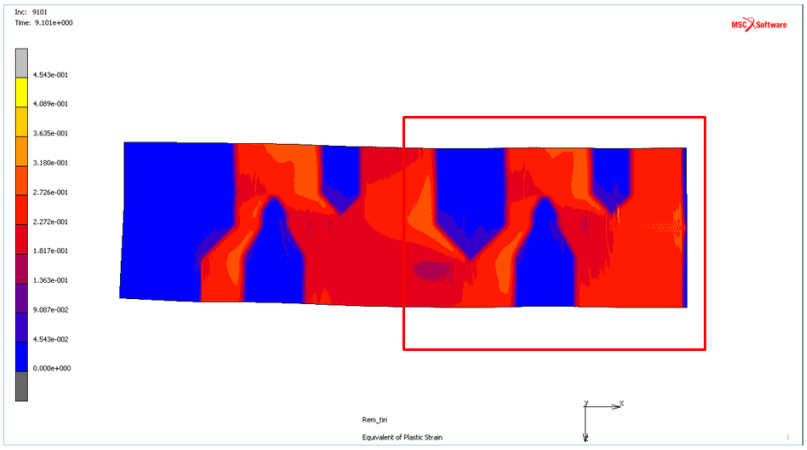

(a) Particulars of first rotation results

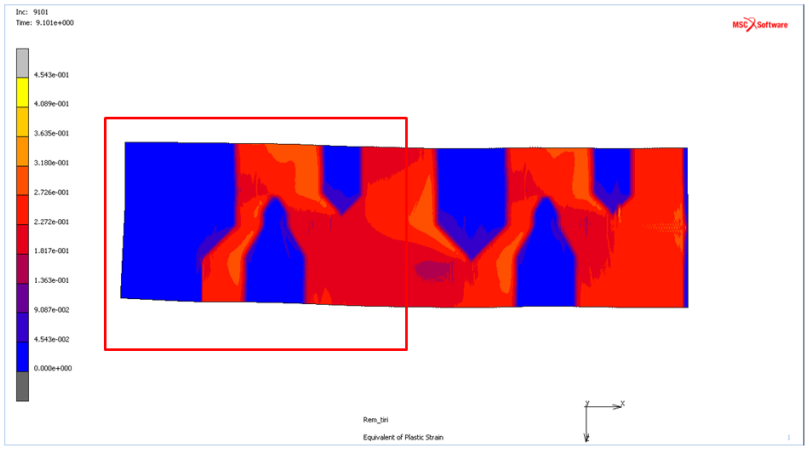

(b) Particulars of not-yet-completed second rotation results

Figure 7.8

7.1 Small scale experimental test

A small scale preliminary experimental test was led. The rolling plant shown in Figure 7.9 is a 4Hi hydraulic cold rolling mill with 125mm diameter of the work-rolls.

Figure 7.9 – Cold rolling mill for small scale tests

A work cylinder was wrought according to the previous geometry (Figure 7.10), by obtaining a pocket with a depth of 0.4mm. The only difference with the F.E.M. model is that the geometry which was used hereafter was not totally balanced, because of a constructive need relative to the stamp-

ing process. The cylinder was mounted as the upper roll of the rolling mill; Figure 7.11a and 7.11b show the pockets on the work-cylinder.

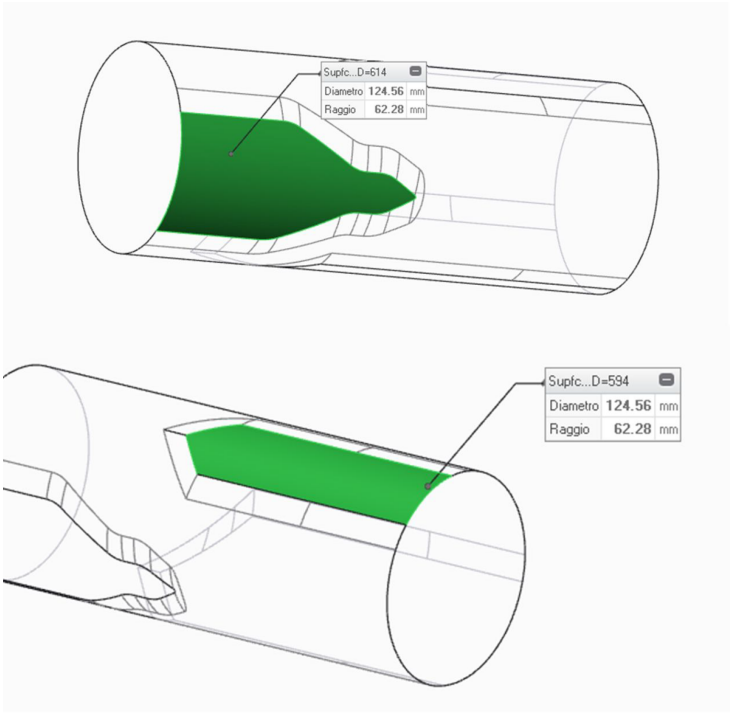

Figure 7.10 – 3D CAD of the work-roll

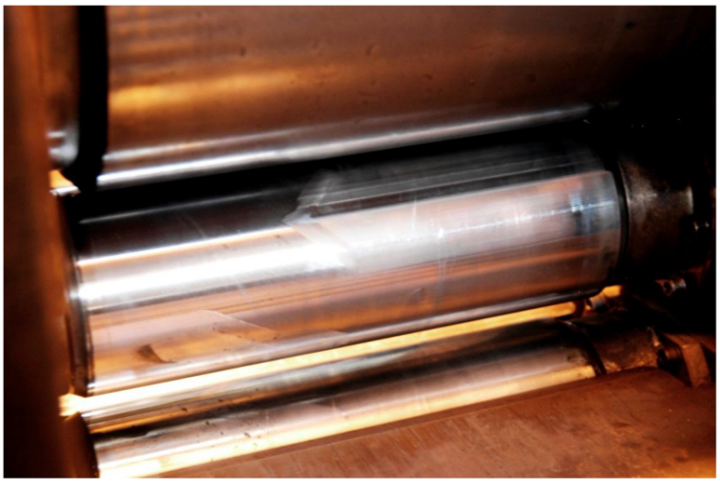

(a) Particulars of the wrought work-roll

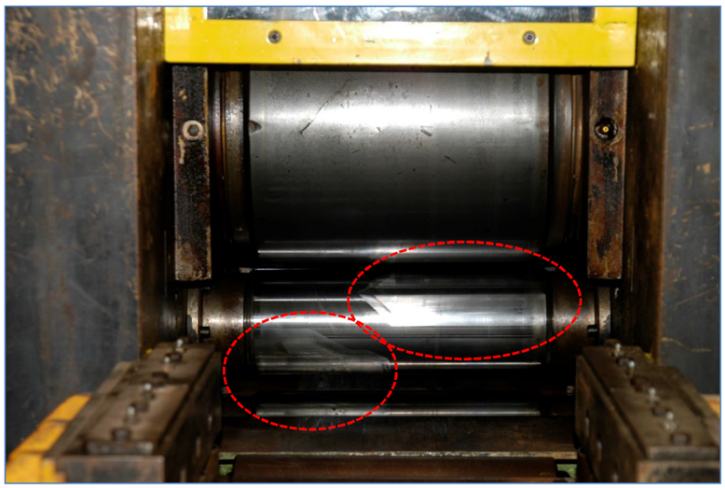

(b) Particulars of the wrought work-roll

Figure 7.11

Experimental tests immediately revealed criticalities such as waving, twist and even tears of the metal strip.

Figure 7.12 – Preliminary test result

All the highlighted defects can be attributed to the not 100% balanced geometry and to the absence of the pay-off and tension reels. Figure 7.12 shows a cold rolling test on a high-performance plastic material, considerable waving occurs despite its high deformation capacity.

Several tests were led on different materials with different initial thickness.

7.1.1 Test n.1

The first test was set-up with a reduction ratio of 30%, starting from a $0.7mm$ AA5754 sheet-metal plate. The length of the work-piece was intentionally less than half a rotation of the cylinder.

(a) 1st test result with thickness measure

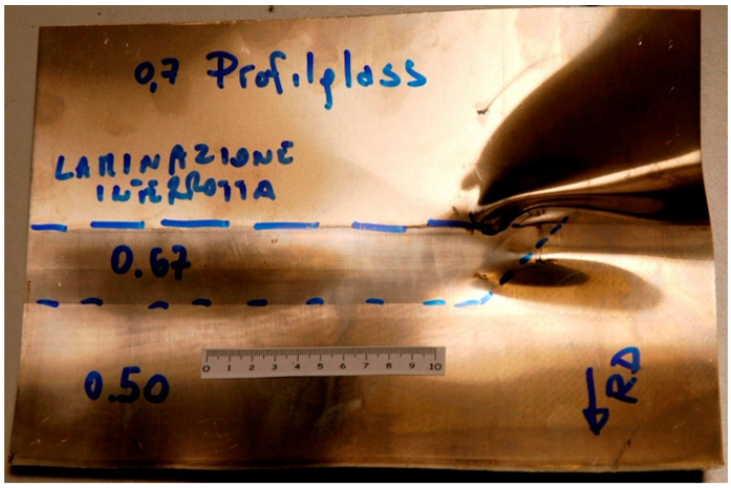

(b) 1st test result with thickness measure

Figure 7.13

Figure 7.13a and 7.13b show the thickness measures of the laminated product.

7.1.2 Test n.2

The second test was performed with the same set-up of the first one but with a full rotation of the cylinder.

Figure 7.14 – 2nd test result with thickness measure

The obtained work-piece is highly affected by wavings and tears and with a

differential elongation as well. Red arrows in Figure 7.14 point at the different elongations of the sheet metal plate.

7.1.3 Test n.3

The third test was led on a 6000 aluminium alloy with $1.2mm$ of initial thickness and a reduction ratio of 20%. It seems like the increase of thickness can attenuate the local deformation phenomena (waving etc.) even though the differential elongation remains unchanged (Figure 7.15).

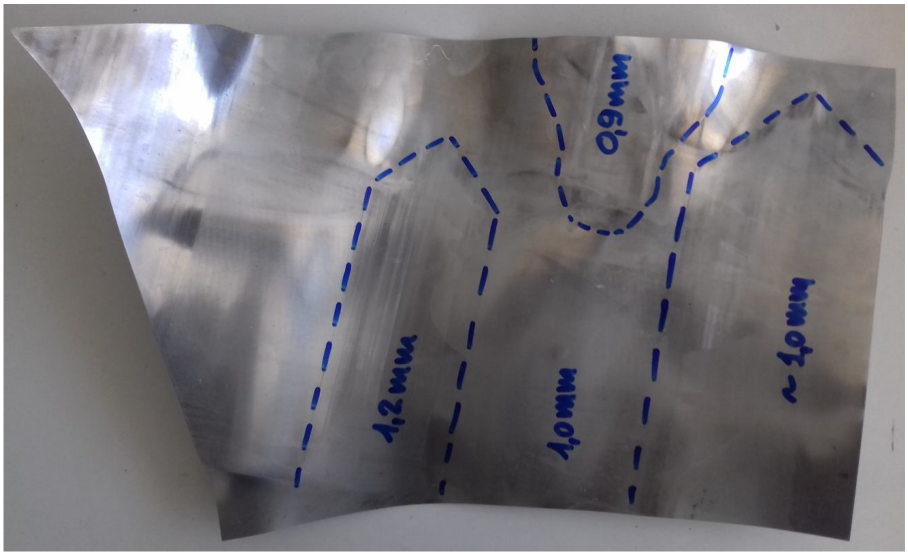

Figure 7.15 – 3rd test result with thickness measure

7.1.4 Test n.4

The fourth test was performed on the same 6000 aluminium alloy with $1.2mm$ of initial thickness, increasing the reduction ratio to 30%.

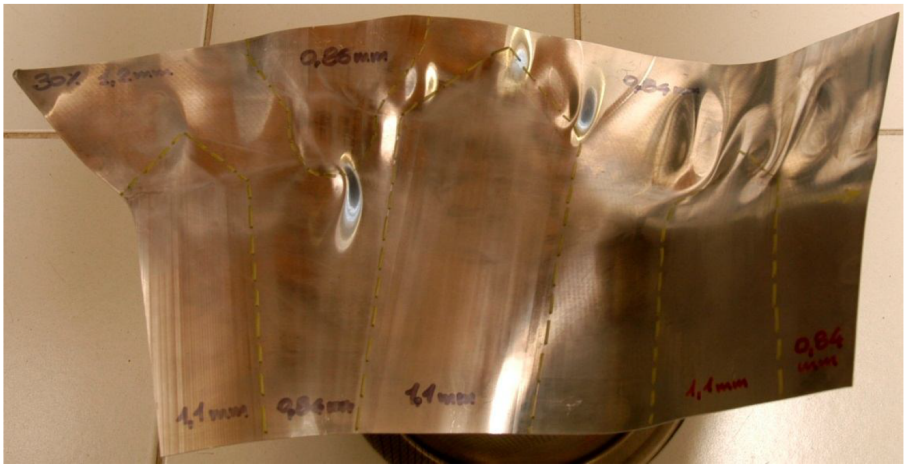

Figure 7.16 – 4th test result with thickness measure

Figure 7.16 shows the results of the test. The laminated specimen appears to be more defective than the previous one with regards to the local waving phenomena.

7.1.5 Test n.5

The last test was led on sheet metal of the same material as the previous ones but with a higher initial thickness ($3.0mm$) with a 6% reduction ratio.

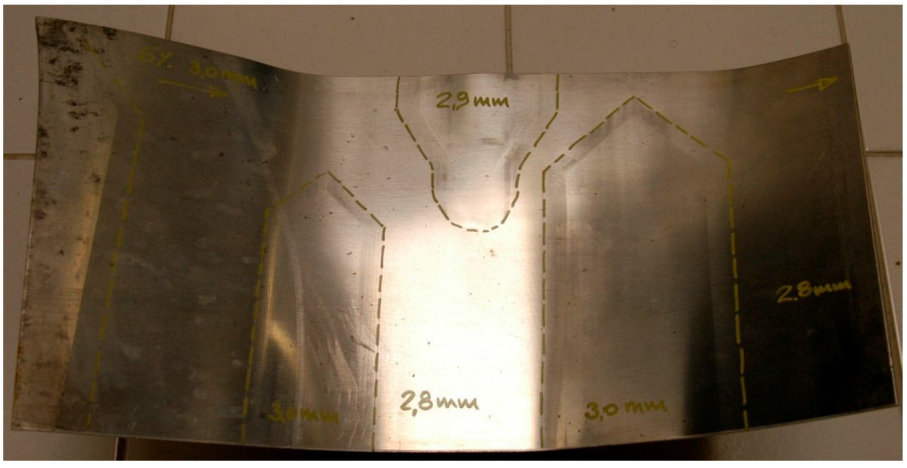

Figure 7.17 – 5th test result with thickness measure

In this case, the damage is very restrained even though both the differential elongation and a calender effect are still visible. The last defect can probably be attributed to the difference between the diameter of the upper and lower cylinder.

7.2 Full scale experimental test

In order to produce a complete prototype of the lateral sliding door frame, with a view to the stamping process as well, a full scale cold rolling mill was specifically designed.

The selected material for the test was a 5754 aluminium alloy with an initial thickness of $2.2mm$ and strip length of $1580mm$.

The machine was set up with a nominal thickness variation of $2.1mm$ on the over-thickness areas and $1.4mm$ elsewhere. Due to the continuous thickness variation between the two values of $1.4mm$ and $2.1mm$, the default thickness control was set off.

The rolling forces were calculated by the load cells in a range of $170 \div 300tons$, the pay-off and tension reels were equal to $2.2kg/mm^2$ and $2.4kg/mm^2$ respectively. Rolling speed was about $15m/min$.

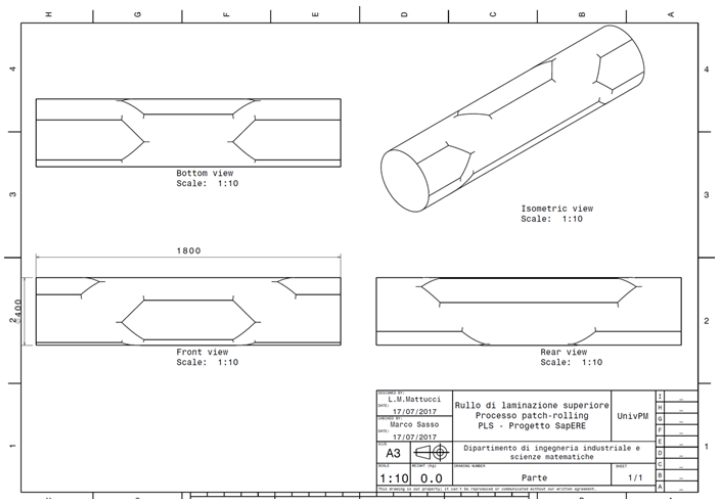

Figure 7.18 – Technical drawing of the full scale work-roll

Figure 7.18 shows the technical drawing of the wrought work cylinder by the envelope of the sketch of Figure 7.19 on the primitive cylinder of $400mm$.

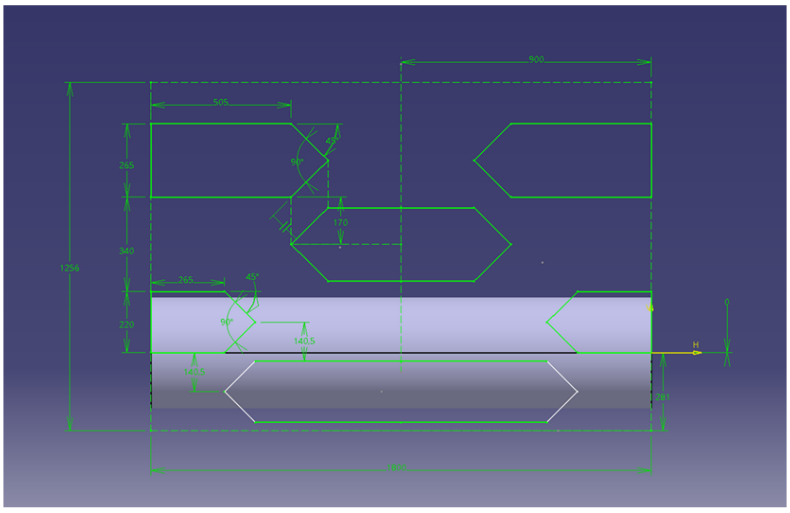

Figure 7.19 – Patch sketch to be enveloped on the base cylinder

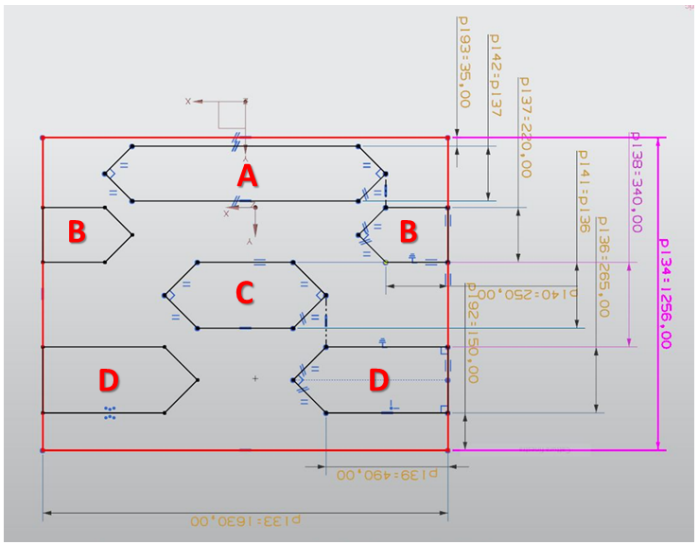

Figure 7.20 – Dimensional drawing of all the patches

The dimensioned sketch of Figure 7.20 reports two different pairs of patches, $A - B$ and $C - D$, which are perfectly balanced at the end of every rotation. The two pairs of patches $A - B$ and $C - D$ are clearly visible in Figure 7.21 and 7.22.

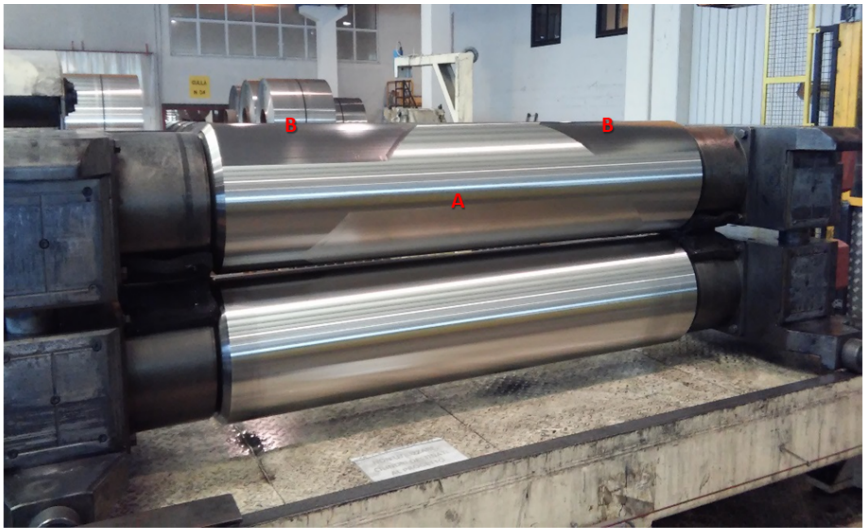

Figure 7.21 – Particulars of the A-B patch pair

Figure 7.22 – Particulars of the C-D patch pair

Figure 7.23a and 7.23b show the obtained work-roll.

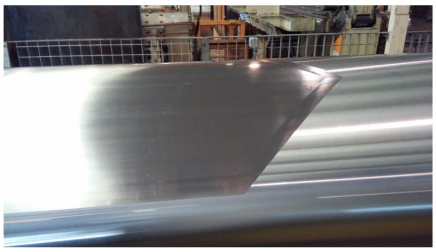

(a) Details of the wrought work-roll

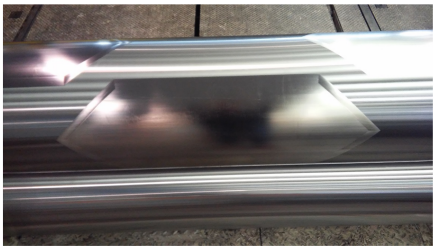

(b) Details of the wrought work-roll

Figure 7.23

Several defects arose from the start. Local buckling phenomena occurred downstream of each patch with a constant repeatability as shown in Figure 7.24. So the process was aborted and attempts were made right away to identify the possible causes for this.

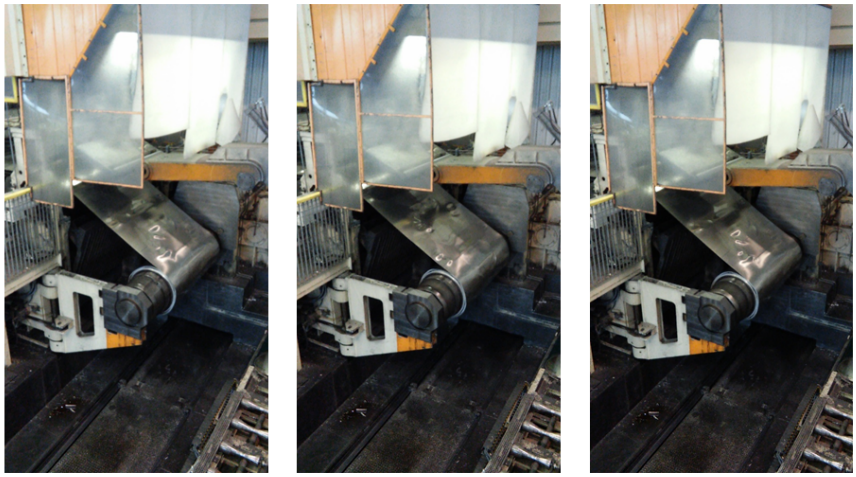

Figure 7.24 – Three moments of the full scale test

The initial means was to measure the thickness locally on a work-piece cut out from the defective strip.

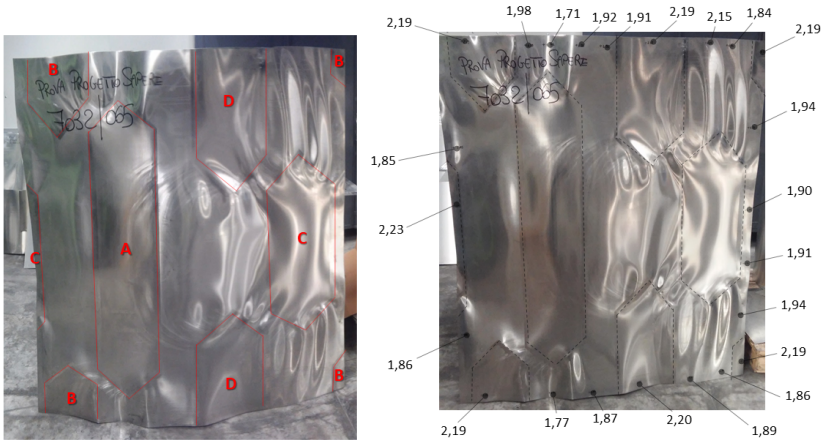

(a) Identification of the A-B and C-D patch pairs on the finished product

(b) Thickness measures on the finished product

Figure 7.25

Measures revealed that the process was totally out of control. The final thickness was very irregular and random, with no-identified zones where the final

thickness was correct. No 2.1mm nor 1.4mm thickness areas were discovered. This phenomenon might be related to the absence of the thickness control.

Other important considerations were made about the nature of the occurred wavings: the 4Hi typology of the cold rolling mill has been regarded as a possible cause. Maintaining a uniform gap between the rolls is difficult because the rolls deflect under the load required to deform the work-piece. The deflection causes the work-piece to be thinner on the edges and thicker in the middle. This can be overcome by using a crowned roller (parabolic crown). This solution works fine when the reduction ratio is set as constant.

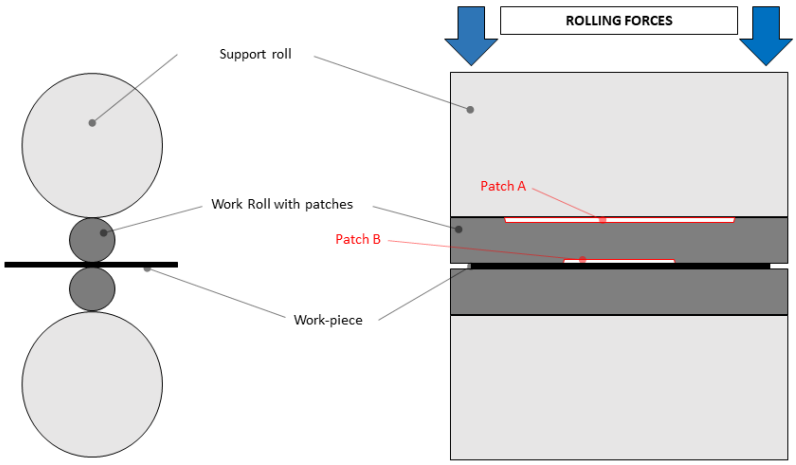

Figure 7.26 – Patch A in contact with the support-roll

However, due to the different local size of the work-roll (200mm nominal radius ÷ 199.3mm patch radius) the bending deformation is different when the pocket comes into contact with the support roller (Figure 7.26) which therefore works differently. This way, the work-piece elongation will be randomly different, being thinner in some places and thicker in others, generating the occurrence of the highlighted defect.

Chapter 8

Conclusions

The present research activity widely investigated the cold patch-rolling process. Several cases of study were developed and they consented to examine in depth the theoretical knowledge of the manufacturing process of laminated products.

At the end of these simulations, it was possible to identify some guide-lines useful in distributing the over-thickness areas over the whole work-piece.

- the position of the over-thickness areas influences the total deformation of the sheet metal plate in a very significant way; this is because of the direct relationship between the thickness reduction and the work-piece elongation (n.b. the rolling process can be reduced to a plain strain case);
- transition areas must be highly extended ($50 - 100$ times the ΔH where ΔH is the over-thickness size) in order to avoid local buckling phenomena or even worse the break of the strip;
- in order to reduce the bending of the strip, which occurs after the forces relative to the pay-off and tension reels are removed, it is very important that the total variation of the thickness must be the same value along the whole transversal dimension.

Regarding the latter, several analytical models were developed to numerically demonstrate the concept of the balance mentioned above. All the acquired know-how was thus applied to a hypothetical real application case with positive

analytical outcomes.

In order to generalize the feasibility of the process for every patch distribution the customer might require, it was necessary to identify a relationship between the main parameters involved in the process, not resorting to specific simulations for each geometrical solution. To this purpose a study of how and how much these parameters influence the process was led, through a Finite Element Method experimentation, organized according to the Design of Experiments techniques.

So a generic F.E.M. model with two patches and more than two rotations of the cylinders was developed and the principal variables were identified on it. The results of the DoE demonstrated a strong relationship between:

- Size and magnitude of the thinning area, which usually follows every patch, with:
  - the ratio between initial thickness to the size of the over-thickness;
  - length of the patch;
- Shear deformation magnitude with:
  - initial thickness;
  - length of the patch;
  - length of the transition area.

Looking at the results, it emerged that process variables such as initial thickness (t_0) and length of the patch (b) are the ones which most influence the length and the depth of the thinning area downstream of every patch.

In the same way, process variables like initial thickness (t_0), length of the patch (b) and most of all the length of the transition area (r), significantly influence the magnitude of the shear deformation related to the different reduction ratios between adjacent material bands.

The engineer must then identify a good combination of the process parameters to minimize the relevance of the thinning area, which might reveal itself to be very dangerous for the following stamping process. Furthermore, the engineer must reduce the magnitude of the shear deformations which could lead to local defects, such as buckling phenomena with an unacceptable surface quality

of the finished product, or even worse the sudden tear of the aluminium strip.

Present research also confirmed the importance of the formability properties of the selected material, and allowed a complete characterisation of several aluminium alloys and hybrid aluminium composites to be performed. Mechanical and formability properties were fully evaluated such as the maximum elongation and anisotropic parameters, and an interesting in-depth analysis was carried out regarding the heterogeneous behaviour of the 5754 aluminium alloy, which appears to be highly affected by the Portevin-LeChatelier effect.

Lastly, the process was validated by first developing a small scale rolling mill and then a full scale one, achieving a prototype and significant experimental tests.

Small scale testing led to severe damage on the rolled work-piece:

- buckling phenomena and tear of the work-piece – probably attributed to the not-completely balanced geometry of the patches and the absence of pay-off and tension reels;
- strip bending (calendering effect) – probably caused by the difference between the diameter of the upper and lower cylinders.

After a total balanced geometry was modelled, a full scale rolling mill was implemented. Some defects occurred in this case too. The metal-strip showed local buckling phenomena and after this, the thickness was measured and revealed to be completely out of control, being so far from the desired final thickness across the whole product.

The first problem may be related to the presence of the pocket. Normally, the support roll is appositely crowned in order to maintain a uniform gap between the upper and lower rolls despite the deflection due to the rolling forces. When the pocket comes in contact with the support roll, the effect of the crown is negated and the elongation of the strip is no longer constant, leading to buckling phenomena. The second problem might be attributed to the absence of the thickness control, which was necessarily set off because of the inconsistent thickness value of the laminated product.

A Design of Experiments with different shape of the patches is under devel-

opment and full scale tests with higher initial thickness are already scheduled for the near future.

Analysis of the new DoE together with the results of the new tests will be the basis of all future steps of this research which has not yet been concluded.

Bibliography

[1] V. B. Ginzburg, *Steel-Rolling Technology, theory and practice*. Taylor & Francis Inc, 1989.

[2] W. L. Roberts, *Cold rolling of steel, Manifacturing engineering and material processing/2*. M.Dekker, 1978.

[3] H. E. Boyer and T. L. Gall, *Metals Handbook*. American Society for Metals, 1985.

[4] A. I. H. Committee, *ASM Metals Handbook, properties and selection: nonferrous alloys and special-purpose materials*. American Society for Metals, 1990.

[5] D. Banabic, H. Binge, K. Pöhlandt, and A. Tekkaya, *Formability of Metallic Materials*. Springer, 2000.

[6] A. E2218-2, *Standard Test Method for determining Forming Limit Curves*. ASTM International, 2002.

[7] A. Makinouchi, "Sheet metal forming simulation in industry," *Journal of Material Processing Technology*, vol. 1, no. 60, pp. 19–26, 1996.

[8] G. Goodwin, "Application of strain analysis to sheet metal forming problem in the press shop," *Society of Automotive Engineers*, vol. 1, no. 680093, pp. 380–387, 1968.

[9] P. Ricci, M. El Mehtedi, L. Barone, and S. Spigarelli, "Effects of temperature and sheet thickness on formability of az31 magnesium alloy," *Materials Science Forum*, vol. 1, no. 604–605, pp. 147–152, 2009.

[10] R. Knockaert, Y. Chastel, and E. Massoni, "Experimental and numerical determination of texture evolution during deep drawing tests," *Journal of Material Processing Technology*, vol. 1, no. 110, pp. 300–311, 2001.

[11] M. Sasso, G. Palmieri, and G. Chiappini, "Sistema ottico di rilievo delle deformazioni per prove di tensione equibiassiale su elastomeri," *XXXVI Conv. Aias*, vol. 1, no. 1, p. nn, 2007.

[12] J. King, C. You, and J. Knott, "Serrated yielding and the localized shear failure mode in aluminium alloys," *Acta Metallurgica*, vol. 29, no. 9, pp. 1553–1566, 1981.

[13] J. Kang, D. Wilkinson, M. Jain, J. Embury, A. Beaudoin, S. Kim, R. Mishira, and A. Sachdev, "On the sequence of inhomogeneous deformation processes occurring during tensile deformation of strip cast {AA5754}," *Acta Materialia*, vol. 54, no. 1, pp. 209 – 218, 2006.

[14] M. Rossi, G. Chiapini, L. Mattucci, and D. Amodio, "Study of the local and global deformation process of an aluminium alloy using full-field measurments," *20th International ESAFORM Conference on Material Forming*, vol. 1, no. 1, p. nn, 2017.

[15] M. Sasso, A. Forcellese, M. Simoncini, D. Amodio, and E. Mancini, "High strain rate behaviour of aa7075 aluminum alloy at different initial temper states," *Key Engineering Materials*, vol. 651-653, pp. 114–119, 2015.

[16] A. Cottrell, "Lxxxvi. a note on the portevin-le chatelier effect," *The London, Edinburgh, and Dublin Philosophical Magazine and Journal of Science*, vol. 44, no. 355, pp. 829–832, 1953.

[17] A. van den Beukel, "Theory of the effect of dynamic strain aging on mechanical properties," *physica status solidi (a)*, vol. 30, no. 1, pp. 197–206, 1975.

[18] E. Pink and A. Grinberg, "Stress drops in serrated flow curves of a15mg," *Acta Metallurgica*, vol. 30, no. 12, pp. 2153 – 2160, 1982.

[19] S. Kumar, "Inverse behaviour of the onset strain of serrated flow," *Scripta metallurgica et materialia*, vol. 33, no. 1, pp. 81–86, 1995.

[20] Y. Brechet and Y. Estrin, "On the influence of precipitation on the portevin-le chatelier effect," *Acta metallurgica et materialia*, vol. 43, no. 3, pp. 955–963, 1995.

[21] P. Hähner, "On the critical conditions of the portevin-le châtelier effect," *Acta Materialia*, vol. 45, no. 9, pp. 3695–3707, 1997.

[22] J. Baird, "Dynamic strain aging," in *The Inhomogeneity of Plastic Deformation, ASM Seminar. 1973, 191-222*, 1973.

[23] H. Schreier, J.-J. Orteu, and M. A. Sutton, *Image correlation for shape, motion and deformation measurements*. Springer US, 2009.

[24] F. Pierron and M. Grédiac, *The virtual fields method*. Springer Science & Business Media, 2012.

[25] G. Le Louëdec, F. Pierron, M. A. Sutton, and A. P. Reynolds, "Identification of the local elasto-plastic behavior of fsw welds using the virtual fields method," *Experimental Mechanics*, vol. 53, no. 5, pp. 849–859, 2013.

[26] D. Amodio, G. Broggiato, F. Campana, and G. Newaz, "Digital speckle correlation for strain measurement by image analysis," *Experimental Mechanics*, vol. 43, no. 4, pp. 396–402, 2003.

[27] S. Avril, F. Pierron, M. A. Sutton, and J. Yan, "Identification of elasto-visco-plastic parameters and characterization of lüders behavior using digital image correlation and the virtual fields method," *Mechanics of Materials*, vol. 40, no. 9, pp. 729–742, 2008.

[28] M. Rossi and F. Pierron, "Identification of plastic constitutive parameters at large deformations from three dimensional displacement fields," *Comput. Mech.*, vol. 49, no. 1, pp. 53–71, 2012.

[29] L. Mattucci, *Studio numerico di un processo di laminazione a freddo a spessore variabile*. UnivPM, 2014.

[30] L. Vizzarri, *Studio e sviluppo di modelli numerici per processi di laminazione a spessore variabile*. UnivPM, 2015.

[31] F. Fischer, F. Rammerstrorfer, N. Friedl, and W. Wieser, "Buckling phenomena related to rolling and levelling of sheet metal," *International Journal of Mechanical Sciences*, vol. 1, no. 42, p. nn, 2000.

[32] R. Nakhoul, P. Montmitonnet, and S. Abdelkhalek, "Flatness defect in thin strip cold rolling and the friction impact on it," *40th NAMRC - North American Manufacturing Research Conference*, vol. 1, pp. 40–55, 2012.

[33] N. Mathieu, R. Dimistriou, A. Parrico, M. Potier-Ferry, and H. Zahrouni, "Flatness defects after bridle rolls: a numerical analysis of leveling," *International journal of material forming*, vol. 1, no. 1, pp. 255–266, 2013.

[34] S. Abdelkhalek, H. Zahrouni, P. Monmitonnet, N. Legrand, and M. Potier-Ferry, "Manifested flatness predictions in thin strip cold rolling using a general rolling fem model," *10° colloque national en calcul des structures*, vol. 1, no. 1, p. 1, 2011.

[35] D. C. Montgomery, *Progettazione ed analisi degli esperimenti*. McGraw-Hill, 2005.

[36] F. Campana, *"Dispense del corso" di Principi e Metodologie della Progettazione Meccanica*. Dipartimento di Costruzione di Macchine, Università di Roma "La Sapienza", 2006.